

Internal radionuclide dosimetry of model and patient based voxelised phantoms using the GATE toolkit

Kevin James Hickson (BAppSc)

A thesis submitted in (partial) fulfilment of the requirements for the degree of

Master of Applied Science (Medical and Health Physics)

School of Applied Sciences
College of Science, Engineering and Health
RMIT University
Melbourne Australia

August 2011

Declaration

Except where due acknowledgement has been made, the work is that of the candidate alone. The work has not been submitted previously, in whole or in part, to qualify for any other academic award. The content of the thesis is the result of work which has been carried out since the official commencement date of the approved research program, Any editorial work, paid or unpaid, carried out by a third party is acknowledged. Ethics procedures and guidelines have been followed.

Kevin Hickson

12 August 2011

Acknowledgments

I would like to thank the tremendous assistance of an number of people in the completion of this thesis. Particularly the supervision of Dr. Graeme O'Keefe, Centre for PET Austin Health. I was extremely lucky to have a supervisor that not only has exceptional research experience but who is also an experienced clinical Medical Physicist.

I would also like to thank my RMIT supervisors (in chronological order) Prof. Peter Johnston who started me off on this project. Dr. Alex Merchant who although left RMIT was still an excellent help in proof reading my thesis. Finally Dr. Rick Franich who has been fighting for the increased academic training of Medical and Health physicists at RMIT.

The support of Dr. Jianfeng He, Mr. Tim Saunder, Mr. Gareth Jones, Dr. Sylvia J Gong and all of the staff at the Centre for PET Austin Health is much appreciated.

I would like to acknowledge the assistance of Mr. Brett Pemberton from the Victorian Partnership of Advanced Computing and the GATE users-list for assistance in cluster computing of the GATE Monte Carlo package.

Thank you to Mr. Paul U, Mr. Anthony Wallace and Dr. Joseph Young for starting me on this path of Medical and Health physics.

I would like to thank my family Mum (who proudly proof read over the whole thesis), Dad, Liam, Chris and Callum. Finally to my beautiful wife Kristina who has been very understanding, supportive and lastly to our baby Annabelle, who was undoubtedly the biggest motivation in completing my Masters.

Contents

Declaration	i
Acknowledgments	ii
Table of Contents	iii
List of Figures	vii
List of Tables	x
Abstract	1
1 Introduction	3
1.1 Problem Statement	3
1.2 Aim and Scope	5
1.3 Research Approach	7
2 Background	8
2.1 Kerma and Absorbed Dose	8
2.2 Equivalent and Effective Dose	9
2.3 MIRD	11
2.4 Decay Data	15
2.5 Anthropomorphic Phantoms	16
2.6 Scaling Organ Masses	22
2.7 Uncertainties in Dosimetry Calculations	24
2.8 Standardised Uptake Value (SUV)	26
2.9 MIRDOSE and OLINDA\EXM	27
2.9.1 Dose factor and S-values	28
2.10 The Monte Carlo Method	29

2.11	Monte Carlo Codes	30
2.12	GATE	32
2.13	Applications of GATE	34
2.14	Chapter Summary	37
3	Method	38
3.1	Simulations in GATE	39
3.2	The MIRDS Benchmark of GATE	40
3.3	MIRDS Spheres in GATE Version 3.1.2	41
3.4	MIRDS Spheres in GATE Version 6.0	42
3.5	Voxelised Phantom Validation	43
3.6	Voxelised Source to Target	45
3.6.1	Homogeneous voxelised simulation	45
3.6.2	Heterogeneous voxelised simulation	46
3.7	Realistic Dosimetry Situations	48
3.8	XCAT Phantom Preparation	48
3.9	Preparation of Patient Data	50
3.9.1	Manual organ segmentation	53
3.9.2	Voxel attenuation map	55
3.9.3	Voxel source distribution	55
3.10	Calculating the DFs	56
3.11	Chapter Summary	57
4	GATE: MIRDS Spheres	58
4.1	Introduction	58
4.2	Validation Results	58
4.2.1	GATE version 3.1.2	59
4.2.2	GATE version 6.0 comparison of physics packages	59
4.3	Accuracy of the MIRDS Spheres	59
4.3.1	Negating electron transport	66
4.4	Comparison of GATE to the Gold Standard	69
4.5	Chapter Summary	72

5	Voxelised phantom validation	74
5.1	Introduction	74
5.2	Absorbed Fractions	75
5.2.1	Speed benchmark	75
5.2.2	Choice of physics packages	77
5.3	Source to Target	80
5.3.1	Homogeneous voxelised simulation	80
5.3.2	Heterogeneous voxelised simulation	81
5.4	Using Voxelised Phantoms	84
5.4.1	Absorbed fraction compared to the DF	85
5.5	Chapter Summary	86
6	Kidney to Liver Dose Factor	87
6.1	Introduction	87
6.2	XCAT Phantom	87
6.2.1	Distribution of energy	88
6.3	Patient	88
6.4	Result Analysis	92
6.4.1	Fitting data to different voxel sizes.	92
6.4.2	Scaling patient DF for voxel volume	97
6.4.3	Organ masses	98
6.5	Agreement to MIRD and OLINDA\EXM	99
6.6	Variations in Human Anatomy	102
6.7	Chapter Summary	103
7	Conclusions and Future work	104
7.1	Validating GATE	104
7.2	Patient and Model Based Absorbed Dose Calculations	105
7.3	Future work	106
7.3.1	Automation	106
7.3.2	Calculation of additional organs	107
7.3.3	Dynamic patient activity distribution	107
7.4	Final concluding remarks	108

A	Gate Macros	109
A.1	PBS Script Example	109
A.2	MIRD Spheres	110
A.2.1	GATEv3.1.2 MIRD	110
A.2.2	Calculate absorbed fractions	111
A.2.3	GATEv6.0 physics	112
A.2.4	Gate version 6 MIRD simulation	114
A.3	Voxel Phantoms	117
A.3.1	Interfile creation	117
A.3.2	Processing voxel dose	120
B	Absorbed Fractions	124
B.1	Simulated Values	124
B.2	Normalised Values	128
C	Monte Carlo	132
C.1	Introduction	132
C.2	Application Assumptions	133
C.3	Description	135
C.3.1	Random numbers	135
C.3.2	Tissue cross sections	137
C.3.3	Path length	137
C.3.4	Interaction type	139
C.3.5	Sampling the Klein-Nishina distribution	139
C.4	Code	142
C.4.1	User classes	142
C.4.2	Command line parser	151
	Bibliography	155

List of Figures

2.1	The difference between kerma and absorbed dose.	9
2.2	Illustration of cumulated activity, residence time, uptake and effective decay.	14
2.3	Extract from the Brookhaven National Laboratory web site.	16
2.4	Physical decay scheme for Fluorine-18.	16
2.5	Geometric phantom of an adult female.	17
2.6	Comparison of the specific absorbed fractions for different phantoms.	19
2.7	Male XCAT phantom.	21
2.8	Time activity curves.	25
2.9	Structure of GATE. Where the core layer defines basic mechanisms available in GATE, the application layer extends base classes for specific modeling and the user layer initiates the simulation by using scripts.	32
3.1	Center slice of voxelised sphere phantom for various voxel sizes.	44
3.2	Center slice of voxelised source to target phantom for various voxel sizes	46
3.3	OpenGL illustration produced from GATE of the source and target spheres in a homogeneous medium. It shows the geometric source region (red sphere) with gamma-ray photons (green line) and the geometric target region (blue sphere).	47
3.4	OpenGL illustration produced from GATE of the source and target spheres in a heterogeneous medium. The red sphere is the source region and it is set to be a kidney analog. The blue sphere is the target region, where the material is set to be a liver analog. The magenta slab is an analog of lung tissue where the yellow slab is an adipose (Fat) analog.	48
3.5	GATE code to implement a Fluorine-18 source.	49
3.6	Centre slice of the 95.05 kg XCAT phantom with varying voxel sizes. In units of density $\text{g}\cdot\text{cm}^{-3}$	51
3.7	Activity and Materials range tables used in GATE for the XCAT phantoms	52

3.8	Regions of interest of the patient phantom using Wasabi	54
4.1	Absorbed fractions in the MIRD spheres using GATE version 3.	60
4.2	Comparison of the absorbed fractions simulated by the different GATE packages for 0.03 MeV photons as a function of sphere mass.	61
4.3	Comparison of the absorbed fractions simulated by the different GATE packages for 0.1 MeV photons as a function of sphere mass.	61
4.4	Comparison of the absorbed fractions simulated by the different GATE packages for 2.75 MeV photons as a function of sphere mass.	62
4.5	Comparison of Absorbed Fractions as a function of mass between the MIRD pamphlets and a simple python based Monte Carlo code.	64
4.6	Comparison of Absorbed Fractions as a function of energy between the MIRD pamphlets and a simple python based Monte Carlo code.	65
4.7	Comparison of Absorbed Fractions between the MIRD pamphlet 8, a simple python based Monte Carlo code and GATE	67
4.8	Radiation yield for electrons in the MIRD - soft tissue composition.	68
4.9	Normalised absorbed fractions for 0.040 MeV photons against the gold standard.	70
4.10	Normalised absorbed fractions for 0.140 MeV photons against the gold standard.	70
4.11	Normalised absorbed fractions for 0.662 MeV photons against the gold standard.	71
5.1	Normalised absorbed fractions for 140 keV photons in voxelised sphere phantoms with different masses, using the <i>standard</i> physics package.	76
5.2	Normalised absorbed fractions for 140 keV photons in voxelised sphere phantoms with different masses, using the <i>low energy</i> physics package.	76
5.3	Normalised absorbed fractions for 140 keV photons in voxelised sphere phantoms with different masses, using the <i>PENELOPE</i> physics package.	77
5.4	Dosimetry plots for a homogeneous phantom with a voxel size of 0.25 mm.	82
5.5	Dosimetry plots for a heterogeneous phantom with a voxel size of 0.25 mm.	83
6.1	Energy distribution of uniform activity in both kidneys of the XCAT phantom (Slice 110, Large).	91
6.2	Dose distribution of non-uniform activity in both kidneys, overlaid with the patients low dose CT.	93
6.3	Dose distribution in the liver resulting from non-uniform activity in both kidneys, overlaid with the patients low dose CT.	94

6.4	Fitting DF to voxelised phantoms of different voxel size.	96
C.1	Histogram of scattered radiation in a semi infinite tissue medium using the python Monte Carlo code.	134
C.2	Diagram for a python based Monte Carlo code for gamma photons. The function used and what it returns is located below the description steps.	136
C.3	A Logic diagram for direction and energy change from Compton scattering	141

List of Tables

2.1	Radiation weighting factors recommended by ICRP publication 103	10
2.2	Tissue weighting factors recommended by ICRP publication 103	11
2.3	Characteristics of different voxelised phantoms.	20
3.1	GATE and GATE related software versions	39
3.2	Tissue composition used in the MIRD pamphlets	41
3.3	Element compositions of the material used in the heterogeneous phantom.	47
3.4	Voxel and array dimensions of the XCAT phantom	50
4.1	Speed benchmarking of a geometric phantom for GATE version 6 physics packages	63
4.2	Hypothesis Testing of the GATE physics libraries	72
5.1	Absorbed fractions in the MIRD spheres for 140 keV photons using voxelised phantoms.	78
5.2	Speed benchmarking of a voxelised phantom for GATE version 6 physics packages	79
5.3	Hypothesis Testing of the GATE physics libraries	79
5.4	Absorbed Fractions for a simple source to target region.	80
5.5	DFs for a simple source to target region.	81
5.6	Absorbed Fractions for a simple source to target region.	84
5.7	DFs for a simple source to target region.	84
6.1	DFs of the XCAT phantom for the kidney to kidney.	89
6.2	DFs of the XCAT phantom for the kidneys to liver.	90
6.3	Dosimetry results of a Average patient.	92
6.4	Fitting parameters for XCAT kidney to kidney.	95
6.5	Fitting parameters for XCAT kidney to liver.	97
6.6	Organ mass corrections for voxel volume.	99

6.7	Summary of calculated DFs.	100
6.8	Summary of calculated DFs.	102
B.1	Values for the absorbed fractions simulated in GATE.	124
B.2	Normalised values for the absorbed fractions simulated in GATE. Columns 3 to 6 are normalised to recommended values from Stabin. Column 7 are results from Stabin	128
C.1	Tissue composition used in the MIRDP pamphlets	137
C.2	Cross-section for the tissue composition used in the MIRDP pamphlets	138
C.3	Total cross-sections for the tissue composition used in the MIRDP pamphlets	138

Abstract

The desire for realistic patient specific dosimetry estimates of internally distributed radioactivity are realised by using Monte Carlo simulations of voxelised phantoms. The purpose of this thesis was to validate the GATE Monte Carlo package as a dosimetry tool and to investigate the accurate application of model and patient specific voxelised phantoms.

Validation of the GATE Monte Carlo package was performed by simulating the absorbed fractions of simple geometric spheres of uniform radioactivity compared to accepted values from Stabin and Konijnenberg [1]. Voxelised spheres have also been simulated and it was found that the GATE *Low Energy* physics package was the most suitable for simulations of voxelised phantoms.

The simulation of the scalable XCAT voxelised phantom has been performed to evaluate the effect of voxel size and patient organ mass on the calculation of dose factors. It was found that for organ self irradiation significantly small voxels are required to ensure that insufficient voxel sampling does not effect the absorbed dose calculation. A retrospective absorbed dose calculation of true patient images was then performed with a correction for insufficient voxel sampling. In this work the scalable XCAT phantom has also been used to show that a voxel size of 2 mm or less is suitable for accurate calculations of organ cross dose.

By comparing the scaled XCAT phantoms with patient and traditional phantoms it was concluded that considerable care is required when adapting model-based

phantom results to individual patients. As differences in patient anatomy contribute significant variability to the dosimetry calculation, it is therefore recommended that where available individual patient specific dosimetry should be calculated using direct Monte Carlo simulation in favor of organ mass scaling.

Chapter 1

Introduction

The use of radionuclides in medicine is well established in both the diagnostic and therapeutic fields. In these fields radiopharmaceuticals are exploited for their bio-distribution. Exposure to ionising radiation is associated with some risks and as such needs to be reliably estimated for its acceptable use in both clinical and research applications. All exposure to ionising radiation must be justified such that the benefits to either the patient or grater community far outweigh any associated risks.

1.1 Problem Statement

Molecular Imaging has been shown to be useful in assessing the effectiveness of new pharmaceuticals and provides added benefits in accelerating development from pre-clinical discovery to Phase III clinical trials through *in vivo* imaging [2]. Approval by regulatory authorities to undertake clinical trials in humans, require a number of ethical and safety issues to be assessed. If Molecular Imaging is used in addition to standard clinical care then one such safety issue is an internal radiation dosimetry assessment. Even though the exposure is justified and will provide a net benefit to the community, imaging studies additional to standard clinical care are not guaranteed to deliver any benefits to the patient participating in the trial. It is therefore important

that radiation dosimetry assessments are as accurate as possible.

Molecular Imaging is a unique modality that images tracers that chemically react within a biological system and therefore respond to molecular changes. This is a notable difference compared to X-ray Computed Tomography (CT) which measures differences in linear attenuation. Molecular Imaging may increase the probability for early diagnosis of disease as changes in function may occur before observable anatomical changes. Research activities into novel radiopharmaceuticals is therefore well developed, as a large spectrum of tracers to target specific disease or metabolic function is possible.

Radiation dosimetry assessments for clinically used radiopharmaceuticals can be obtained by reviewing publications that report the radiation dose in units of “*dose per injected activity*”. Examples of such publications include [3, 4, 5], where radiation dosimetry is defined as the calculation, assessment or estimation of the energy absorbed by ionization of atoms in tissue from the emission of energetic radiation. Radiation dosimetry is based on the key quantity of absorbed dose. Absorbed dose is defined as the mean energy of ionizing radiation absorbed per unit mass of an absorbing medium. Absorbed dose is usually indicative of ¹ the probability of harmful biological effects [6].

The development of novel radiopharmaceuticals are governed by the same regulatory and ethical approval required by any new drug. In the case of a new radiopharmaceutical a simple review of previous published literature is by no means adequate. A radiation dosimetry assessment of a new radiopharmaceutical must therefore be calculated using a model based approach. At the Phase I stage in the clinical development of a new radiopharmaceutical, dosimetry assessment may involve analytical and modeling based techniques or data obtained from preclinical animal scans. Results of a dosimetry estimate will therefore only be as good as the

¹Absorbed dose alone (see section 2.1) is insufficient to predict the effects of radiation. Radiation and tissue weighting factors (see section 2.2) are also required to evaluate the effective dose.

standardised models of human anatomy and physiology. Further dose assessment can then be undertaken on results from the Phase I trial.

Novel radiopharmaceuticals may have both diagnostic and therapeutic applications. Accurate dosimetry of diagnostic procedures is important for making judgments on the diagnostic benefits to the patient compared to the associated radiation risks. In diagnostic applications relatively small amounts of radioactivity are used in comparison to therapeutic procedures. However the number of procedures over the entire population is much higher. Dosimetry of diagnostic radiopharmaceuticals is therefore primarily concerned with the dosimetry of a total population or group. The absorbed dose from internally distributed radioactivity used in diagnostic procedures is usually only calculated using models based on reference individuals and not specific patients.

The model based approach may be appropriate for diagnostic radiopharmaceuticals however a more patient specific approach is required for radionuclide therapy where the aim is to deliver a therapeutic dose of radiation to malignant tissue. Accurate calculations of the absorbed dose in malignant tissues and surrounding organs from radionuclide therapy will directly affect the outcomes of the treatment.

1.2 Aim and Scope

In recent times considerable development has been made in model and patient specific dosimetry estimations. A key area of work has been the application of detailed computer models of patient anatomy. In the past simple geometric shapes like spheres, cubes, cylinders, etc. have been used to describe patient anatomy [7]. This approach as a first approximation for calculating radiation doses, is useful to combat limitations in computational methods at the time of the models development. These models do however lack realism.

Improvements to model based dosimetry assessment are achieved by using voxelized phantoms. A voxelized phantom is made up of a group of small volume

elements (a voxel) that together are used to define a complex geometry. Standard voxelized human phantoms include those described by Zubal [8] and Segars [9]. Definitions of activity distribution may also be described using a voxelized approach. The desire for patient specific dosimetry estimates has also become more practical with hybrid imaging technologies like PET/CT or SPECT/CT. In this case the CT image is used as the voxelized phantom and the PET or SPECT image as the voxelized source.

For simple geometric shapes it may be possible to solve for the absorbed dose analytically, however as the geometry becomes more complex the ability to analytically solve for the absorbed dose becomes less likely. The Monte Carlo method can be used to simulate the interaction of radiation through matter and is usefully applied to this problem. One publicly available software framework for this calculation is Geant4 [10] and its Application to Tomography Emission (GATE) [11]. GATE has the ability to realistically model the physics processes involved in Molecular Imaging and dosimetry applications.

It was proposed that a validation of the GATE toolkit for internal dosimetry applications be undertaken, with particular attention to the calculation of absorbed dose fractions. The following validation steps have be investigated;

- use GATE to calculate absorbed doses in simple geometric models that can be compared with analytical determined values.
- comparison of GATE results to previous literature, simple calculated values or other available Monte Carlo codes and
- investigate the possible sources of error involved with using voxelised models in GATE.

Following validation the use and appropriateness of the Extended Cardiac Torso (XCAT) [12] phantom in GATE was investigated. Estimations of the absorbed dose

to large organs have therefore been provide as a model based dosimetry estimate. A concluding goal of this work was to use GATE in a retrospective dosimetry assessment of an individual patient who has undergone a Molecular Imaging examination. This retrospective assessment illustrates the differences in model vs patient specific absorbed dose calculations and demonstrates the possibility of patient specific dosimetry estimates as opposed to nominal standard phantom calculations.

1.3 Research Approach

To achieve the aims above, chapter 2 introduces background information about dosimetry methods, concluding with a short review of studies already completed. Chapter 3 provides methods for simulating simple dosimetry problems in GATE, as well as setting out a method for benchmarking and validating GATE results. Chapter 3 concludes with describing the processes required for performing realistic dosimetry calculations in GATE. Chapter 4 outlines the results of validating GATE against the well known values for simple geometric spheres containing uniformly distributed activity. Chapter 5 shows results of validating voxelised phantoms in GATE for simple source and target regions. Chapter 6 provides results for a dosimetry assessment of the XCAT voxelised phantom and concludes by investigating a retrospective dosimetry assessment of a patient who received a fluorodeoxyglucose (^{18}F -FDG) PET/CT examination. Finally chapter 7 discusses further work that may be undertaken and concludes on the previous chapters.

Chapter 2

Background

2.1 Kerma and Absorbed Dose

Energy transfer from ionizing radiation may involve both direct ionization and indirect forms of kinetic energy transfer. The International Commission on Radiation Units and Measurements (ICRU) introduced the term Kinetic Energy Released in a medium (kerma) to describe the kinetic energy ($\Delta\bar{E}_{tr}$) transferred from photons to electrons in a mass (Δm) [13]. Kerma is defined as;

$$\text{kerma (J} \cdot \text{kg}^{-1}\text{)}; \quad K = \frac{\Delta\bar{E}_{tr}}{\Delta m} \quad (2.1)$$

The closely linked term absorbed dose was introduced in section 1.1 and is the mean energy ($\Delta\bar{E}_{ab}$) of ionizing radiation absorbed per unit mass (Δm) of an absorbing medium. Absorbed dose is defined as;

$$\text{Absorbed dose (J} \cdot \text{kg}^{-1}\text{)}; \quad D = \frac{\Delta\bar{E}_{ab}}{\Delta m} \quad (2.2)$$

It should be noted that for practical measurement purposes the increment of mass, Δm , should be small enough so that the absorbed dose is defined to a point, but not

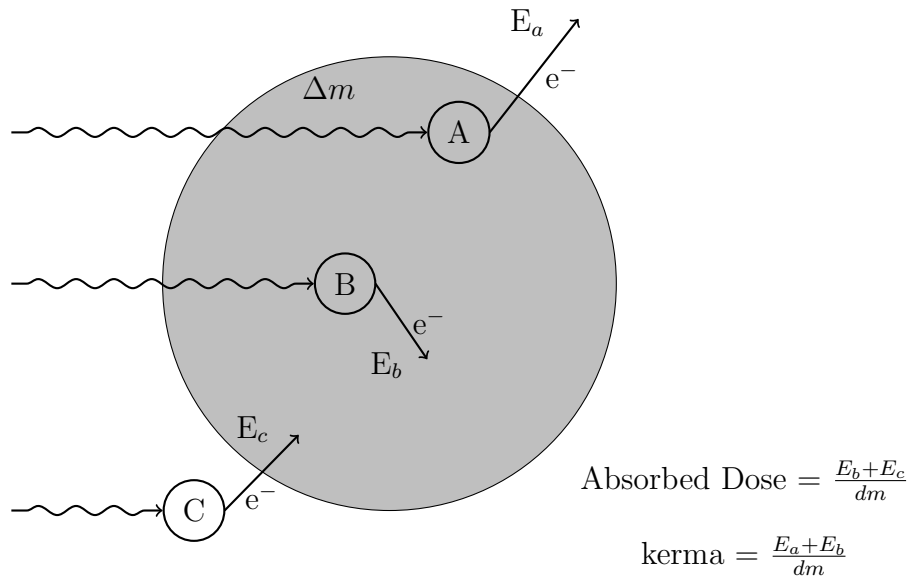


Figure 2.1: The difference between kerma and absorbed dose. (Adapted from [15])

so small that statistical fluctuations in the energy deposited are significant. Equations 2.1 and 2.2 have the SI units of $\text{J} \cdot \text{kg}^{-1}$. The SI units for kerma and absorbed dose is given the name gray (Gy) after Louis Harold Gray for his contributions to radiation dosimetry and notably the Bragg-Gray Principle [14].

The difference in the two terms kerma and absorbed dose are illustrated in figure 2.1. Photons impart kinetic energy to electrons both in (point A and B) and out (point C) of the region of interest. The kinetic energies of the electrons are also absorbed both in the region (energies E_b and E_c) and out (energy E_a) of the region. Therefore the kerma is dependent on where the photon imparted its kinetic energy, and the absorbed dose is dependent on where the energy (in this case the secondary electron) was absorbed.

2.2 Equivalent and Effective Dose

From the point of view of radiation biology, the absorbed dose alone is insufficient to predict the effects of radiation. Biological damage due to radiation is reliant on not only the average energy deposited but also the spatial variations of energy deposition

at the microscopic level [15].

For example an experiment may make measurements at different biological end points or vary the kinds of radiation used. These experimental differences may result in a different absorbed dose required to produce the same effect. For radiation types with a high linear energy transfer (LET) (e.g. alpha particles or heavy ions) this is particularly apparent.

To address this the International Commission on Radiological Protection (ICRP) introduced the terms equivalent dose H_T and radiation weighting factor w_R . Using the notation given in the ICRP report 103 [16] the equivalent dose is;

$$\text{Equivalent dose (J} \cdot \text{kg}^{-1}\text{)}; \quad H_T = \sum_R w_R D_{T,R} \quad (2.3)$$

Where; $D_{T,R}$ is the absorbed dose in a tissue T from a radiation of type R. The radiation weighting factor for different radiation types are shown in table 2.1 [16]. The sum is applied over all types of radiation involved. The SI unit for equivalent dose is given the name sievert (Sv) after Rolf Sievert to avoid problems resulting from the use of two quantities with the same dimensions [17].

Table 2.1: Radiation weighting factors recommended by ICRP publication 103

Radiation type	Radiation weighting factor, w_R
Photons	1
Electrons ^a and muons	1
Protons and charged pions	2
Alpha particles, heavy ions	20
Neutrons ^b	1-20

^a excludes Auger electrons.

^b a continuous function of neutron energy.

Previously the term quality factor, Q was used instead of the radiation weighting factor. Q is only a function of LET for different radiation types [18], where the w_R is based on the relative biological effectiveness (RBE) and the increasing probability of

radiation damage with increasing dose (stochastic effects). In the field of radiobiology the RBE is defined as the ratio of the absorbed doses of two types of radiation producing the same biological effect in identical systems.

The introduction of equivalent dose leads onto the definition of effective dose and is defined by the weighted sum of tissue equivalent doses. That is;

$$\text{Effective dose; } E = \sum_T w_T H_T = \sum_T w_T \sum_R w_R D_{T,R} \quad (2.4)$$

Here w_T is the tissue weighting factor. The sum is performed over all organs and tissues in the human body. Values for the tissue weighting factor are shown in table 2.2. These values are derived from the contributions of individual organs and tissues to the overall radiation harm from stochastic effects.

Table 2.2: Tissue weighting factors recommended by ICRP publication 103 [16]

Tissue	w_T
Bone–marrow (red), Colon, Lung, Stomach, Breast, Remainder tissues ^a	0.12
Gonads	0.08
Bladder, Oesophagus, Liver, Thyroid	0.04
Bone surface, Brain, Salivary glands, Skin	0.01

^a Remainder tissues: Adrenals, Extrathoracic (ET) region, Gall bladder, Heart, Kidneys, Lymphatic nodes, Muscle Oral mucosa, Pancreas, Prostate (σ), Small intestine, Spleen, Thymus, Uterus/cervix (φ)

Further details on the fundamental units used in radiation dosimetry can be found in [16, 19, 20].

2.3 MIRD

Calculation of absorbed dose to an organ from an internally distributed radionuclide has been described by The Medical Internal Radiation Dose (MIRD) Committee of the American Society for Nuclear Medicine (SNM). The publication of a number of pamphlets by the committee have been accepted by the Nuclear Medicine community

as the standard approach for dosimetry calculation of diagnostic radiopharmaceuticals.

In its most simplest form the MIRD method for absorbed dose calculations requires; the total number of nuclear transitions that have occurred over a given time and the amount of energy deposited per nuclear transition per unit mass of the target organ. Ultimately however appropriate information or in most cases assumptions on the following is required;

- the administered radiopharmaceutical activity,
- the rate of radionuclide decay (physical half life),
- the fraction of energy/type per decay (spectrum information),
- the fraction of administered activity that is located in each source organ (time activity function and uptake),
- the length of time the activity is in the source organ (effective half life),
- the total number of decays in the source organ (cumulated activity),
- the fraction of energy absorbed in the target organ from the source organ (absorbed fractions), and
- the mass of each organ.

The absorbed dose from a source organ r_h to a target organ r_k in the MIRD method is;

$$D_{r_k} = \sum_h \tilde{A}_h S(r_k \leftarrow r_h) \quad (2.5)$$

The absorbed dose in the target organ is summed over all source organs. \tilde{A}_h is the cumulated activity in the source organ 'h' where $S(r_k \leftarrow r_h)$ is the mean absorbed dose per unit of cumulated activity (or S value). The cumulated activity is reliant on

both physical decay (λ_p) of the radiopharmaceutical and its biologic removal (figure 2.2). The effective decay constant (λ_{eff}) is given by the addition of the physical and biological decay constants. In the original MIRD system the residence time τ_h was used to define the average time that the administered activity spends in an organ. The cumulated activity can therefore be written as;

$$\tilde{A}_h = A_0 \cdot \tau_h = \int_0^\infty A_0 e^{-\lambda_h^{eff} \cdot t} dt \quad (2.6)$$

The function representing the uptake and clearance may be modelled by the sum of exponential functions, that include terms for the fractional uptake ($f_1 \dots f_n$) and its biologic removal ($\lambda_1 \dots \lambda_n$). Equation 2.7 therefore can also be used to describe cumulated activity.

$$\tilde{A}_h = A_0 \int_0^\infty \sum_{i=0}^n f_i e^{-(\lambda_i + \lambda_p)t} dt \quad (2.7)$$

The S value is a function of the mass of the target region m_{r_k} , the mean energy emitted per unit cumulated activity (Δ_i) for radiation of type i and the absorbed fraction ϕ_i . Where the absorbed fraction is the ratio of the energy absorbed in the target region (k) by the energy emitted from the source organ (h). The S value is therefore written as;

$$S(r_k \leftarrow r_h) = \sum_i \Delta_i \frac{\phi_i(r_k \leftarrow r_h)}{m_{r_k}} \quad (2.8)$$

where i is for the i-type radiation.

The absorbed fraction ϕ_i is a useful quantity that has been calculated for a number of different shapes and isotopes. The absorbed fraction is a term that is dependent on the penetration of the ionising source and attenuation characteristics of the medium as well as the medium geometry. The MIRD committee produced two relevant reports on this topic for different shapes with activity emitting different energy photons. These were MIRD pamphlets 3 and 8 [21, 22]. The pamphlets have

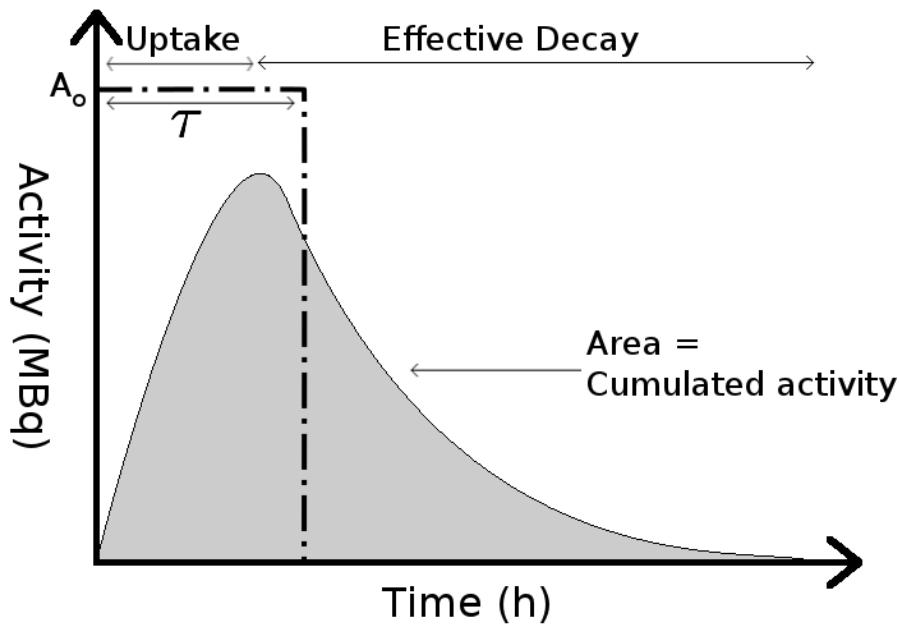


Figure 2.2: Illustration of cumulated activity, residence time, uptake and effective decay.

been recalculated by Stabin and Konijnenberg [1] and can be given the suitable title as the “gold standard” for absorbed fraction values in simple geometric regions.

Also of note is the fact that S-values are not limited to an organ scale. In fact nothing prohibits the use of the MIRD schema to smaller organ regions, small-scale tissue regions or even a cellular level. The MIRD committee has released documentation on S-values at a cellular level [23, 24] and also at a voxel based level [25].

In voxel based dosimetry, tomographic images are used for activity quantification and the absorbed dose may be calculated on a voxel-wise basis using direct Monte Carlo simulation (section 2.10). The MIRD schema defines the absorbed dose in a target voxel k from N surrounding source voxels h as equation 2.9.

$$D_{vox_k} = \sum_{h=0}^N \tilde{A}_{vox_h} \cdot S(vox_k \leftarrow vox_h) \quad (2.9)$$

Where \tilde{A}_{vox_h} is the cumulated activity in the source voxel h and S is defined as the mean absorbed dose to a target voxel per radioactive decay in the source voxel h . When $h = 0$ the self absorption in the target voxel k is considered. Voxel based dosimetry is useful in calculating isodose contours and dose volume histograms within tissue regions with non-uniform activity uptake and is therefore applicable to radionuclide therapy. Although computationally intensive, voxels may be grouped to define whole organs in which tissue weighting factors may be applied to calculate the effective dose.

2.4 Decay Data

Equation 2.8 has many forms. An extension to this equation is the definition of the mean energy emitted per unit of cumulated activity, Δ_i . An accepted expression for Δ_i is shown in equation 2.10.

$$\Delta_i = y_i \times E_i \quad (2.10)$$

Where, y is the number of radiations with energy E emitted per nuclear transition. E is the energy per radiation (MeV) and i is the radiation type. Decay data for radionuclides used for medical purposes are found in a variety of sources including the RADAR website [26] or other published sources [27]. Figure 2.3 shows an extract from the Brookhaven National Laboratory website [28] which report isotopes in the MIRD format. Figure 2.4 shows the traditional decay diagram for ^{18}F to ^{18}O decay via electron capture and positron emission[29]. Fluorine-18 is shown due to its relevance to PET imaging.

9-FLUORINE-18

Half-life = 109.77 Minutes Nov-1996
Decay Mode(s): $\epsilon + \beta^+$

<u>RADIATIONS</u>	<u>y(i)</u> <u>(Bq-s)⁻¹</u>	<u>E(i)</u> <u>(MeV)</u>	<u>y(i) × E(i)</u>
β^+ 1	9.67E-01	2.498E-01*	2.42E-01
$\gamma \pm$	1.93E+00	5.110E-01	9.89E-01
K X-ray	1.80E-04	5.249E-04*	9.42E-08
K X-ray	4.74E-12	5.000E-04*	2.37E-15
Auger-K	3.07E-02	5.200E-04*	1.60E-05
Listed X, γ and $\gamma \pm$ Radiations			9.89E-01
Listed β , ϵ and Auger Radiations			2.42E-01
Listed Radiations			1.23E+00

* Average Energy (MeV).

Oxygen-18 Daughter is stable.

Figure 2.3: Extract from the Brookhaven National Laboratory web site [28].

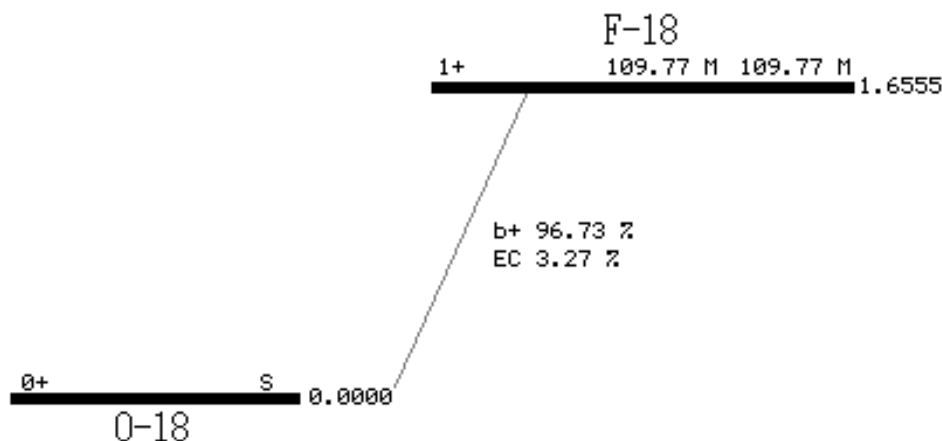


Figure 2.4: Physical decay scheme for Fluorine-18 reproduced from [29].

2.5 Anthropomorphic Phantoms

A number of anthropomorphic phantoms have been defined and used for dosimetry problems over time. The phantoms can be split into two different groups, Mathematical and Voxelised phantoms. Mathematical phantoms are defined by using geometric volumes and planes, to represent a variety of organs in a highly stylised way. Mathematical phantoms of note include the MIRD phantom [30] of the standard

man, ADAM (standard man) and EVA (standard woman) [31] and the Cristy and Eckerman pediatric phantoms [7]. Figure 2.5 shows the components of a Female adult mathematical phantom built from the geant4 class G4PhantomBuilder [32] which is the geant4 implementation of the Oak Ridge National Laboratory phantoms [7].

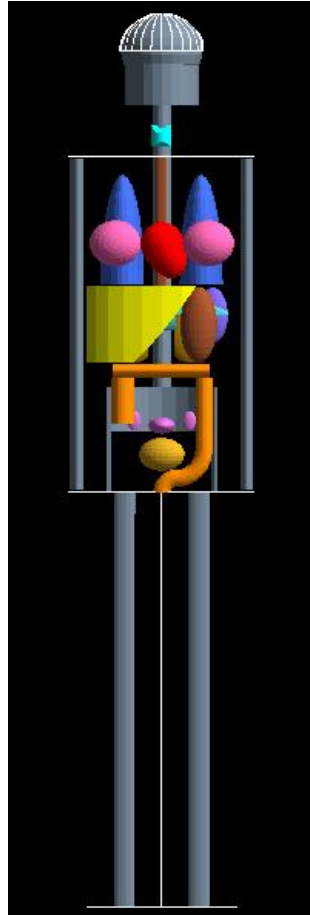


Figure 2.5: Geometric phantom of an adult female [32].

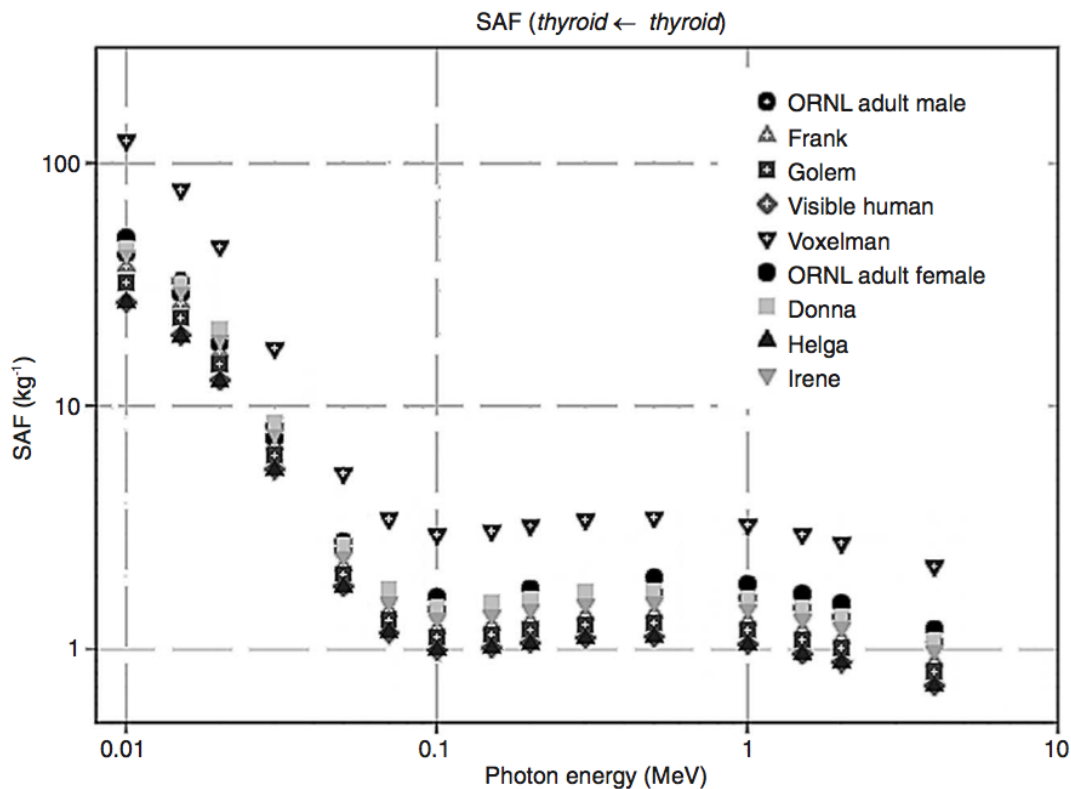
As an example of the mathematic phantom the following equation 2.11 represents the Liver of the MIRD phantom which is defined by an elliptical cylinder cut by a plane and defined between $27 \leq z \leq 43$. Another organ example are the Kidneys, which are defined by ellipsoids also cut by a plane.

$$\left(\frac{x}{16.5}\right)^2 + \left(\frac{y}{8}\right)^2 \leq 1, \quad \frac{x}{35} + \frac{y}{45} - \frac{z}{43} \leq -1 \quad (2.11)$$

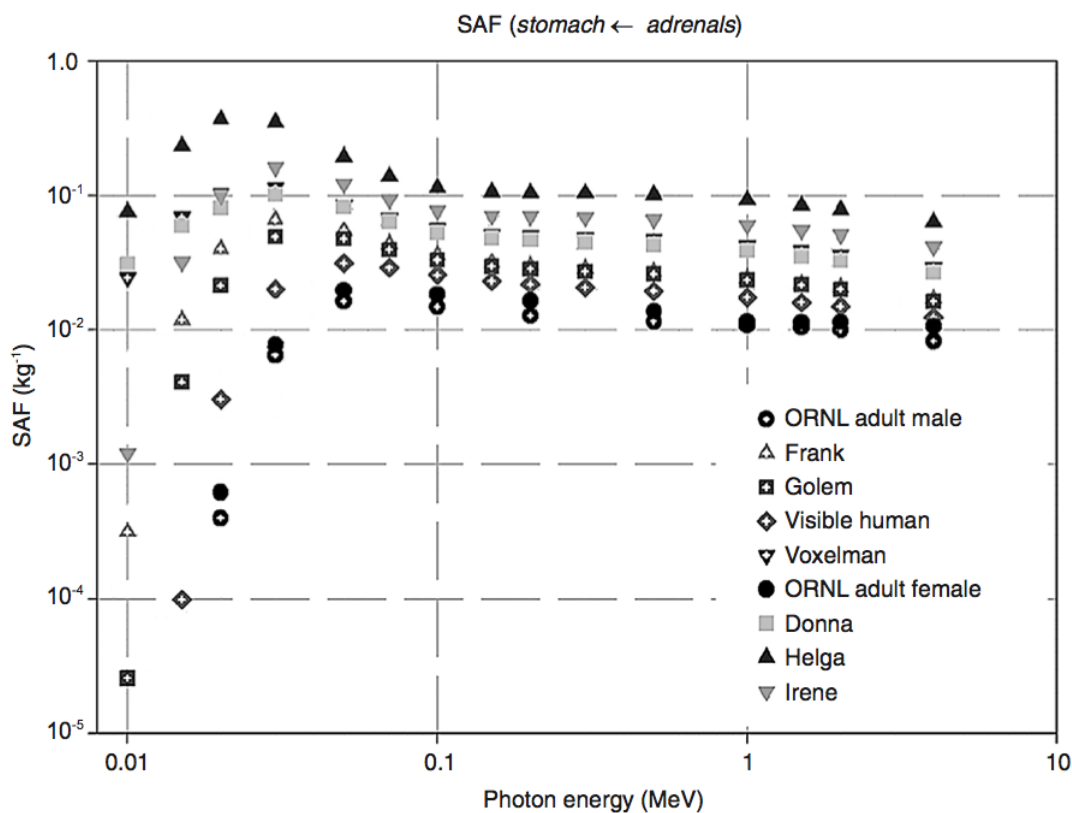
A number of tomographic voxelised phantoms of human anatomy have been published in peer review papers. Models are available of adult males [8, 33, 34], adult females [35, 36] (including pregnant subjects [37]), children [38, 39] and babies [40, 41]. Models have been reported for Caucasian and Asian [42, 43] subjects. Organ segmentation has been completed from CT and MRI images with varying voxel sizes. Colour photographs of the Visible Human Project [44, 45] have also been used for segmentation. It is considered that voxelised phantoms are more realistic representations of human anatomy compared to traditional mathematical based phantoms [9], however minor assumptions are made about the density composition of the phantom.

Zankl et al. [46] have used the Voxelman [8] and the GSF¹ family of voxel phantoms [36] to calculate specific absorbed fractions for Monoenergetic photon energies. Table 2.3 shows the image characteristics of the voxelised phantoms used by Zankl et al. and includes the subjects height, weight and body region. The differences in the specific absorbed fractions for each of the voxelised phantoms and the Cristy, Eckerman Oak Ridge National Laboratory (ORNL) adult mathematical phantoms are shown in figure 2.6. Since the simulation framework (Monte Carlo physics assumptions) is the same for all of these phantoms, differences in the specific absorbed fraction are a result of geometry. The notable differences for each phantom demonstrates that the use of reference phantoms for internal dose estimates may not necessarily be accurate to patient specific situations. In fact an insufficient representation of a real patient gives rise to large changes in the specific absorbed fraction. The magnitude of this change is dependent on the physical differences between the reference phantom compared to the patient.

¹German National Research Center for Environment and Health



(a) Specific Absorbed Fractions for organ self-absorption $\Phi(\text{thyroid} \leftarrow \text{thyroid})$



(b) Specific Absorbed Fractions for organ cross dose $\Phi(\text{stomach} \leftarrow \text{adrenal glands})$

Figure 2.6: Specific absorbed fractions for monoenergetic photons for seven adult voxelised phantoms compared to the Cristy, Eckerman adult mathematical phantoms reproduced from Zankl et al. [46].

Table 2.3: Characteristics of voxelised phantoms used by Zankl et al. [46].

Model	Height (cm)	Weight (kg)	Body region	Voxel width (mm)	Voxel depth (mm)	Voxel height (mm)	Array shape
Frank	-	-	Head and trunk	0.74	0.74	5	512x512x193
Golem	176	69	Whole body	2.08	2.08	8	256x256x220
Visible Human	180	103	Head to knee	0.91	0.94	5	512x512x250
Voxelman	178	70	Head to thigh	3.75	3.75	4	128x128x236
Donna	176	79	Whole body	1.875	1.875	10	256x256x179
Helga	170	81	Head to thigh	0.98	0.98	10	512x512x114
Irene	163	51	Whole body	1.875	1.875	5	256x256x348

Organ segmentation is a time consuming process which when performed manually may also suffer from operator subjective error [47]. Significant research is currently being undertaken for automated organ segmentation. Current methods are however limited to larger organs such as the Liver [48], Spleen [49], the Lungs [50] and the Kidneys [51]. Segmentation of contrast enhanced CT [52] and MRI [53] images have also been used.

These voxel based phantoms are of patient data sets and are therefore dependent on the resolution of the imaging equipment. The data sets have fixed voxel sizes and if different voxel sizes are required, then interpolation would have to be performed. Interpolation is both time consuming and may introduce errors since organ shapes are not analytically defined [54]. It should be noted that scaling of geometric phantoms is not difficult, however these simple representations lack realism. One of the more useful phantoms for this work are the NURBS Cardiac Torso (NCAT) [9] and Extended Cardiac Torso (XCAT) [12] series of phantoms. These are based on an extension to the 4-D Mathematical Cardiac Torso (MCAT) [55] phantom using non-uniform rational b-splines (NURBS) surfaces [56]. The use of parametric surfaces overcome limitations in scaling the NCAT/XCAT data sets for different voxel sizes.

The NCAT and XCAT phantoms have been designed to account for respiratory

and cardiac motion. Myocardial SPECT studies were the first application of the NCAT phantom, with the cardiac model being developed by tagged MRI datasets of a normal healthy patient [9]. CT data sets of the Visible Human Project were used to construct the remainder of the torso [57]. The XCAT phantom is an extension of the NCAT phantom that includes the head and neck region as well as organs in the lower abdomen.

Segars states that *'an ideal computer phantom would combine the realism of a patient-based pixelized phantom with the flexibility of a geometrical or mathematical phantom'* [9]. It is therefore considered that the XCAT phantom (figure 2.7) is currently a powerful realistic model of human anatomy that is ideal for model based internal radiation dosimetry calculations.

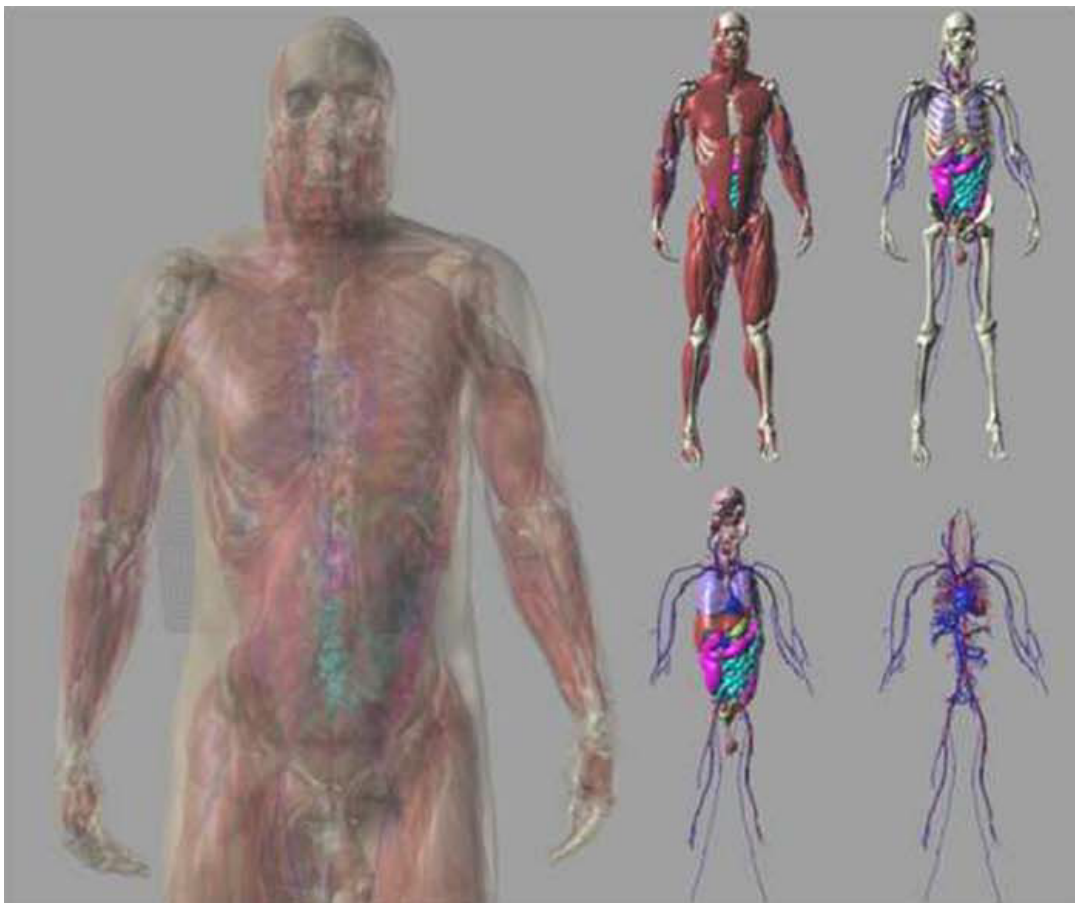


Figure 2.7: Male XCAT phantom. [12]

Variations in human anatomy have also been studied using the NCAT phantom

by Marine et al. [58] and the companion paper by Clark et al. [59]. Individual organ sizes can vary significantly between patients, Marine et al. review relevant literature of organ mass values for Adult Males and Adult Females with particular attention to the 10th, 25th, 50th, 75th and 90th percentiles. It was found that for organ self-dose the specific absorbed fraction varies from 15% to 30% and for organ cross-irradiation the specific absorbed fraction varies from 8% to 33%. Clark et al. measures differences in moderately and severely obese adults where the organs remained the same size as the 50th percentile but only surrounded by increasing volumes of visceral adipose tissue. Clark et al. finds that between these two groups depending on the irradiating organs little change in the specific absorbed fraction is observed compared to the 50th percentile.

2.6 Scaling Organ Masses

It is considered that the use of reference phantoms for internal dose estimates may not necessarily be accurate to patient specific situations. In an attempt to address this issue the MIRD pamphlet 11 [60] provided some guidance on how scaling of reference S-values for both the photon and electron components of the emission spectrum should be approached.

For photon absorption the absorbed fraction and specific absorbed fraction is scaled as in equation 2.12, assuming that the photon path length is large relative to the diameter of the organ.

$$\phi_{pt} = \phi_{ref} \left(\frac{m_{pt}}{m_{ref}} \right)^{1/3} \quad \Phi_{pt} = \Phi_{ref} \left(\frac{m_{ref}}{m_{pt}} \right)^{2/3} \quad (2.12)$$

Where ϕ_{pt} is the patient absorbed fraction and ϕ_{ref} is the reference phantom absorbed fraction. For target organs that are some distance from the source organ the photon absorbed fraction varies directly with the organ mass. Therefore scaling the target

organ mass for the photon specific absorbed fraction for organ cross-irradiation is not required [61]. This has been confirmed by Petoussi-Henss et al. [62].

For non-penetrating radiation, self absorption is the dominate process and therefore the absorbed fraction has traditionally been set to 1.0 for organs that are much larger then the mean-free-path of the radiation [63]. This leads to the specific absorbed fraction being inversely proportional to the mass of the source organ. If the source and the target are the same organ then the reference S-Value may also be scaled by the organ mass for the non-penetrating component of the emission spectrum [64]. The MIRD perspective [65] scales the patient S-values by equation 2.13. By assuming that the $1/m^{2/3}$ correction from equation 2.12 for the gamma component of the emission spectrum is negligible as a first order correction (as the majority of photons are not absorbed) then equation 2.13 holds [66].

$$S_{h \leftarrow h}(pt) = S_{h \leftarrow h}(ref) \times \frac{m_h(ref)}{m_h(pt)} \quad (2.13)$$

For the organ_k ← organ_h cross-irradiation case the target mass is not corrected, however the source organ mass is. If it is assumed that for non-penetrating radiation all of the energy is deposited in the source organ then only the gamma component of the emission spectrum will contribute to the absorbed fraction in the target organ (which follows equation 2.12). The computer program OLINDA\EXM [61] (see section 2.9) corrects for different source organ masses by equation 2.14.

$$S_{k \leftarrow h}(pt) = S_{k \leftarrow h}(ref) \times \left(\frac{m_h(ref)}{m_h(pt)} \right)^{\frac{2}{3}} \quad (2.14)$$

Scaling of reference phantoms and organs have typically been applied when patient organs are significantly smaller or larger then the reference organs. Organ mass scaling seems to be used more exclusively for radionuclide therapy situations where a more patient specific dose calculation is required. This is supported in the

literature [67, 68].

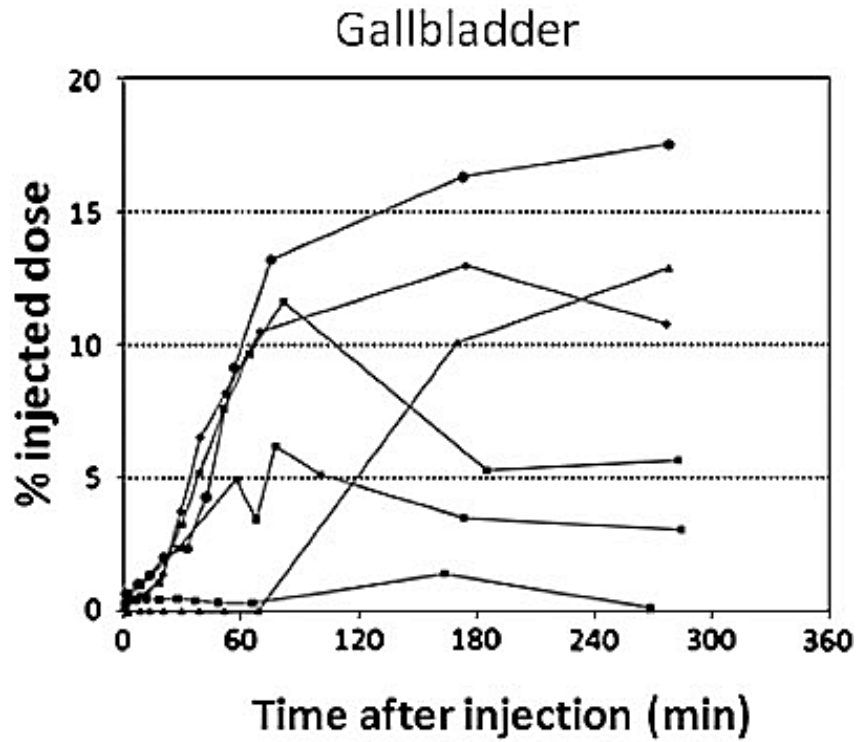
2.7 Uncertainties in Dosimetry Calculations

A systematic analysis of the uncertainties in radiopharmaceutical dosimetry calculations using a MIRD based approach has been documented previously by Stabin [69].

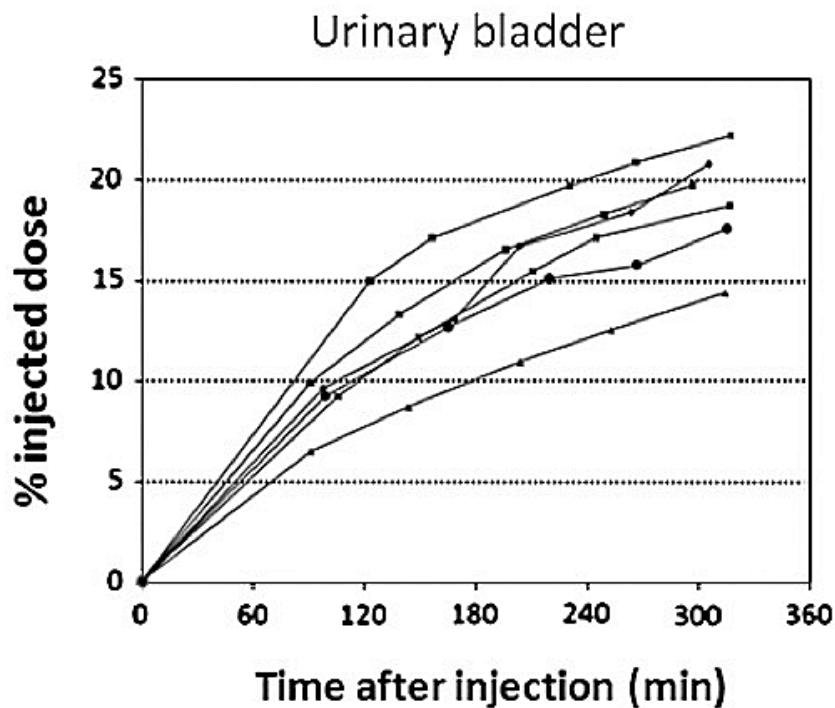
The absorbed dose equation 2.5 used in the MIRD system may be split into terms used to describe either biokinetic processes (\tilde{A}_h) or physical / model terms ($S(r_k \leftarrow r_h)$).

From equations 2.6 and 2.7 the physical decay constant and initial administered activity provide a relatively small uncertainty in diagnostic procedures compared to applying standardised fitting parameters for fractional uptake and biologic removal. The physical decay constants for medical radioisotopes are well known and have an uncertainty often less than 0.01% [70]. Wood and Collins [71] for example report the half-life of Tc-99m as 0.250281 ± 0.000022 days. The initial administered activity is limited to the accuracy of the initial activity measurement performed by a dose calibrator. For dose calibrators, current regulations state a required measurement error of less than 10%, however an error of less than 5% is more common [72].

Applying standardised fitting parameters for fractional uptake and biological removal to a population will introduce additional uncertainties. Differences in uptake curves between patients can be considerable. Figure 2.8 shows results from Koole et al. [73] and demonstrates this variation for six patients administered ^{18}F -GE067, which is a radioligand for in vivo brain amyloid imaging. The percentage injected dose is shown for both the gallbladder (figure 2.8a) and the Urinary bladder (figure 2.8b). The major source of these differences are explained by biokinetic differences between individual patients however other sources of error may be introduced such as incorrectly defining the region of interest.



(a)



(b)

Figure 2.8: Time activity curves for six patients administered ^{18}F -GE067, for both the gallbladder (a) and urinary bladder (b). (reproduced from Koole et al. [73])

The absolute uncertainty in the calculation of the S-values for standardised anthropomorphic phantoms may be limited to approximately 5% [69]. From equation 2.8, Δ_i provides the least uncertainty and is comparable to the low uncertainties of the decay constant. For example Helmer and Van der Leun [74] reports the γ_1 -ray energy for Tc-99m as 140.511 ± 0.001 keV. The uncertainty in the specific absorbed fractions can be minimised by performing a large number of radiation transport histories (sections 2.10, 2.11). It should however be noted that S-values for standardised anthropomorphic phantoms represent a median value for only a small reference group of patients. In clinical practice these standardised individuals are accurate for only small percentages of the population. Therefore the largest errors are introduced by applying reference S-values to individual patients that significantly differ in size, shape or weight from the standardised phantoms. Figure 2.6b shows that the specific absorbed fraction and therefore the S-value may vary greatly from one phantom geometry to another.

2.8 Standardised Uptake Value (SUV)

The Standardised Uptake Value is a dimensionless semi-quantitative unit used for uptake normalisation of PET scans and is often used as an aid for standardised visual image interpretation. SUV is defined as the ratio of activity concentration in a structure to the average concentration in the entire body [75]. Authors have normalised to both body weight [76] and body surface area [77]. Equation 2.15 defines SUV body weight.

$$SUV_{BW} = \frac{C(t) \cdot 2^{t/t_{\frac{1}{2}}}}{D/M_{body}} \quad (2.15)$$

where $C(t)$ is the voxel radioactivity concentration (kBq/mL) at time t after injection. $t_{\frac{1}{2}}$ is the isotope decay half-life, D is the injected dose (MBq), and M_{body}

(kg) is the mass of the subject.

From a practical point of view SUV is obtained by calibrating the PET scanner to convert counts per voxel into radioactivity concentration, it is therefore plausible to determine the activity at time t per gram by scaling the image voxels by $\frac{D}{M_{body}} \cdot 2^{-t/t_{\frac{1}{2}}}$. Some have been critical of the clinical application of SUV [78, 79], however it has been used successfully by a number of authors in defining organ time-activity curves of dosimetry calculations [73, 80].

2.9 MIRDOSE and OLINDA\EXM

The most widely accepted values for S-Values for nuclear medicine applicable radionuclide are from the original MIRD pamphlet 11 [60] and the Internal dosimetry software MIRDOSE [81] which has been superseded by OLINDA\EXM (Organ Level INternal Dose Assessment \EXponential Modeling)[61]. These two software programs are the most widely used method for calculating absorbed doses from radiopharmaceuticals. OLINDA\EXM has also been accepted by the US Food and Drug Administration after concerns were raised regarding the use of MIRDOSE as a “medical device” [82, 83].

Calculation methods for MIRDOSE and OLINDA\EXM are similar with only slight differences. MIRDOSE exclusively used the methods set out in the MIRD primer [84], where OLINDA\EXM uses information provided electronically by the RADAR (RAAdiation Dose Assessment Resource) group [26].

Absorbed fractions for penetrating radiation are calculated using Monte Carlo methods in both the MIRDOSE and OLINDA\EXM programs. Calculations for non-penetrating radiation for MIDOSE are based on the MIRD 11 methodology where for the self absorption case, the absorbed fraction equals 1. When the source and target organ are separated by any distance the absorbed fraction then equals 0. MIRD 11 also assumes that the absorbed fraction at the surface of an organ

containing non-penetrating radioactivity will be $\frac{1}{2}$. This approach may however not be accurate for small organs or when the energy of the so-called non-penetrating radiation is high. Therefore OLINDA\EXM applies a correction for loss of electron energy if the organ mass is less than 1 kg and has an energy greater than 0.1 MeV. The correction is an interpolation of the tables developed by Stabin and Konijnenberg [1].

Both the MIRDOSE and OLINDA\EXM programs provide use of the Cristy and Eckerman anthropomorphic phantoms [7]. The isotope database was also increased in OLINDA\EXM to over 800 radionuclides compared to 223 different radionuclides in MIRDOSE3.

2.9.1 Dose factor and S-values

OLINDA\EXM uses equation 2.16 to express absorbed dose, which is ultimately the same as equation 2.5. Where N ($Bq \cdot s$) is the number of disintegrations that occur in the source organ and DF ($\frac{Gy}{Bq \cdot s}$) is the dose factor.

$$D = N \times DF \quad (2.16)$$

It has been stated that the residence time has led to some confusion in the MIRDOSE program and that N be used to replace $A_0 \cdot \tau$ [61]. The dose factor is mathematically equivalent to the S-value and therefore may be referred to interchangeably with the S-value in some texts. Stabin and Siegel [85] have also suggested that equation 2.16 replace those used in the MIRD or ICRP [86] systems. Hence the DF will be referred to throughout this thesis and not the S-value.

2.10 The Monte Carlo Method

Monte Carlo (MC) methods are based on random variable sampling from a known distribution to numerically solve problems for which an analytical solution does not exist [87]. MC methods are made up of the following components;

- a probability distribution that describes the system being analysed,
- generation of a (pseudo) random number,
- a rule used to sample the probability distribution from the generated random number, typically based on the underlying dynamics or physics of the system under investigation.
- variance reduction techniques to reduce computational time, and
- a history (or scoring) of the interested quantities.

The tracking of individual photons and electrons is a suitably complex problem that can be divided into a number of independently smaller problems where each smaller problem may be solved using a MC approach. For example a particle may travel a random distance in a material before it undergoes some interaction where, the event may then describe a random energy change in the original particle. This example describes three random processes that will each follow an independently known (or approximated) distribution. A detailed example of a photon specific Monte Carlo code is discussed in Appendix C.

Sources of error when using a MC approach are dominated by statistical uncertainty due to sampling variations and the uses of an adequate mathematical models to represent the true physical processes involved. Statistical uncertainty can always be reduced by increasing the number of events tracked, however this will also increase computational costs. This limitation is still however less important than making appropriate assumptions about the physical model.

For example, a model representing the energy absorbed in a region of interest from incoming photons that undergo Compton or photoelectric interaction may assume that the energy is absorbed at the point of energy transfer (i.e. kerma = absorbed dose). By assuming that the photon energy is deposited locally (i.e. zero interaction length) the computational burden is reduced as no electron tracking is required. Therefore, for a given duration of computation, more photons can be tracked thus reducing statistical uncertainty. This assumption will work for the region of interest if it is large and the interaction point did not occur near the region boundary. Of course if the region is small (about the size of the mean electron range) then there is some probability that the electron will escape the region. In this case the zero interaction length assumption will cause an overestimate of energy deposited in the source organ and an underestimate in the electron energy absorbed in neighbouring organs.

2.11 Monte Carlo Codes

A number of highly validated general-purpose radiation transport codes are available in the public domain. Each code was originally developed for different applications however over time they have become more and more general. Public domain codes of note include; Monte Carlo N-Particle (MCNP) [88], Electron Gamma Shower (EGS) [89] and GEometry ANd Tracking (Geant) [10].

MCNP has a long and interesting history with various name changes and an origin in the 1940s. Its major application has traditionally been neutron transport where it has been described to have no competitor [90]. MCNP added electron transport and as such its applicability has increased. For example MCNP has been used by Yoriyaz et al. [91] for absorbed dose calculations for internal emitters used in radioimmunotherapy using the Zubal [8] phantom. Where Ferrari, Sohrabpour and Miro [92, 93, 94] have used MCNP for external dosimetry calculations. It should

also be noted that the current version MCNP5 is written in FORTRAN90 and C.

EGS was first developed at the Stanford Linear Accelerator Center for simulation of high-energy electromagnetic cascades. At the outset it was almost exclusively used in high-energy accelerator projects, however improvements in low energy photon and electron transport changed this [95]. Nowadays EGS [89] has become the dominant code for medical physics applications and some have referred to it as the de facto gold standard for clinical radiation dosimetry [96]. EGS uses MORTRAN which is a preprocessor for FORTRAN77 but also has C/C++ class libraries that are linked to the EGS code.

Geant was developed at CERN for high energy physics problems and was originally written in FORTRAN, until its current version Geant4 which is a total rewrite in C++. Particular attention was originally paid to improving geometry definitions for multi-detector simulations. Like MCNP and EGS, Geant has included *low energy* packages making it more useful for medical applications. These packages are referred to as *standard*, *low energy* and *PENELOPE*. The *standard* package tracks photons and electrons down to 1 keV, where the *low energy* package tracks photons and electrons down to 250 eV. The *low energy* package is based on the Livermore libraries [97]. *PENELOPE* [98] itself is a MC code that has been designed specifically for coupled electron-photon transport. The *PENELOPE* code will also track electrons and photons down to 250 eV. The physics packages of *PENELOPE* were re-engineered and validated in Geant4 by the creators of the *PENELOPE* code [97, 99]. This further increases the usefulness of Geant4 to dosimetry problems of internal emitting radiopharmaceuticals.

2.12 GATE

The use of Monte Carlo methods has become increasingly popular in medical imaging, especially since the developments of dedicated simulation toolkits for Emission Tomography, most notably Geant4 Application for Tomographic Emission (GATE) [100] and Simulation System for Emission Tomography (simSET) [101]. The preferred choice is quickly becoming GATE since it is built on the well-validated Geant4 code with a stable and flexible geometry manager.

GATE uses underlying C++ classes so that the input does not rely on any C++ programming by the GATE user. GATE has a layered structure that consists of a developer, core, application and user layers (figure 2.9).

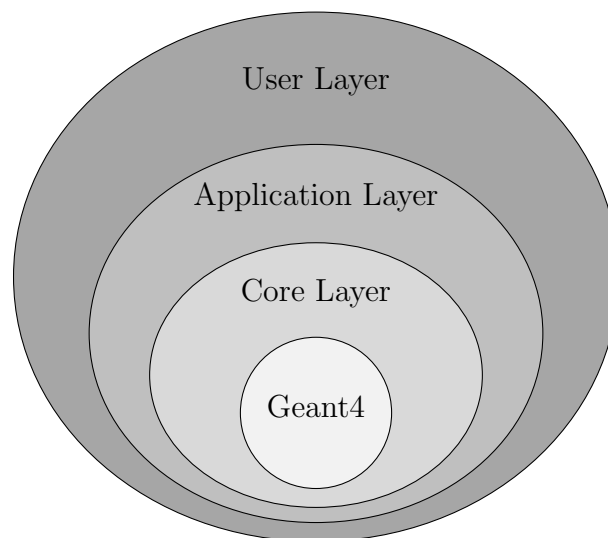


Figure 2.9: Structure of GATE. Where the core layer defines basic mechanisms available in GATE, the application layer extends base classes for specific modeling and the user layer initiates the simulation by using scripts.

The core layer represents base classes that explain the construction of geometry, the interaction physics, visualisation and time management. The application layer extends on these base classes at the core layer to model specific objects or processes. For example the base class for volumes is at the core layer, where the application layer defines the specific volume types like a box or a sphere and how they can be translated. The user layer allows the running of the simulation in an interactive

mode or by executing a macro script. Generally the macro script will consist of the Geometry definition (the Scanner and Phantom), the source distribution, physics processes and time management.

A particular novel approach used by GATE is its Activity definition. By using the Geant4 General Particle Source class, GATE defines the source properties such as activity, its particle type (radionuclide, gamma, positrons, etc.), energy distribution, half life, position and direction. One interesting thing about GATE is the use of a virtual clock. At random time intervals δt , events that occur are sampled from equation 2.17 which is the probability of the source activity at time t , where $A(t)$ is the source activity at time t . This allows for modelling of dynamic systems (e.g. respiratory motion).

$$P(\delta t) = A(t) \cdot e^{-A(t)\delta t} \quad (2.17)$$

The Geant4 code allows accurate modeling of particles and their interactions in GATE. These include modeling of; Photons, Electrons, electron-positron annihilation, Bremsstrahlung, Photoelectric effect, Compton scattering, Rayleigh scattering, Ionisation and Møller scattering. For positron emission two modules are used. The first module randomly generates the positron energy from the measured β^+ spectra, making use of the Neumann algorithm [100]. The speed of the simulation is increased here because it bypasses the decay of radionuclide process used by Geant4. The β^+ spectra of ^{11}C , ^{15}O and ^{18}F have been parameterised in GATE. The second module takes into account annihilation photon acollinearity i.e. the angular deviation of the annihilation photons from 180.00° . To reproduce results found experimentally by Iwata et al. [102] a Gaussian blur with a FWHM of 0.58° is applied.

Since the release of GATE version 6 [103] significant work has been made to implement the three electromagnetic packages *standard*, *Low energy* and *PENELOPE*. In each of these libraries the energy loss of photons is due to discrete interactions only.

The electron energy loss is tracked through continuous energy loss and secondary electron production. It should be noted that the multiple scattering algorithms used in the *PENELOPE* code are not yet implemented in GATE.

One of the largest criticisms of GATE has been its relatively long simulation times compared to other Monte Carlo packages such as EGS4 [104]. To increase the efficiency of GATE a number of authors have applied different techniques to reduce simulation times including cluster computing and variance reduction techniques. De Beenhouwer et al. [105] have developed software to split GATE macros for implementation on a computer cluster. Other authors have used similar macro splitting approaches to reduce simulation times such as Staelens et al. [106] and Jan et al. [107].

The classic variance reduction technique of particle *splitting* and *Russian roulette* have also been introduced into GATE version 6. When a particle has a relatively high probability of depositing its energy the particle is split into n particles each having the same characteristics as the original except each is weighted by the fraction $1/n$. If the particle has a relatively low probability of depositing its energy then the Russian roulette scheme may kill the particle.

Taschereau and Chatziioannou [108] have also applied a compressed voxel strategy to reduced simulation time. The method fuses adjacent voxels together that have identical physical properties in an aim to reduce the memory and CPU requirements on the Monte Carlo simulation.

2.13 Applications of GATE

In the main, GATE has been used to assess molecular scanner performance compared to protocols such as the National Electrical Manufacturers Association (NEMA) standards [109, 110, 111]. GATE has been shown to be useful in the continuing development of not only PET and SPECT optimisation but also preclinical small

animal scanners [112, 113]. There have been a number of dedicated PET systems validated in GATE. These include the ECAT EXACT HR+ (CPS Innovations) [107, 114], the PET components of the PET/CT scanners like the Allegro/GEMINI PET scanner (Philips Medical systems) [115], the Biograph 6 PET scanner (Siemens medical systems) [114, 116] and the Advance/Discovery LS PET scanner (GE Healthcare) [117]. One point of interest is a trend in the literature to see improved spatial resolution in all simulations compared with experimental values. Karakatsanis, Lamare and Schmidtlein [114, 115, 117] go on to comment that this is likely to be due to the inability of GATE to model the inherent limitations of the resolution of Photomultiplier tubes (PMTs) and the modeling of light sharing, and light scatter between PMTs. By adding an analytical Gaussian blurring function these underestimates can be accounted for [114, 117]. Commercially available SPECT scanners such as the DST-XLi, Millennium VG Hawk-Eye (both GE Healthcare) [118] and the Axis/Irix (Philips Medical systems) [119, 120] SPECT scanners have also been modelled in GATE. Particular attention is paid to collimator design and septal penetration in the evaluation of these models, as well as matching the modelled and measured energy spectrum.

The application of GATE to image reconstruction optimisation in both SPECT [121] and PET [122] has also been shown to be useful. For example He et al. [123] investigated correction for respiratory motion using GATE and list mode driven data reconstruction.

Dosimetry applications of GATE have been investigated by a number of authors [104, 124, 125, 126]. Visvikis et al. [104] was one of the first to compare GATE to other codes such as MCNP and EGSnrc. By using Geant low-energy electromagnetic library they benchmarked GATE using the method proposed by Rogers et al. [127]. Two separate beams of 18 MeV photons and 20 MeV electrons were tracked through slabs of different materials (water, aluminum, lung and water). The overall dose uncertainty in results between MCNP and GATE were similar. Benchmarking did

show that GATE was 18 times slower than EGSnrc. This is due to the large number of variance reduction techniques used in EGSnrc. Visvikis used a version of GATE pre-2006 and since this time additional variance reduction techniques have been added to GATE which include photon splitting.

Validation of the standard electron transport algorithm in Geant4 (version 4.8.1) for use with GATE was conducted by Ferrer et al. [124]. They found that by calculating dose point kernels, the standard electron package was in agreement with MCNPX (a variant of MCNP) and other published values for electron energies greater than 50 keV. At 10 keV, the result accuracy became questionable. They also found that when scoring very thin regions ($\sim 1 \mu\text{m}$) results again did not agree with the MCNPX values. For imaging systems this is not of high importance as the range of 10 keV electrons in water ($2.5 \mu\text{m}$) is much less than the spatial resolution of a SPECT or PET scanner. Ferrer et al. also state that this is unlikely to impact significantly on dose calculations performed at the organ scale for conventional nuclear medicine isotope dosimetry. It should however be noted that the Geant4 *low energy* and *PENELOPE* packages were not tested, and are more suitable for dosimetry at lower energies. The effect of the standard *low energy* package on conventional nuclear medicine will be assessed in chapters 4 and 5.

The *low energy* package was however compared with the standard package in the GATE platform by Thiam et al. [125]. The authors used GATE to model the *low energy* photons from Iodine-125 used in brachytherapy. They compared values in GATE to results from the AAPM Task Group Report Number 43 [128] and found that the maximum relative difference between the AAPM report and the *low energy* package was 1% where the *standard* package was 7%. Currently no published data compares the Geant4 *PENELOPE* modules to the other *low energy* packages under the GATE platform, however this has been extensively compared in Geant4 [129]. It has been shown that the Fortran version of *PENELOPE* is the equal of EGSnrc [130, 131] and as mentioned above, the *PENELOPE* code was re-engineered

and validated in Geant4 by the creators of *PENELOPE* [97, 99]. Taschereau and Chatziioannou [126] have applied GATE and the *PENELOPE* package to absorbed dose calculations in a mouse phantom for ^{18}F -FDG, ^{18}F -FLT and $^{18}\text{F}^-$ (Fluoride ions).

2.14 Chapter Summary

This chapter has introduced background information on internal radiation dosimetry. Particular attention has been paid to aspects of the MIRD schema related to accurate absorbed dose calculations. The influence of the MIRD committee on the topic is demonstrated by the numerous relevant pamphlets produced and the popularity of the MIRDOSE and OLINDA\EXM dosimetry codes.

The Monte Carlo method has also been introduced for its ability to track the absorption of energetic radiation. Publicly available well documented Monte Carlo codes such as EGS, MCNP and Geant4 have also been introduced. Evidence from the literature has been provided to suggest that the use of Geant4 Application for Tomographic Emission (GATE) to internal dosimetry problems is plausible.

Chapter 3

Method

The main objective of this chapter is to establish a method for validating GATE and defining the methodologies used for investigating dosimetry of model and patient based voxelised phantoms in the GATE toolkit.

Patient specific Monte Carlo based dosimetric methodologies can potentially incorporate minimal assumptions compared to scaling model based dosimetry methods. The use of GATE as a dosimetry tool was introduced within the review of GATE related literature in section 2.13. A full understanding of the application of GATE to specific situations is required in order to establish the necessary level of confidence in the simulation results. This chapter provides a methodology for both the rigorous assessment of GATE and its application to patient specific dosimetry calculations.

Section 3.1 describes the processes involved in running GATE simulations in this work. Sections 3.2 through 3.5 establish the methodology used to simulate the MIRD [22] spheres using both mathematical and voxelised defined spheres. By comparing these to the original MIRD values, other Monte Carlo codes or published literature, a decision as to which of the three Geant4 electromagnetic physics packages is most suitable is made. The implementation of voxelised phantoms that define different source and target regions are discussed in section 3.6. The reasons for simulating different voxel sizes will be discussed. The methods used in the preparation of XCAT

and patient data sets are described in sections 3.7 through 3.9. Section 3.10 provides details for the calculation of DFs for the XCAT and patient simulated results.

3.1 Simulations in GATE

The following describes the processes involved in running the GATE simulations in this work. Simulations in GATE versions 3.1.2 and 6.0p01 have been investigated. Table 3.1 shows the version numbers of required libraries and software that have been used.

Table 3.1: GATE and GATE related software versions

	geant	clhep ^a	root
GATE v3.1.2	4.9.1p02	2.0.3.2	5.20
GATE v6.0p01	4.9.2p02	2.0.4.2	5.20

^a Class Library for High Energy Physics

Simulations were submitted to the Victorian Partnership for Advanced Computing (VPAC) computer cluster “Tango” [132]. At the time of simulation Tango was fitted with 111 compute nodes. Each node was fitted with 2 AMD 2356 Quad Core Opteron processors [133], giving a total of 888 cores. Tango runs a Linux operating system (CentOS 5 64-bit) and job scheduling is controlled by the Portable Batch System software OpenPBS.

A macro language is used to pass commands on geometry, physics, etc. to the GATE environment. Macro files are ASCII files with the extension “.mac” and can be executed from the GATE command interpreter, from within another GATE macro file or using the macro file as an argument of the GATE command line executable. In the case of this work all GATE simulations were executed from the command line or more specifically in the cluster environment through a bash script submitted to the job scheduler. An example of this PBS script is shown in Appendix A.1.

3.2 The MIRD Benchmark of GATE

An approach to initial validation is to investigate historical benchmarks that have not previously been reported in GATE. The MIRD scheme for internal dose calculations was introduced in section 2.3. Benchmarking GATE against methods documented in the MIRD pamphlets [21, 22] will give not only testable results for GATE, but also insight into where original values in the MIRD pamphlets have evolved. Specifically a key benchmark would be the performance of GATE in calculating absorbed fractions for the “MIRD spheres”. Comparisons to the MIRD spheres are not limited to GATE but can be compared against published data using different Monte Carlo codes.

Absorbed fractions for simple geometric shapes containing photon-emitting radioactivity are described in the MIRD pamphlets 3 and 8 [21, 22]. The pamphlets calculate absorbed fractions of uniformly distributed sources and point sources located centrally in homogeneous spheres, ellipsoids and cylinders. The two pamphlets differ in the size of these simple geometries. For example, sphere masses in pamphlet 3 range from 0.3 kg to 6.0 kg. Where pamphlet 8 calculates spheres of mass ranging from 1 g to 100 g.

Although a large variation of shapes and sizes were originally calculated, it is realistic for this benchmark to concentrate on values obtained from pamphlet 8. In particular, unit density spheres of uniformly distributed radioactivity emitting photon energies ranging between 0.03 MeV and 2.75 MeV. Spheres were chosen due to the availability of additional literature, namely Stabin and Konijnenberg [1] and can be compared with analytically determined values. Spheres were also compared to a simple Monte Carlo code created for this work (Appendix C). Values for ellipsoids have not been calculated as more complex geometries are calculated in following chapters.

Uniformly distributed radioactivity has been chosen over point sources. In comparison to point sources, pamphlet 8 states that there is a small increase in

error for uniformly distributed sources of radioactivity. Round off errors are cited for the resulting increased uncertainty. The error occurs in the calculations made for the absorbed fraction compared to the specific absorbed fraction [22]. From the literature [104, 124, 125] differences in the most accepted Monte Carlo codes are largest at small volumes and low energies. The likely reason is due to the different implementation of the physics in the codes themselves and particularly the boundary crossing models for electron transport simulations as well as multiple scattering algorithms. Therefore, to further validate GATE, unit density spheres of a mass ranging from 1 g to 100 g have been chosen over the larger spheres with a wide range of energies.

In this methodology the MIRD spheres are regions of interest in a homogeneous tissue-analog medium. This again allows for simple benchmarking in GATE. The composition of the tissue medium is shown in Table 3.2. This composition is used for comparison to the MIRD values for any simulation involving a homogeneous set-up.

Table 3.2: Tissue composition used in the MIRD pamphlets[21]

Element	Fraction of mass %
Oxygen	71.39
Carbon	14.89
Hydrogen	10.00
Nitrogen	3.47
Sodium	0.15
Chlorine	0.10

3.3 MIRD Spheres in GATE Version 3.1.2

Mathematically defined spheres using the Geant4 geometry manager were simulated for Spheres of mass ranging from 1 g to 100 g (the parameterized macro shown in Appendix A.2.1.) As the macro was parameterized, the sphere radius, initial photon energy and length of scan time could be entered from the command line. For

example:

```
Gate -a radius 0.620350 -a energy 0.14 -a time 15.0 spheres.mac
```

The physics library used in these simulations was the “standard” library. Photoelectric and Compton interactions are modelled for photons, however Rayleigh scattering is not. Secondary electrons were tracked to a distance of 30 cm which is much greater than the size of the spheres. X-rays generated from secondary processes were also modelled.

The output of this simulation is two ASCII files one containing the total number of events generated (“[*name*]Run.dat”) the second containing a history of events (“[*name*]Hit.dat”) that interact within the region of interest. The absorbed fraction is calculated separately using the two generated ASCII files and the simple python script *sum_energy.py* (Appendix A.2.2).

3.4 MIRD Spheres in GATE Version 6.0

The mathematically defined MIRD spheres have also been simulated in version 6.0p01 of GATE. The macro has only slight differences compared to the 3.1.2 version. A key difference however, is in the physics definitions. The three physics packages have been compared in GATE to find which is the most suitable to use in following applications. The results of the three physics packages compared to the gold standard for the MIRD absorbed fractions (presented by Stabin and Konijnenberg [1]) is shown in section 4.4. Appendix A.2.3 shows examples of implementing the different physics packages into GATE.

To assist with batch processing two additional scripts were written (Appendix A.2.4). The ASCII output files were processed using the same method described in section 3.3.

Furthermore a minimalistic speed benchmark to find how using a different physics package would effect the overall simulation time was completed in GATE version 6.0. The 100 g MIRD sphere was simulated with uniformly distributed activity of 140 keV photons. The simulation time for 10 runs of each physics package was completed. A total of 10^6 photons were generated in each run which was deemed to be sufficient for the purpose of evaluating the simulation speed.

3.5 Voxelised Phantom Validation

It is considered that voxelised phantoms are more useful for defining realistic human anatomy compared to traditional mathematical phantoms [25]. To extend the complexity of the GATE validation, the MIRD spheres are again simulated in GATE, however the spheres will be defined by voxels. Self absorption in the MIRD spheres is evaluated for spheres of mass ranging from 1 g to 100 g. Uniformly distributed activity is simulated for a photon energy of 140 keV. The three physics packages are again investigated individually in GATE version 6.0p01. From this data a choice as to which of the physics packages is the most appropriate for the simulation of voxelised phantoms will be made (section 5.2.2).

The influence of different voxel sizes to the calculated absorbed fractions are investigated by simulating each sphere mass with spheres being defined by individual voxels sizes ranging from 6.00 mm down to 0.25 mm. This broad range of voxel sizes are chosen to represent the current range of voxel sizes used in typical medical images and to investigate simulation accuracy dependence on voxel size.

The voxelised phantoms are converted into interfile format for implementation into GATE. Appendix A.3.1 shows the appropriate python code to create this voxelised phantom in interfile format. The center slice of each of the 60 g voxelised phantoms is shown in figure 3.1. It can be seen that as the voxel size decreases a more accurate representation is obtained for the sphere.

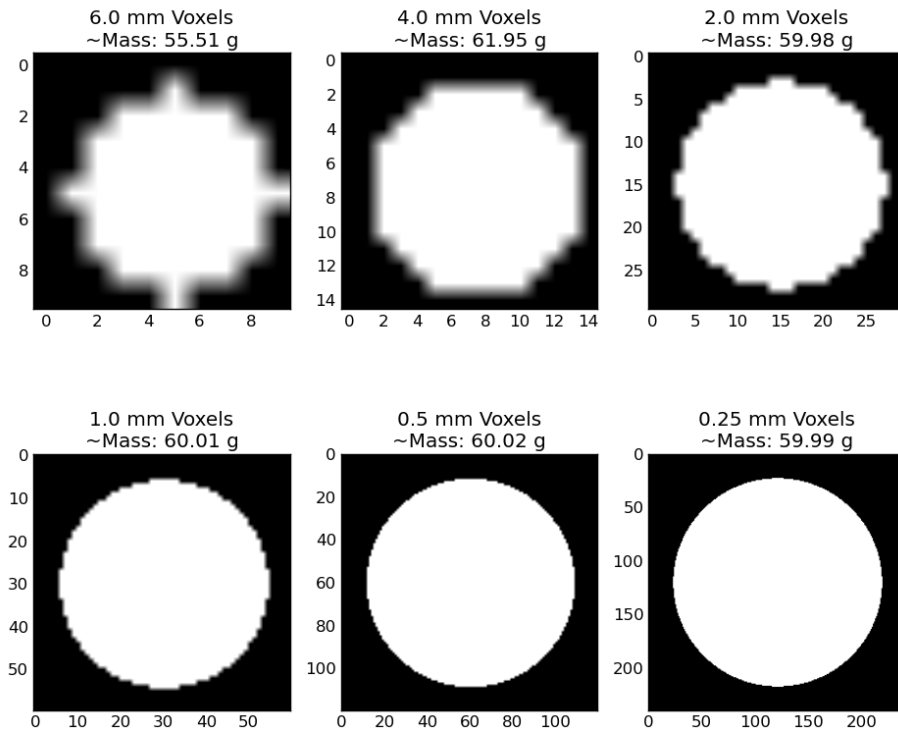


Figure 3.1: Center slice of voxelised sphere phantom for various voxel sizes.

Again a simple simulation speed benchmark (As defined in section 3.4) is completed for the 100 g sphere and 140 keV photons. A total of 10^6 photons were generated in each run. A voxel phantom with dimensions of 0.25 mm x 0.25 mm x 0.25 mm (referred to as 0.25 mm voxels) is used. 0.25 mm voxels were chosen as they increase the likelihood of differences in simulation speed being seen due to voxel to voxel boundary crossing.

3.6 Voxelised Source to Target

The absorbed dose in a neighbouring organ from a source organ makes an important contribution to the overall internal dosimetry assessment. The performance of voxelised phantoms have therefore been investigated for source to target regions in both homogeneous and heterogeneous medium.

3.6.1 Homogeneous voxelised simulation

A spherical source with a radius of 10 mm was embedded into a homogeneous medium 20 mm away from a second spherical target organ. The source and target regions were chosen to be voxelised spheres. Spheres have been used as square voxels are more likely to misrepresent a spherical volume. The homogeneous material was chosen to be water as compared to the MIRD tissue analogue (see Table 3.2).

A total of 10^8 events were simulated for 6 voxel phantoms with a voxel size ranging between 8.0 mm down to 0.25 mm. For each of these phantoms both 140 and 511 keV photons were simulated separately. The *low energy* physics package was also used. This decision arises from the results obtained in section 5.2.2. The center slice of the voxel phantoms are shown in figure 3.2, where the grey region is the source and the white region is the target. An incorrect volume definition of the spheres using square voxels is particularly obvious for a voxel size greater than 2.0 mm.

The output of each voxel simulation is a dose distribution in cGy with the same dimensions as the original input phantom. The absorbed dose was calculated by using a simple class presented in Appendix A.3.2. Put simply, the value of each voxel was converted to Gy, multiplied by its mass and then converted from Joules to MeV. The total energy in the region was then summed and the absorbed fraction found. From the Mean energy emitted per unit cumulated activity (Δ) the DF is also found.

For comparison, a geometric phantom and source of the same setup was simulated and the absorbed fraction found. Figure 3.3 shows visualisation output from GATE using OpenGL. It shows the geometric source region (red sphere) with gamma-ray photons (green line) and the geometric target region (blue sphere).

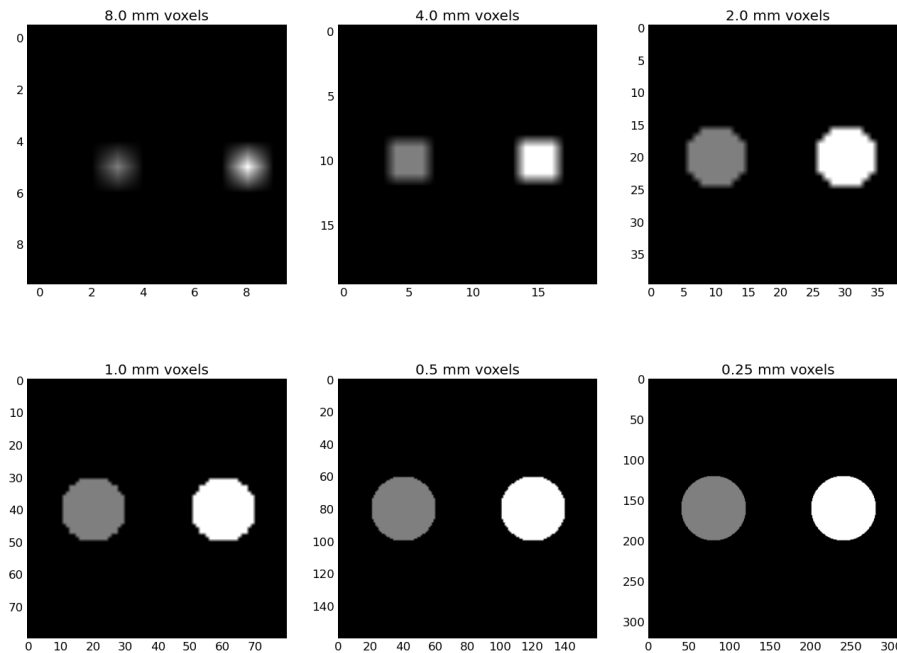


Figure 3.2: Center slice of voxelised source to target phantom for various voxel sizes

3.6.2 Heterogeneous voxelised simulation

A similar voxel approach is also described for a heterogeneous phantom. Again the source and target regions are spheres with a radius of 10 mm. The spheres are separated by two 10 mm thick slabs. Figure 3.4 shows a visualisation output from GATE using OpenGL. In this figure the red sphere is the source region and it is set to be a kidney analog. The blue sphere is the target region, where the material is set to be a liver analog. The magenta slab is a analog of lung tissue where the

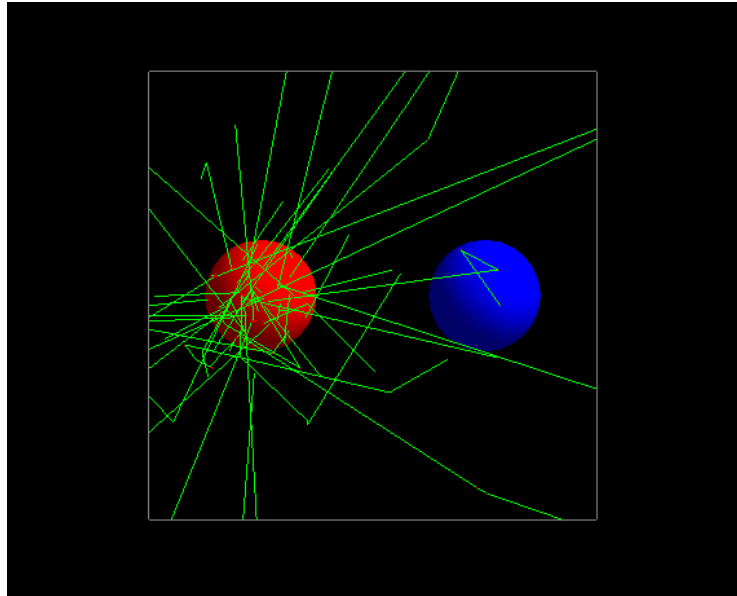


Figure 3.3: OpenGL illustration produced from GATE of the source and target spheres in a homogeneous medium. It shows the geometric source region (red sphere) with gamma-ray photons (green line) and the geometric target region (blue sphere).

yellow slab is an adipose (Fat) analog. These regions are surrounded by air. The composition of each material is shown in Table 3.3.

Table 3.3: Element compositions of the material used in the heterogeneous phantom.

Material	Density $\text{g}\cdot\text{cm}^{-3}$	Percentage of Element Mass										
		H	C	N	O	Na	P	S	Cl	K	Ca	Ar
Lung	0.26	10.3	10.5	3.1	74.9	0.2	0.2	0.3	0.3	0.2		
Adipose	0.92	12.0	64.0	0.8	22.9		0.2					0.1
Kidney	1.05	10.3	13.2	3.0	72.4	0.2	0.2	0.2	0.2	0.2	0.1	
Liver	1.06	10.2	13.9	3.0	71.6	0.2	0.3	0.3	0.2	0.3		
Air ^a	1.29 ^b		0.0	75.5	23.2							1.3

^a Values are rounded to 1 decimal place

^b Density $1.29 \text{ mg}\cdot\text{cm}^{-3}$

A total of 10^8 events are simulated for 6 voxel phantoms with a voxel size ranging between 8.0 mm down to 0.25 mm. For each of these phantoms both 140 and 511 keV photons are simulated. The *low energy* physics package was again used.

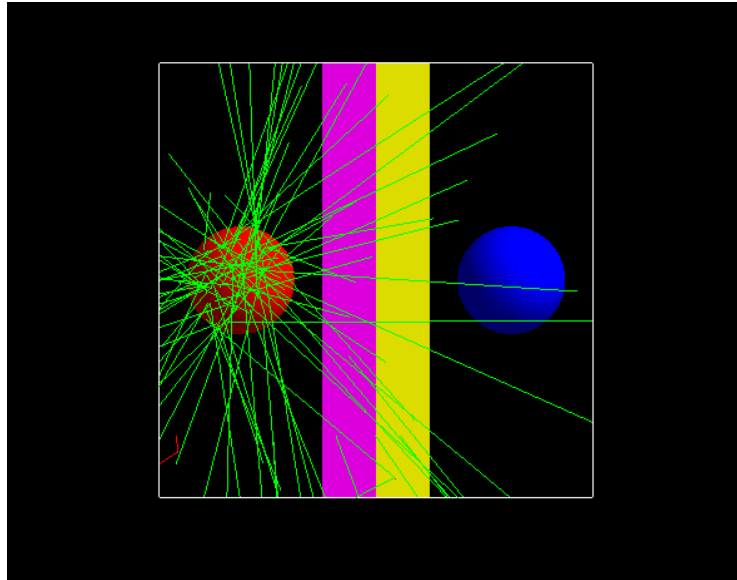


Figure 3.4: OpenGL illustration produced from GATE of the source and target spheres in a heterogeneous medium. The red sphere is the source region and it is set to be a kidney analog. The blue sphere is the target region, where the material is set to be a liver analog. The magenta slab is an analog of lung tissue where the yellow slab is an adipose (Fat) analog.

3.7 Realistic Dosimetry Situations

The previous sections of this chapter have established a methodology to validate GATE and in particular the choice of electromagnetic physics package. Methods for extending the use of GATE in potentially more clinically relevant situations, using both a standardised model of human anatomy and true patient data are described in the remainder of this chapter. Preparation of the XCAT phantom and true patient data are described in sections 3.8 and 3.9.

3.8 XCAT Phantom Preparation

The XCAT phantoms were created by using the program *dncat_bin* with small variations to the sample male input parameters included with the XCAT distribution (male.smap.par). The phantom height was not changed from 175 cm, while the phantom weight was varied by scaling both organ masses and total body fat content

to produce three different patients weighing 95.05^1 kg, 69 kg and 51 kg. This is equivalent to a standardised model of 3 male patients with a body mass index of $31.0 \text{ kg}\cdot\text{m}^{-2}$ (large), $22.5 \text{ kg}\cdot\text{m}^{-2}$ (average) and $16.7 \text{ kg}\cdot\text{m}^{-2}$ (small).

The activity definitions in the *dncat.bin* input file are changed so that the variables, 'kidney_activity' = 500 and 'liver_activity' = 100. All remaining activity related parameters are then set to 0. These values are chosen for ease of organ identification for not only defining the voxelised source in GATE but also for use as a voxel mask for the absorbed dose calculations. Unlike sections 3.1 to 3.6 where only photons had been simulated the realistic dosimetry models have been simulated using a Fluorine-18 source. The implementation of this source into GATE is shown in figure 3.5.

The ion source type in GATE is used to simulate any ion by defining its atomic number ($Z = 9$), atomic weight ($A = 18$), ionic charge in units of energy ($Q = 0$), and its excitation energy in keV ($E = 0$). This definition incorporates both the radioactive decay and atomic de-excitation. This is the most 'realistic' way of simulating a radio-nuclide in GATE.

```
/gate/source/voxel_ncat/gps/particle ion
/gate/source/voxel_ncat/gps/ion 9 18 0 0
/gate/source/voxel_ncat/gps/monoenergy 0. keV
/gate/source/voxel_ncat/setForcedUnstableFlag true
/gate/source/voxel_ncat/setForcedHalfLife 6586 s
```

Figure 3.5: GATE code to implement a Fluorine-18 source.

Finally for each of the XCAT phantoms the voxel size is also varied. Table 3.4 shows the varied parameters concerning the XCAT dimensions. The output obtained for *dncat.bin* was two 32-bit floating point images (attenuation and activity maps) and a log file. The center coronal slice of the 95.05 kg XCAT phantom is shown in figure 3.6 for the different voxel sizes 1 mm to 16 mm voxels. XCAT phantoms with

¹This is the weight of the visible male from the visible human project[57] and also the default weight in the male.smap.par file distributed with XCAT

voxel sizes of 0.6 mm and 0.4 mm are also investigated for voxel sampling of self dose in the kidneys. At such small voxel sizes (i.e. 0.6 mm and 0.4 mm) it was not possible to investigate organ cross dose due to computational limitations.

Table 3.4: Voxel and array dimensions of the XCAT phantom.

pixel width (mm)	slice width (mm)	array size	start_slice	end_slice
0.4	0.4	560	3040	3400
0.6	0.6	374	2027	2267
1.0	1.0	400	1121	1520
2.0	2.0	200	561	760
4.0	4.0	100	281	380
8.0	8.0	50	141	190
16	16	25	71	95

Each image is converted into 16-bit unsigned integer format for implementation into GATE. The attenuation map is scaled so that the value that defines the skull bone is equal to 32768. The value 32768 was chosen to assist with file conversion. The maximum pixel value possible for a 16-bit signed integer ($2^{15}-1$) is 32767, which in the CT image corresponds to the material with the highest linear attenuation. GATE however requires 16-bit unsigned integer format, which allows for a maximum value of 65535 ($2^{16} - 1$). As skull bone is expected to have the highest linear attenuation this is set to one over the maximum value allowed for a signed integer therefore making any error in the data type conversion visible. From the log file an appropriate interfile header is also created. The activity and material range tables used in GATE for the converted images are shown in figure 3.7. The GATE toolkit reads the interfile image and uses the material range table to allocate pixel values to the relevant material.

3.9 Preparation of Patient Data

A routine clinically acquired ^{18}F -FDG PET/CT scan has been used as a basis for a retrospective calculation of the mean absorbed dose per unit of cumulated activity.

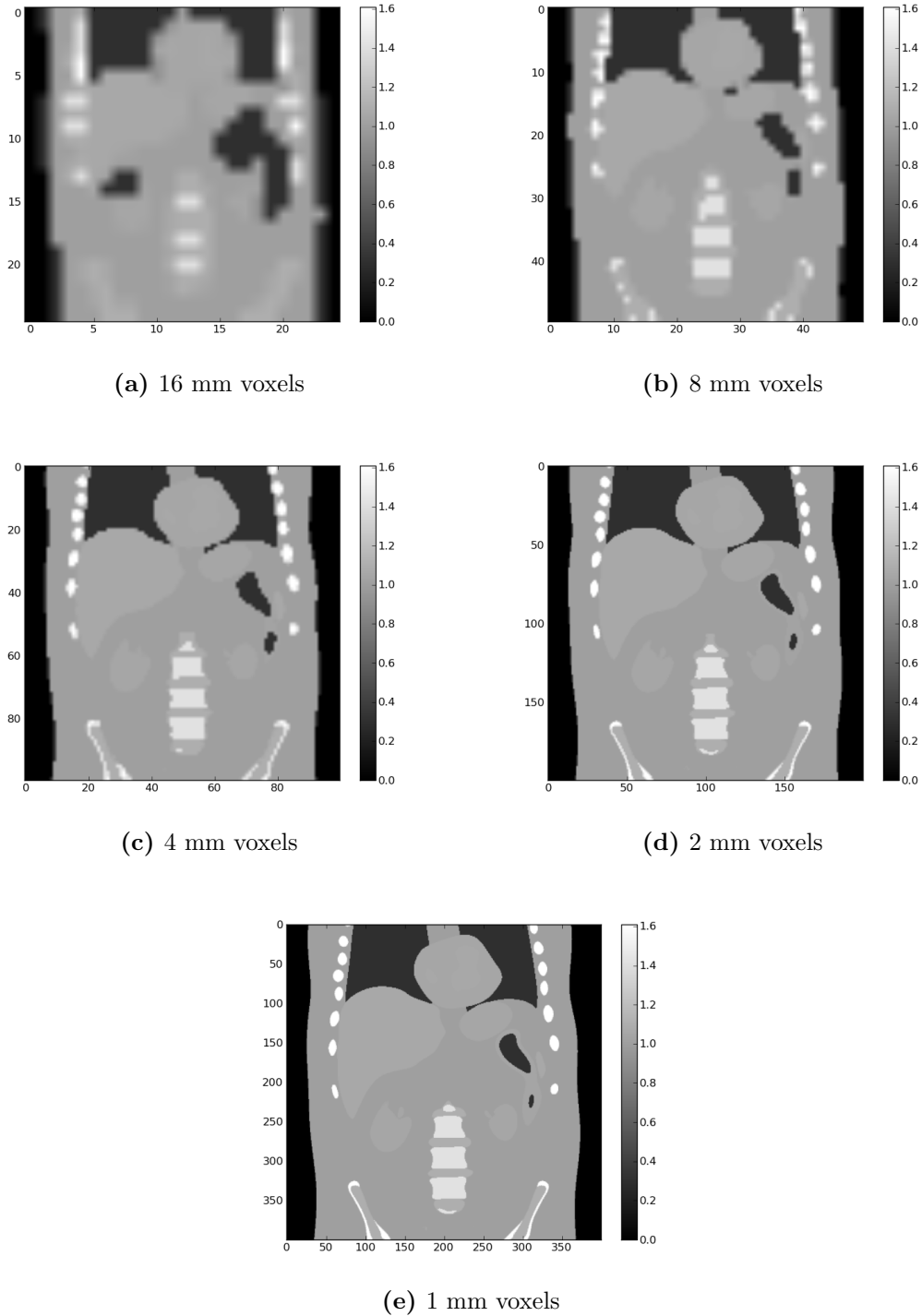


Figure 3.6: Centre slice of the 95.05 kg XCAT phantom with varying voxel sizes. In units of density $\text{g}\cdot\text{cm}^{-3}$

Activity Range Table:

```
2
20 105 0.0
105 501 1.0
```

Materials Range Table:

```
12
0      3065  Air      false 0.0 0.0 0.0 1.0
3065  13011 Lung     false 0.0 0.0 0.0 1.0
13011 20566 Adipose  false 0.0 0.0 0.0 1.0
20566 21525 Body     false 0.0 0.0 0.0 1.0
21525 21819 Intestine false 0.0 0.0 0.0 1.0
21819 22048 Pancreas false 0.0 0.0 0.0 1.0
22048 22177 Muscle   false 0.0 0.0 0.0 1.0
22177 22292 Kidney   false 0.0 0.0 0.0 1.0
22292 22736 Liver    false 0.0 0.0 0.0 1.0
22736 24154 Cartilage false 0.0 0.0 0.0 1.0
24154 27562 SpineBone false 0.0 0.0 0.0 1.0
27562 31336 RibBone   false 0.0 0.0 0.0 1.0
31336 32768 SkullBone false 0.0 0.0 0.0 1.0
```

Figure 3.7: Activity and Materials range tables used in GATE for the XCAT phantoms

The patient was a 75 year old male who was administered 365.75 MBq of ^{18}F -FDG 70 minutes before the acquisition of the PET scan. The patient weighed 69 Kg and was 165 cm tall.

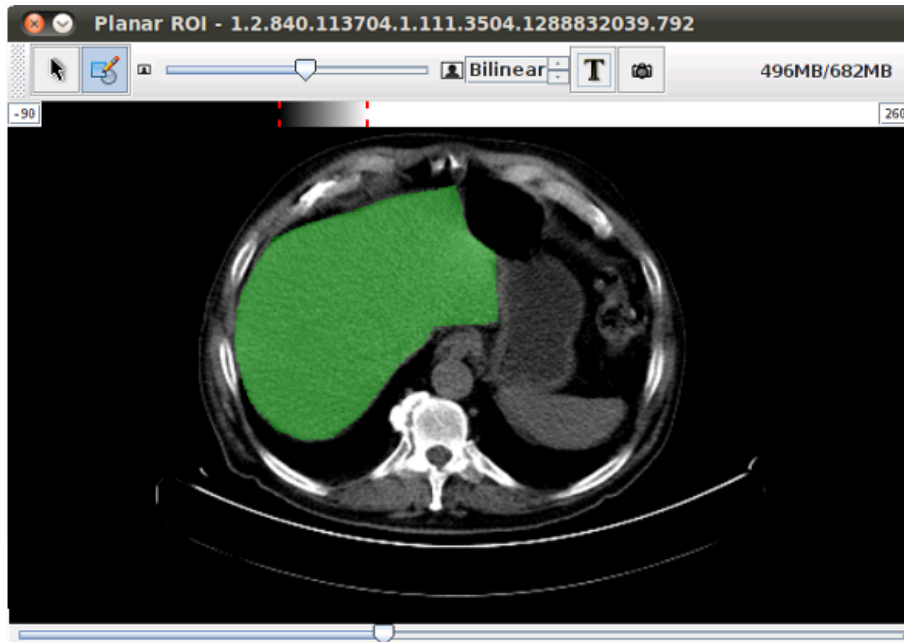
Images were acquired using the Phillips Gemini PET/CT scanner. A total of seven emission bed positions were acquired with three minutes per bed position giving a total scan time of 21 min. PET images were then reconstructed with a 3D Row Action Maximum Likelihood Algorithm (3D-RAMLA [134]), the PET reconstructed voxel size was 4 mm x 4 mm x 4 mm. The Gemini scanner has the ability of using ^{137}Cs attenuation correction however only CT attenuation correction was used. The helical CT attenuation scan had scan parameters of 60 mA, 30 sec exposure time, pitch of 1.5 and 140 kVp. The reconstructed CT voxel size was 1.17 mm x 1.17

mm x 6.5 mm. The PET and CT images are inherently co-registered with identical patient positioning and coordinate system. Regular quality control of the Gemini PET/CT ensures co-registration between the PET and CT gantries. PET images were obtained in ugm (a vendor specific file format used by the Philips Allegro PET Scanner) format while CT images were obtained in dicom format.

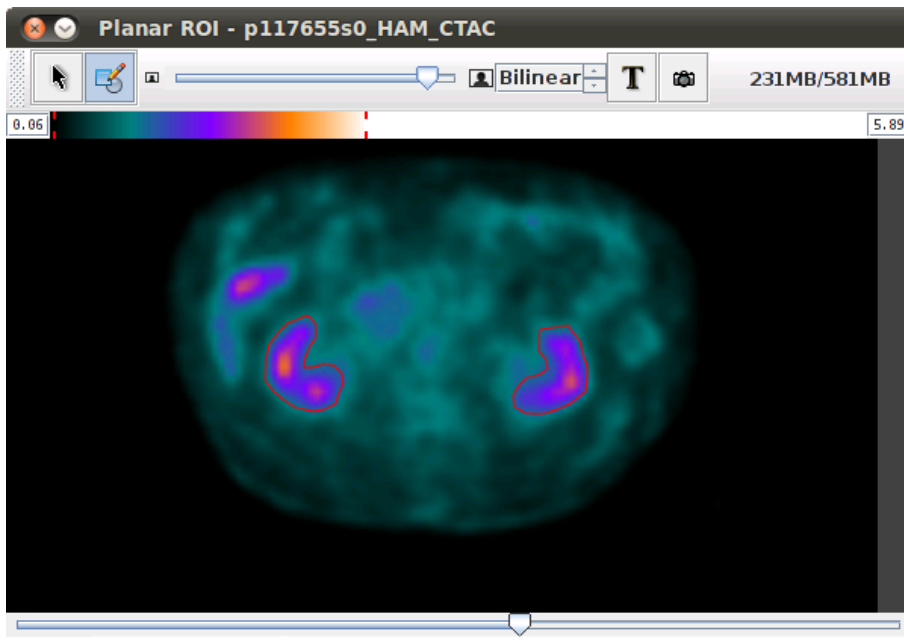
3.9.1 Manual organ segmentation

In the XCAT phantoms the liver and kidney regions are well defined by using the activity file. For patient data it is required to segment regions or organs of interest. The approach used in this thesis was to draw manual regions of interest. A number of automated and semi-automated (seed function) approaches have been applied to organ segmentation by a number of authors [47, 135, 136, 137, 138], however these methods are often limited by the resolution of the modality i.e. CT and MRI.

Organ regions were drawn manually by the author using an in-house, medical image quantitative analysis and visualisation package called Wasabi (written in Java) [137]. Regions were drawn on the CT image and then transferred to the PET image. The defined regions were then used to define a mask with the same dimensions as the original PET and CT files. Figure 3.7 shows examples of the regions drawn, it shows that windowing of the images was used to assist with highlighting a defined organ boundary.



(a) Example of the liver region shown in green on the CT image. The pixel values have been windowed to a range of -90 to 260, this helps with drawing the region. Regions are drawn along each slice for both the kidneys and the liver.



(b) Example of the kidneys are shown inside the red regions on the PET image. The pixel values have been windowed to a range of .06 to 5.89, this helps with defining the edges of the organ. Regions have not been filled so that the non-uniform activity distribution is clearly seen.

Figure 3.8: Regions of interest of the patient phantom using Wasabi

3.9.2 Voxel attenuation map

The voxel attenuation map was converted from dicom format to interfile format. Dicom formatted CT images are 16-bit signed integer representation of Hounsfield units. As GATE requires images in 16-bit unsigned integer format each pixel is added by 1000 so that Air is represented by 0 in the interfile. The range table was then set directly from the interfile and is a direct representation of the density of each material.

3.9.3 Voxel source distribution

The voxelised source is created from the PET data which is in units of SUV_{bw} . As identified in chapter 2 quantifying the actual activity in each voxel or organ is difficult, however some assumptions can be made to approach this problem. The actual cumulated activity in the GATE simulation will be the total number of events generated, therefore it is important to ensure that the source is a true representation of both its distribution and activity. The process used to obtain the voxelised source distribution follows a number of steps.

- The kidneys are segmented by applying the organ mask defined in Wasabi.
- Since the PET data file is in units of SUV_{bw} the activity per gram is found by scaling the standardised uptake value by $\frac{A_0}{M} \cdot 2^{-t/t_{1/2}}$.
- The activity per voxel (in MBq) is then found by multiplying each voxel by the density of the voxel ($\text{g}\cdot\text{cm}^{-3}$) and the voxel volume (cm^3).
- Finally the source distribution is converted to Bq per voxel and saved in interfile format (16 bit unsigned integer).

An activity range table that increases linearly with pixel value is therefore applied for GATE implementation. It should be noted that the activity per voxel is converted

to Bq to maintain the distribution from the original floating point number format to an unsigned integer. As a result, no scaling (i.e. maximum pixel value scaled to a value of 32768) of the pixel values is required. Although GATE has the ability to set time activity curves to individual voxels this feature was not used, since the PET data is effectively a ‘snapshot’ in time and therefore biological clearance was not modeled.

3.10 Calculating the DFs

The procedure for calculating the absorbed fractions or DFs from a voxel phantom in GATE is the same regardless of complexity of the voxel data. Using the interfile method for dose calculation in GATE the resulting output file is a dose histogram with the same dimensions as the entered interfile, with units of cGy.

The first step is the creation of a voxel map that represents the mass distribution of the phantom. This is created by using the volume of the voxel multiplied by the density of the material that the voxel represents. Multiplying the mass of each voxel by the dose matrix gives the energy deposited in each voxel. A mask of the region of interest is applied to both the energy and mass matrix arrays where the sum represents the energy deposited in the region and the mass of the region.

Using the total energy emitted by the source, the mass of the region and the energy deposited in the region, the specific absorbed fraction is easily calculated. The total energy emitted by the source is known from the source definition. Also known from the source definition is the mean energy emitted per decay (Δ). From Δ the DF is also easily calculated. The calculation of the DF is a simple extension of the calculation method explained in section 3.6.1.

3.11 Chapter Summary

This chapter has defined a clear approach for validating GATE as a dosimetry tool. It proposes a simple benchmark of GATE using the MIRD spheres. A clear and objective way of choosing the most practical physics package used in GATE version 6.0 is also defined.

The XCAT phantom has been introduced as a powerful dosimetry tool that can be used to investigate the effects of changing organ mass sizes. By using the protocol defined for preparing patient data from a PET/CT data set, a method for calculating patient specific dosimetry calculations is possible in GATE.

The following chapters 4, 5 and 6 present the results of this method. They also discuss the relevance of the results.

Chapter 4

GATE: MIRDSpheres

4.1 Introduction

This chapter will describe results for calculating the absorbed fractions in the MIRDSpheres, the likely accuracy of the original values for the MIRDSpheres and finally some concluding remarks on the accuracy of the GATE simulated values with respect to EGS and MNCP (Stabin and Konijnenberg [1] refer to section 2.3) which are used as the gold standard.

4.2 Validation Results

Results of calculating the absorbed fractions in the MIRDSpheres using GATE are shown in this section. These results are discussed and the suitability of GATE as a framework for calculating absorbed fractions is validated.

4.2.1 GATE version 3.1.2

The absorbed fractions for spheres of different mass with uniformly distributed radioactivity are shown graphically in figure 4.1. Values for this figure are also presented to 3 decimal places in table B.1, Appendix B.

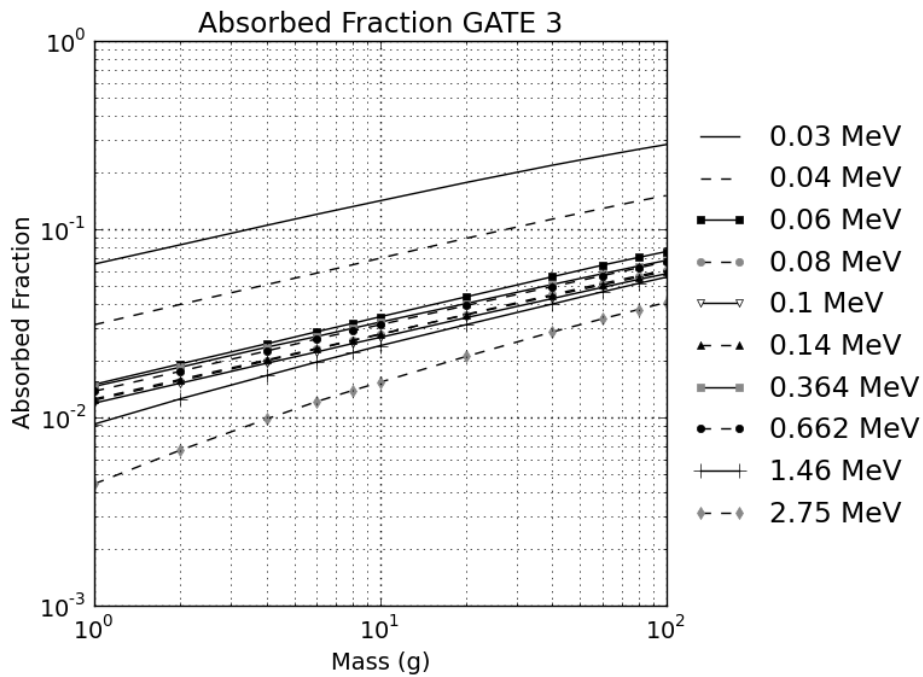
4.2.2 GATE version 6.0 comparison of physics packages

Using GATE version 6.0p01 the three physics packages have been used to find the absorbed fractions in the MIRD spheres. Results for photon energies ranging from 0.03 MeV to 2.75 MeV and sphere masses ranging from 1 g to 100 g are presented in table B.1 to 3 decimal places. Figures 4.2 to 4.4 show the three GATE version 6 physics packages compared to the GATE version 3 package for photon energies of 0.03 MeV, 0.10 MeV and 2.27 MeV as a function of sphere mass. From these figures and table B.1 it can be seen that the differences between the packages are only very small above 60 keV ($< 2\%$) and still reasonable below 60 keV (5%).

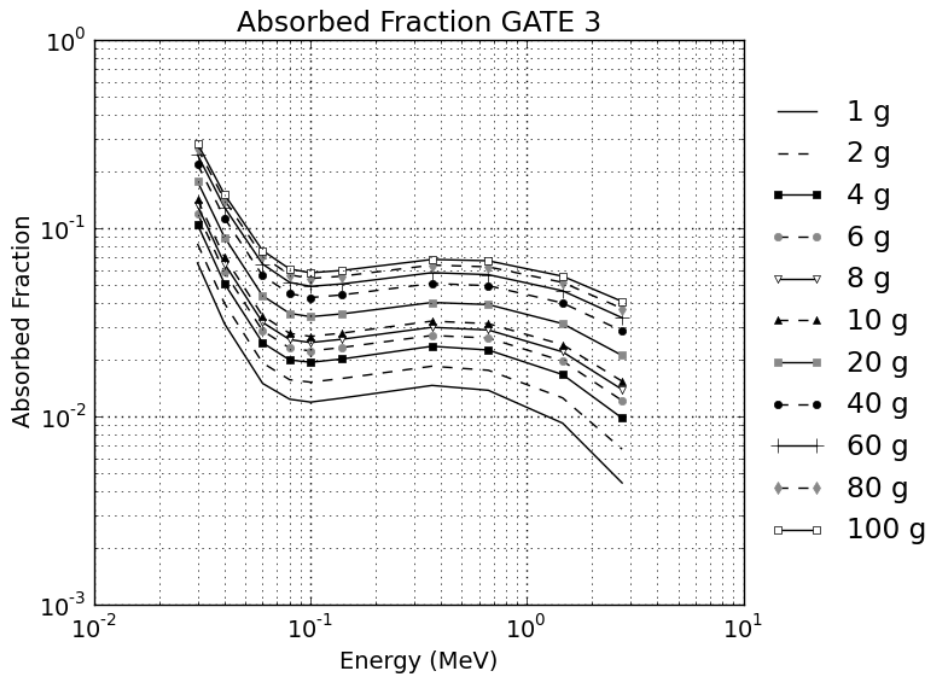
Additionally a comparison of the simulation speed for the different physics packages using a geometric sphere definition was completed. Table 4.1 shows results of the speed benchmark test described in section 3.4. A simple mean and standard deviation of the run times suggests that for a geometric phantom definition in GATE the *standard* physics package is significantly faster executing in about 50% of the time of the other packages. The difference between the *PENELOPE* and *low energy* package were smaller at 5–10%.

4.3 Accuracy of the MIRD Spheres

Since the release of MIRD pamphlet 8 in 1972, there have been a number of changes in modern Monte Carlo codes that may have affected the accuracy of the original



(a) Absorbed fractions as a function of sphere mass, GATE version 3.



(b) Absorbed fractions as a function of photon energy, GATE version 3.

Figure 4.1: Absorbed fractions in the MIRD spheres using GATE version 3.

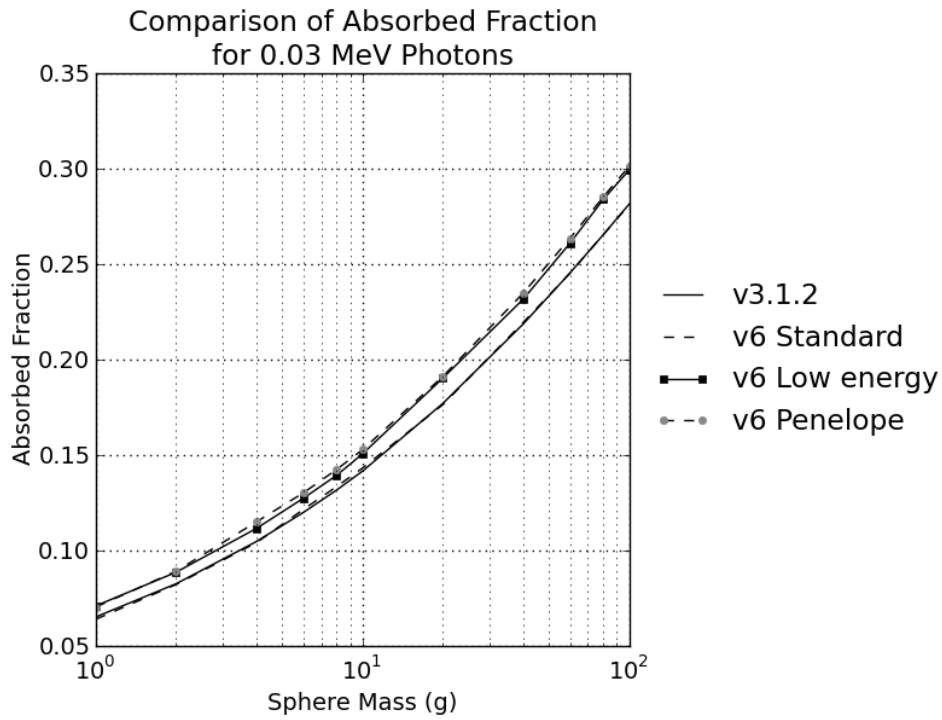


Figure 4.2: Comparison of the absorbed fractions simulated by the different GATE packages for 0.03 MeV photons as a function of sphere mass.

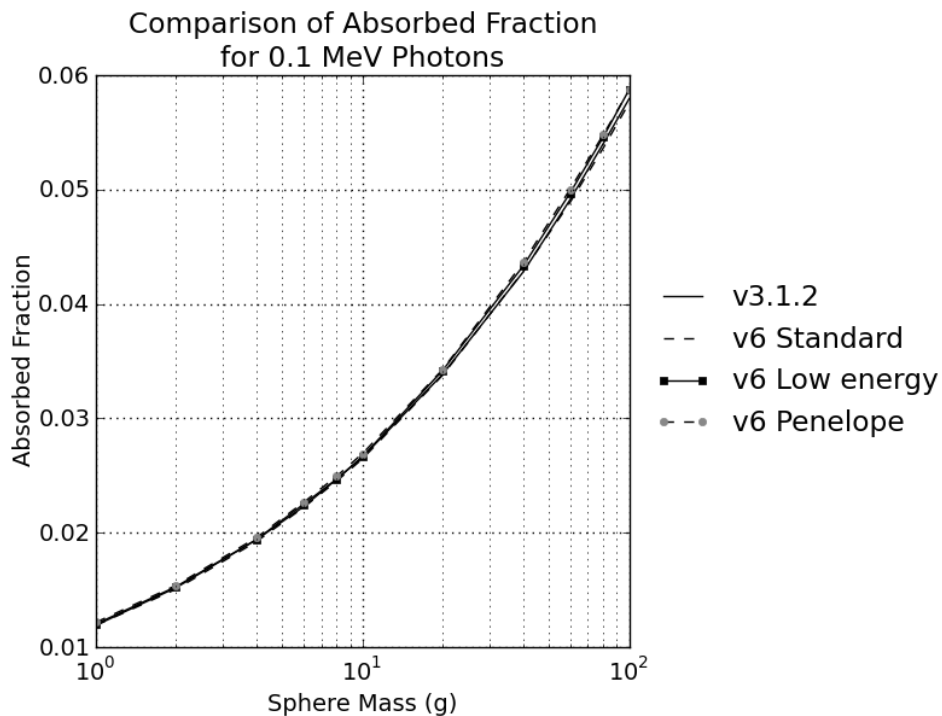


Figure 4.3: Comparison of the absorbed fractions simulated by the different GATE packages for 0.1 MeV photons as a function of sphere mass.

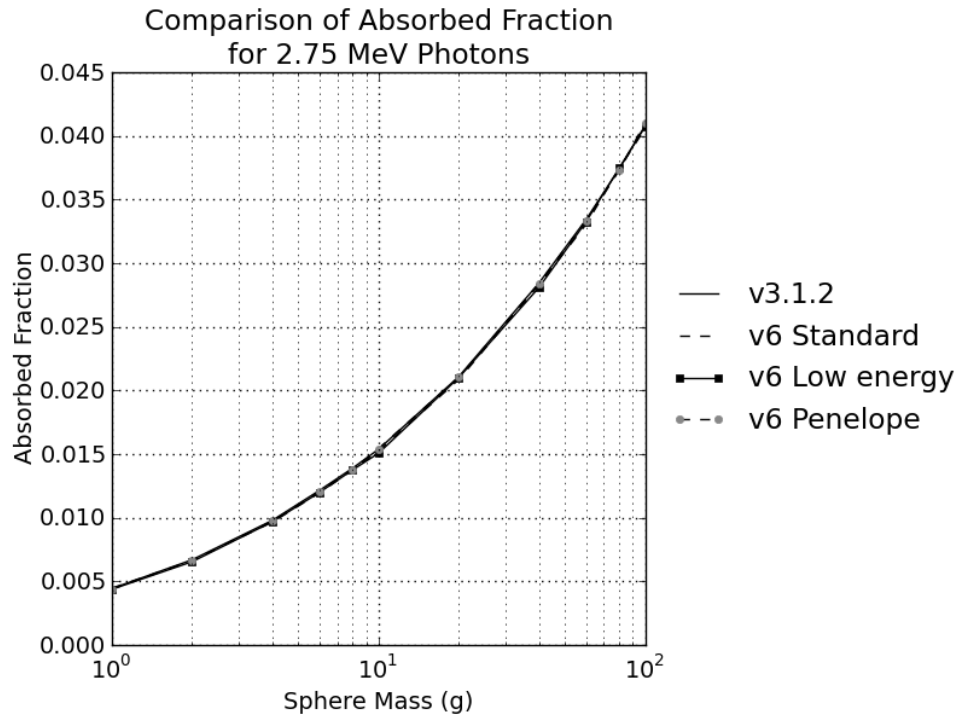


Figure 4.4: Comparison of the absorbed fractions simulated by the different GATE packages for 2.75 MeV photons as a function of sphere mass.

calculated values. Most notably are the effects of electron transport, increased accuracy of cross section data and to a lesser extent increased computational power. The original method for calculation of the absorbed fractions are explained briefly in MIRD 8 and in more detail in a review article by the same authors [139].

To assist in comparing the MIRD values with values simulated in GATE it is useful to pinpoint possible sources of error in the original MIRD values. The approach adopted was to write a Monte Carlo application that is very similar to that explained in the review article by Ellett et al. [139]. This very simple code was written in the python programming language [140] and will from this point be referred to as *track.py* (additional details are found in Appendix C).

Homogeneous unit density spheres with a mass range of between 1 g to 100 g were modelled with *track.py*. An energy range of between 0.03 MeV and 0.662 MeV of uniformly distributed radioactivity was also modelled. Figure 4.5 shows a comparison of the absorbed fractions as a function of mass between the MIRD pamphlets and

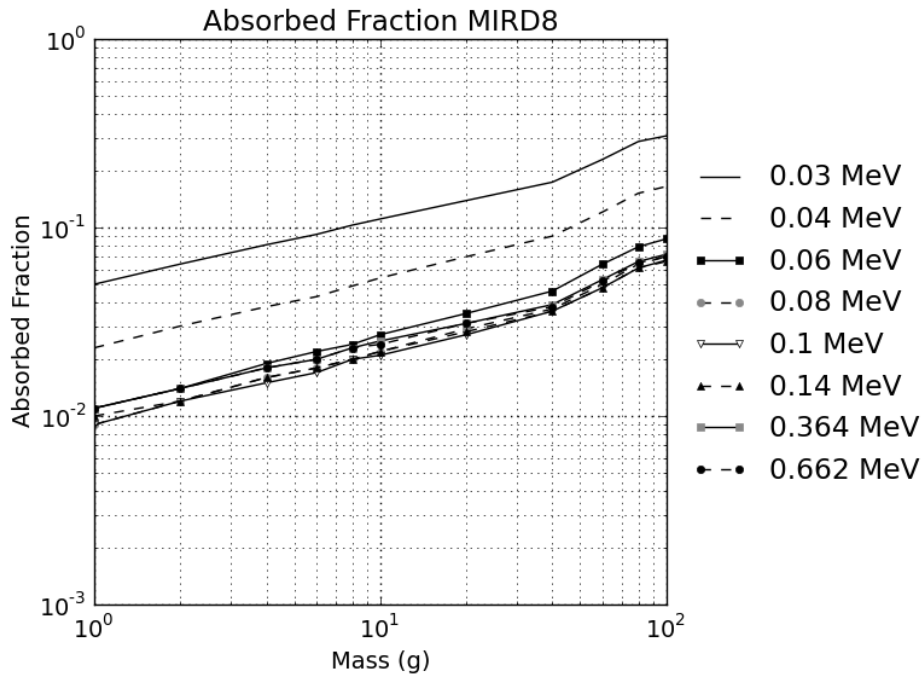
Table 4.1: Speed benchmarking of a geometric phantom for GATE version 6 physics packages

Run no.	<i>standard</i> (s)	<i>low energy</i> (s)	<i>PENELOPE</i> (s)
1	50.6	108.9	101.5
2	50.8	111.3	102.1
3	50.4	109.0	103.0
4	50.8	110.3	101.0
5	50.0	109.3	100.3
6	50.4	108.8	100.8
7	51.3	107.8	100.2
8	49.8	108.6	99.9
9	50.4	108.9	102.7
10	51.0	109.3	102.0
mean	50.5	109.2	101.4
standard deviation	0.5	1.0	1.1

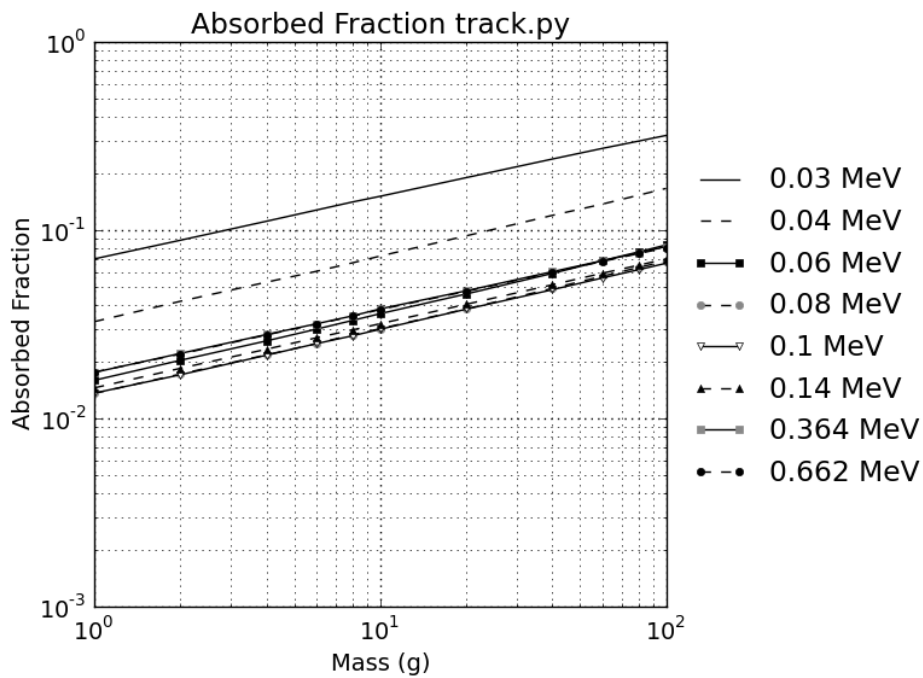
the simple code, where figure 4.6 is a function of energy.

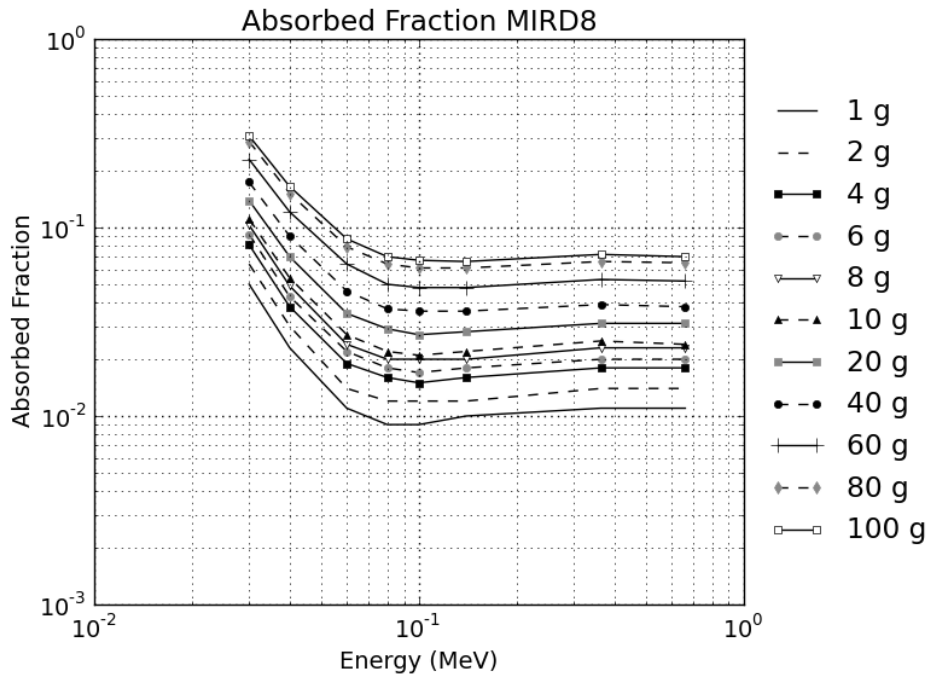
When figures 4.5a and 4.5b are specifically compared, there is a discontinuous change in the slope of the log-log plot in the original MIRD values for a sphere mass of 40 g to 100 g (figure 4.5a). This rise brings the MIRD values into better agreement with *track.py* for example for a photon energy of 0.03 MeV and sphere mass of 100 g the MIRD and *track.py* values are 0.306 and 0.319 respectively. Where at a sphere mass of 40 g the absorbed fractions for MIRD and *track.py* are 0.174 and 0.239 respectively. This trend is not as obvious when comparing figures 4.6a and 4.6b which plots mass as a function of energy. However when comparing the 1 g sphere on these figures it can be suggested that the original MIRD code must have introduced an underestimating bias for sphere mass of less than 40 g.

It should also be noted that for photon energies between 0.06 MeV and 0.662 MeV in figure 4.5a values unexpectedly cross. The reason for this is likely due to the fact that the published MIRD values are to three decimal places and some rounding errors will have been introduced in the presented figure. The Python programming language however uses the 64-bit IEEE 754 number standard to represent floating type numbers, this gives the *track.py* values higher precision (52 bits of space for the

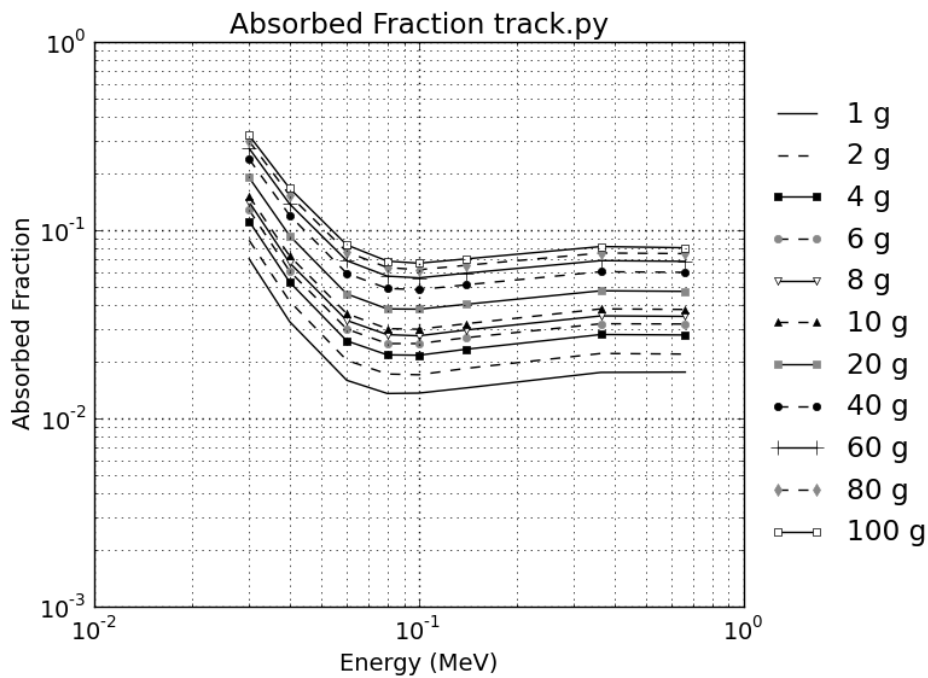


(a) Absorbed fractions from the MIRD pamphlet as a function of mass

(b) Absorbed fractions from *track.py* as a function of mass**Figure 4.5:** Comparison of Absorbed Fractions as a function of mass between the MIRD pamphlets and a simple python based Monte Carlo code.



(a) Absorbed fractions from the MIRD pamphlet as a function of energy

(b) Absorbed fractions from *track.py* as a function of energy**Figure 4.6:** Comparison of Absorbed Fractions as a function of energy between the MIRD pamphlets and a simple python based Monte Carlo code.

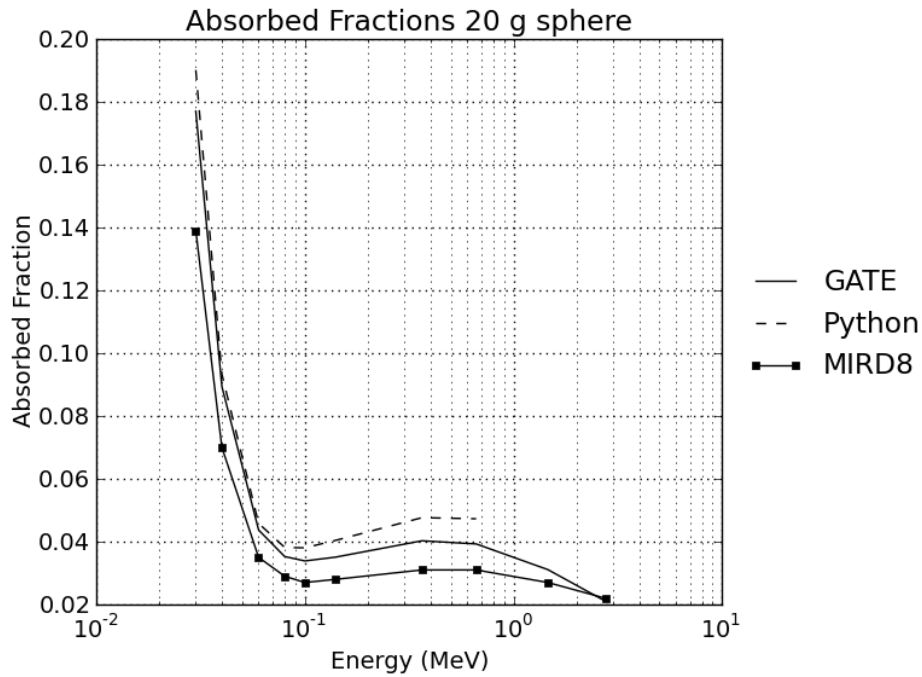
mantissa, or around 16 decimal digits) and therefore the small rounding errors are not visible on the figures.

Since *track.py* and the MIRD values do not take into account electron transport the following section (section 4.3.1) discuss possible reasons for these differences further.

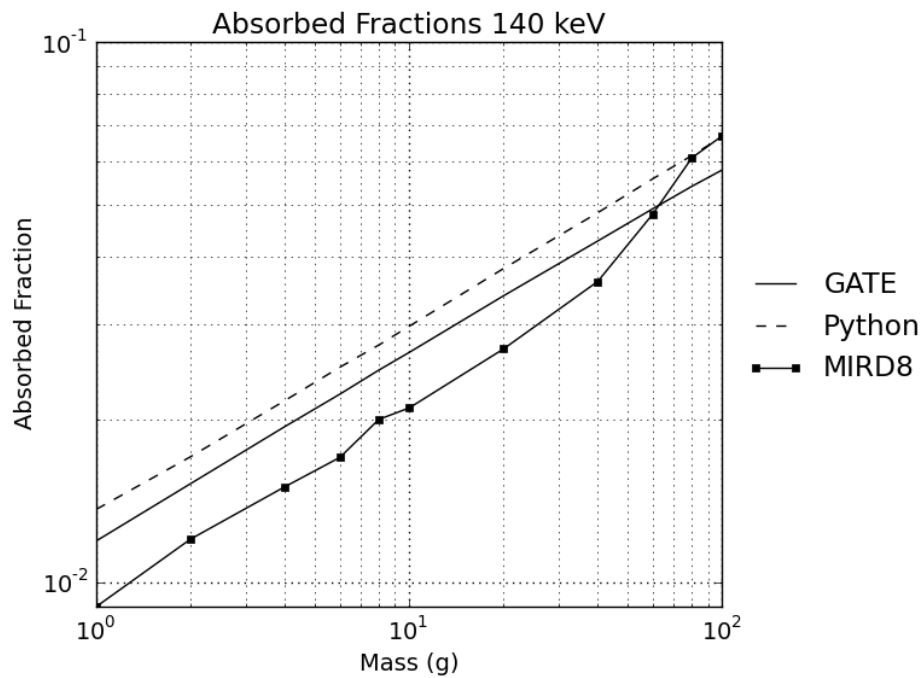
4.3.1 Negating electron transport

Both the MIRD and *track.py* Monte Carlo approaches do not account for the effect of electron transport on the Absorbed Fractions. To gain further information on the accuracy of the MIRD values figure 4.7 compares MIRD8, *track.py* and GATEv3.1.2. When comparing the three approaches it is encouraging to see that results simulated in GATE can be reasonably predicted by the recalculated *track.py* approach especially in the low energy region. Where this trend is not observed for the MIRD8 values.

Looking more closely, figure 4.7a shows that as the photon energy increases, the absorbed fractions for the MIRD8 and python based approaches seem to diverge from the trend exhibited in GATE. The most likely explanation for this is the explicit treatment of electron transport in GATE. It is reasonable to assume that as the photon energy increases some of the kinetic energy transferred through Compton scattering is not being absorbed in the region of interest. For example in GATE, electrons are tracked through a path of continuous discrete energy loss. This differs from the MIRD8 calculations which assumes that the kinetic energy of secondary electrons (i.e. recoil electrons produced by Compton effect) are absorbed into the medium at the point of interaction. If the electron escapes the region without depositing its kinetic energy the MIRD8 calculation will vary slightly and should over estimate the absorbed fraction (i.e. kerma approximation). This is indeed true for the *track.py* calculations however this is not seen in the MIRD8 values. In fact the MIRD8 values underestimate the absorbed fraction for spheres with a mass less



(a) Absorbed fractions for a 20 g unit density sphere with varying photon energies.



(b) Absorbed fractions for 140 keV photons in unit density spheres.

Figure 4.7: Comparison of Absorbed Fractions between the MIRD pamphlet 8, a simple python based Monte Carlo code and GATE

then 80 g. There is no plausible explanation for this underestimation except that the actual Monte Carlo code itself introduced this bias.

Higher energy secondary electrons will also have some probability of producing bremsstrahlung, which may also escape the region without being re-absorbed. It should however be noted that the probability of this is extremely low. This is because recoil electrons produced from Compton interactions with an initial photon energy of less than 2 MeV will have a very low radiation yield, where the radiation yield is the fraction of initial kinetic energy emitted as bremsstrahlung through continuous energy loss of a charged particle in a medium [141]. Figure 4.8 was produced from the ESTAR database [142] and shows the radiation yield for electrons in the MIRD - soft tissue composition. It can be seen from figure 4.8, that electrons with a kinetic energy of approximately 0.2 MeV results in a radiation yield of 0.1%, therefore by neglecting this process less than 0.1% of the absorbed dose is not being accounted for.

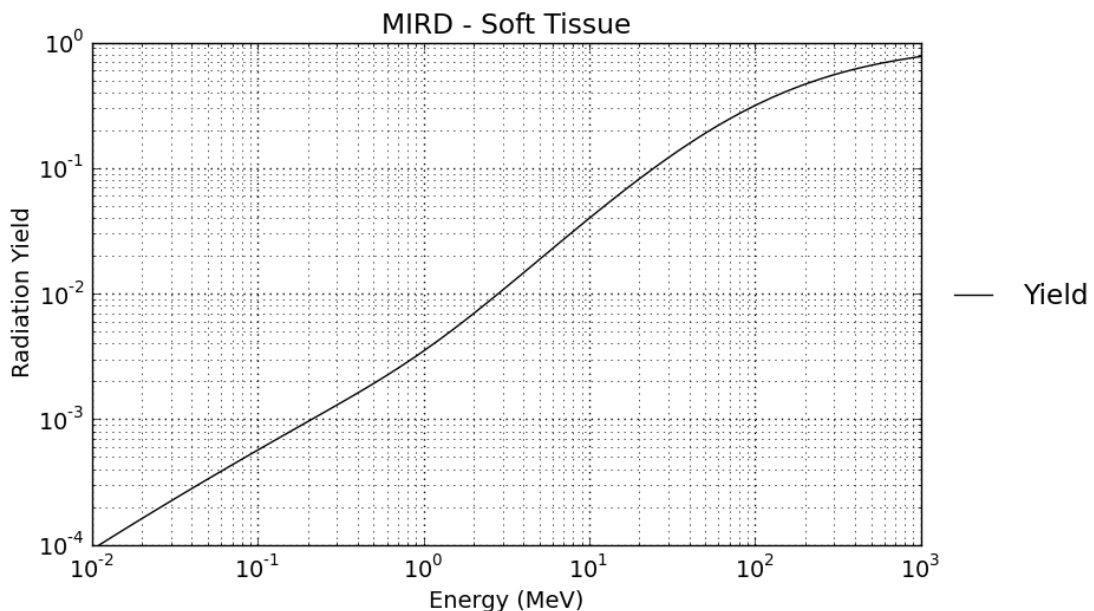


Figure 4.8: Radiation yield for electrons in the MIRD - soft tissue composition.

It has also been confirmed (see figure 4.7b) that the linear trend (note the log-log graph) seen in the python based approach is consistent with the trend seen in the

GATE results. Where sphere size increases this trend is not observed for the MIRDS values.

4.4 Comparison of GATE to the Gold Standard

From the results presented in figures 4.2 to 4.4 no judgment on the accuracy of GATE can be given without comparison to the current “gold standard”. As stated in section 2.3 this thesis uses the re-evaluation of absorbed fractions of photons in various sphere sizes as completed by Stabin and Konijnenberg (reference values) [1] as its gold standard for absorbed fractions.

Table B.1 includes the reference values calculated by Stabin and Konijnenberg which are the average values from using the Monte Carlo codes EGS4 and MCNP4B. For a more accurate comparison all values have been normalised to our gold standard (i.e. GATE simulation value divided by the reference value from Stabin). As a comparison figures 4.9 through 4.11 shows the normalised values for different photon energies as a function of sphere mass. Photon energies of 0.040 MeV, 0.140 MeV and 0.662 MeV have been shown. Table B.2 presents the full range of normalised values to two decimal places. It also shows values for EGS4 divided by the MCNP values from Stabin and Konijnenberg [1].

From figures 4.9 through 4.11 it can be seen that a basic trend in all of the GATE simulation approaches are very similar. As the photon energy is reduced the differences between the *standard* physics packages used in version 3 and 6 become more noticeable compared to the *low energy* and *PENELOPE* packages. Overall from table B.2 it can be seen that absorbed fraction simulated in GATE do not differ from the reference values by more than 12% for the *standard* packages and 10% for the *low energy* and *PENELOPE* packages. It is however also appropriate to recognise that the differences in the EGS4 and MCNP values are as high as 13%. These differences are therefore more likely to represent commonly encountered

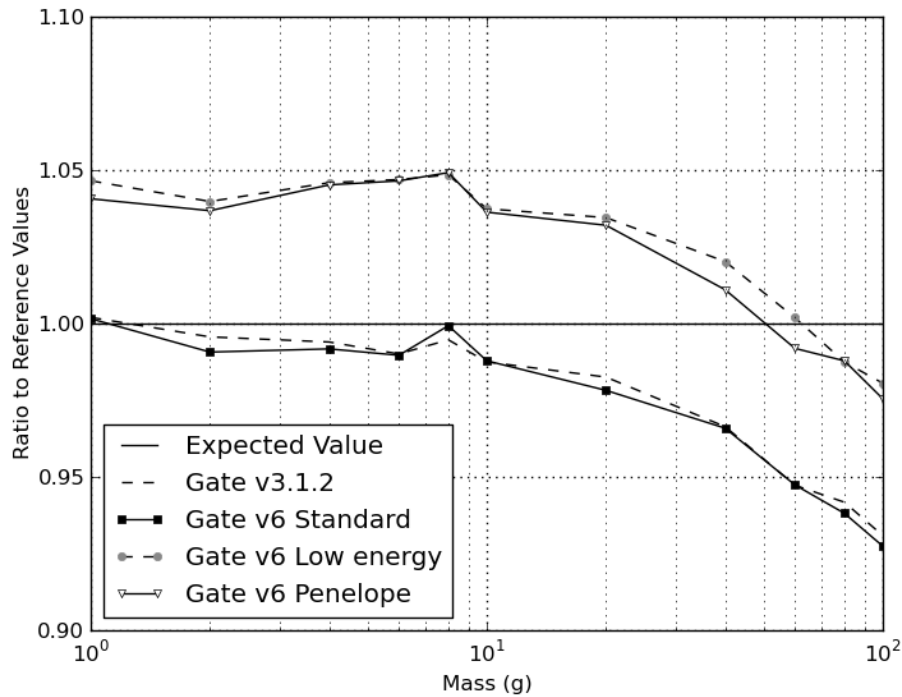


Figure 4.9: Normalised absorbed fractions for 0.040 MeV photons against the gold standard.

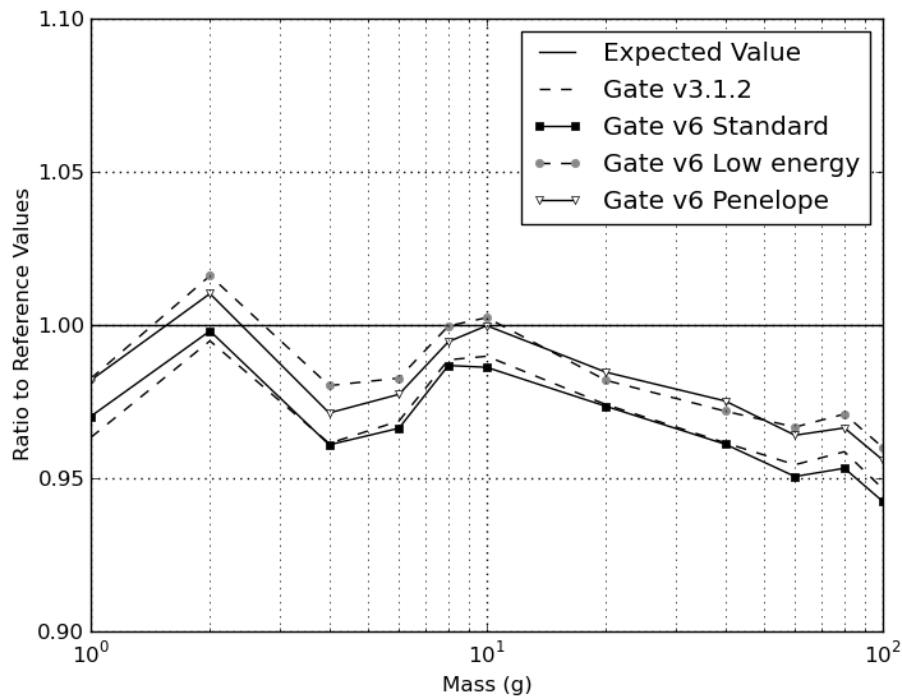


Figure 4.10: Normalised absorbed fractions for 0.140 MeV photons against the gold standard.

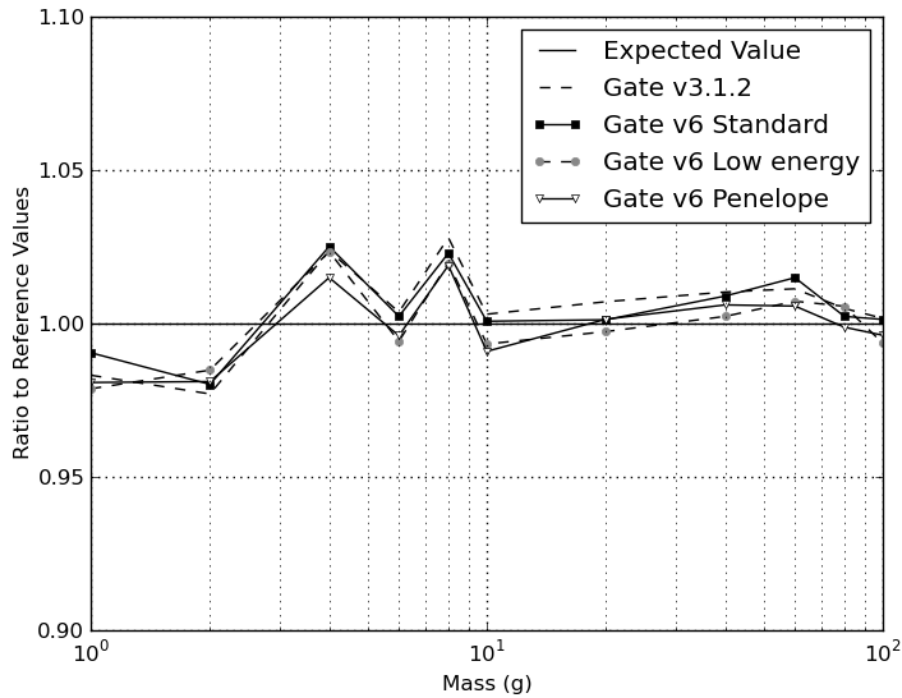


Figure 4.11: Normalised absorbed fractions for 0.662 MeV photons against the gold standard.

differences in the modeling software itself.

One question however still remains, is there sufficient evidence to suggest which of the GATE physics packages are the most suitable for dosimetry applications in an energy range of 0.03 MeV to 2.75 MeV? Hypothesis testing of the four GATE methods (GATE v3.1.2, GATE v6 *standard*, GATE v6 *low energy* and GATE v6 *PENELOPE*) was performed by comparing the ratio of each method to the reference values by Stabin and Konijnenberg (see table B.2). It should be noted that if the GATE method is comparable to the reference values then the ratio of the absorbed fractions will equal 1.00, therefore this statistical test will assume a hypothesis that $\mu_0 = 1$ (i.e. null hypothesis, $H_0 : \mu_0 = 1$ and the alternative hypothesis, $H_a : \mu_0 \neq 1$).

For each of the four methods compared to the values obtained by Stabin a total of $n = 110$ different combinations of photon energy and sphere masses are simulated.

As the sample size is suitably large the Z-score¹ is calculated for each method and compared to a rejection region based on a 99% confidence interval.

From table 4.2 it can be concluded that both the *low energy* or *PENELOPE* libraries are comparable to the other Monte Carlo codes used by Stabin and Konijnenberg, whereas there is a noticeable difference between GATE version 3 and the *standard* package compared to the reference values. Due to the similarity between GATE version 3 and the *standard* physics library it is not necessary to investigate GATE version 3 any further. The remainder of this thesis will therefore only use GATE version 6. The physics libraries will again be compared in chapter 5 with respect to voxelised sources and phantoms.

Table 4.2: Hypothesis Testing of the GATE physics libraries

	GATE v3	GATE v6 <i>standard</i>	GATE v6 <i>low energy</i>	GATE v6 <i>PENE- LOPE</i>
μ_0	1.00	1.00	1.00	1.00
α	0.01	0.01	0.01	0.01
\bar{X}	0.984	0.981	0.999	1.001
$\sigma_{\bar{X}}$	0.030	0.030	0.034	0.035
n	110	110	110	110
Z-score	-5.52	-6.58	-0.33	0.20
Rejection region ^a	2.58	2.58	2.58	2.58

^a Two tail rejection region i.e. if $|Z| > \text{rejection region}$, then rejected the null hypothesis

4.5 Chapter Summary

The use of the MIRD spheres as a benchmark for Monte Carlo transport codes has been discussed in this chapter. The limitations of the original MIRD spheres have been discussed and the GATE package was compared to the alternative gold standard presented by Stabin and Konijnenberg. By using the MIRD spheres as

¹As the sample size is large (i.e. >30) the assumption is made that the deviation from $\mu = 1.00$ in the normalised values is normally distributed with the true standard deviation being approximated by the sample standard deviation.

a benchmark, evidence has been provided to suggest that for simple geometric phantoms GATE provides an appropriate level of accuracy. It is also concluded that GATE version 6 will be adopted for further dosimetry simulations since the GATE version 3 and GATE version 6 *standard* packages are comparable. The accuracy and use of voxelised phantoms in GATE will be addressed in chapter 5.

Chapter 5

Voxelised phantom validation

5.1 Introduction

It was stated in section 2.5 that voxelised phantoms are more useful for defining realistic human anatomy compared to traditional mathematical phantoms. The validation results of the previous chapter only addressed sources and phantoms defined using simple geometric shapes, it is therefore important to investigate the accuracy of voxelised phantoms and in particular the effect of individual voxel size. Inaccurate or insufficient voxel sampling of regions may introduce errors into calculations of the absorbed fraction or specific absorbed fractions.

To extend on the work completed in the previous chapter the MIRD spheres are again simulated in GATE, however the spheres will be defined as a voxelised phantom and source. The computational issues associated with simulating increasingly smaller voxel sizes are also investigated through a speed benchmark. From this data a choice as to which of the physics packages is the most appropriate and what spatial sampling for the simulation of voxelised phantoms will be made. Another important extension from the previous chapter is the investigation of source to target regions. The absorbed dose in a neighbouring organ from a source organ makes an important contribution to the overall internal dosimetry assessment. The performance of

voxelised phantoms will therefore be investigated for source to target regions in both homogeneous and heterogeneous media.

5.2 Absorbed Fractions

Using values from table B.1 the absorbed fractions are again normalised to the reference values by Stabin and Konijnenberg [1].

Figures 5.1 through 5.3 show the normalised absorbed fractions for 140 keV photons and different sphere masses. It can be seen that there are substantial differences for large voxel sizes and that as the voxel size decreases below 1 mm (*standard*) and <2 mm (*low energy, PENELOPE*) the simulated absorbed fractions do not differ from the reference values by more than 5%. It can also be seen that for each of the physics packages the overall trend of each plot is similar. This highlights the importance of correctly setting the voxel size for accurate absorbed dose calculations. By referring back to figure 3.1 the 60 g sphere represented by 6.0, 4.0 and 2.0 mm voxels have masses of 55.51, 61.95 and 59.98 g respectively. This is also reflected in figures 5.1 through 5.3 where it can be seen that for a voxel size of less than 2 mm the absorbed fraction begins to converge. Table 5.1 shows the absorbed fractions for 140 keV photons using a voxel size of 0.25 mm.

5.2.1 Speed benchmark

A speed benchmark for the 100 g sphere and 140 keV photons is shown in table 5.2. A total of 10^6 photons were generated in each run for a voxel size of 0.25 mm. It can be seen from the mean and standard deviation that the *standard* physics package is much quicker than both the *low energy* and *PENELOPE* packages. From the results previously presented in table 4.1 this result is expected, however the *low energy* package is faster for voxel phantoms than the *PENELOPE* packages.

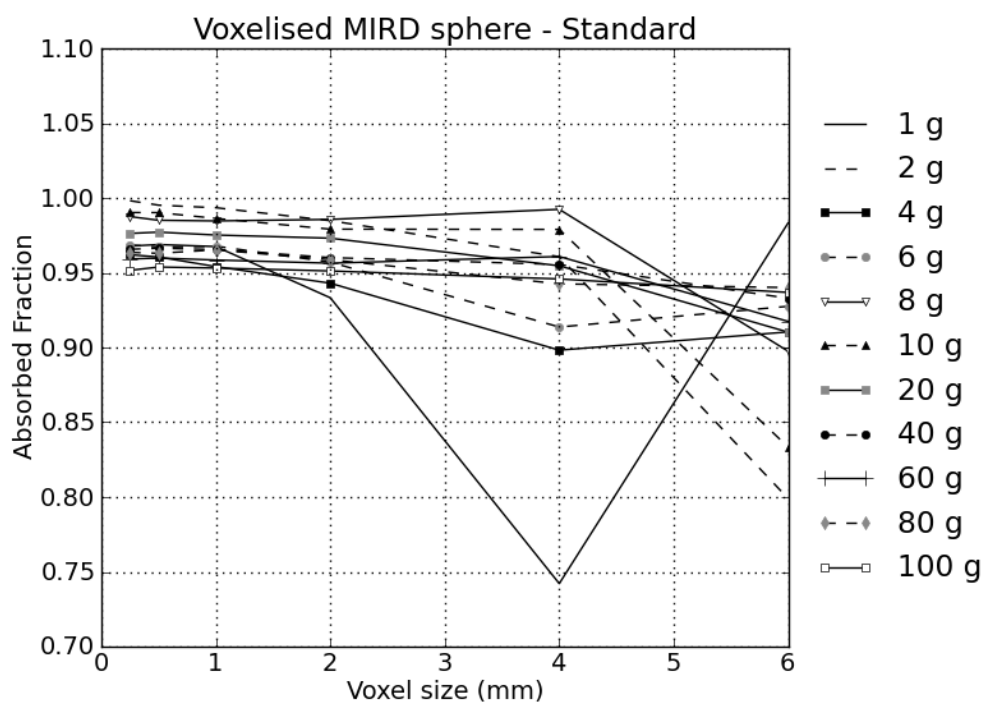


Figure 5.1: Normalised absorbed fractions for 140 keV photons in voxelised sphere phantoms with different masses, using the *standard* physics package.

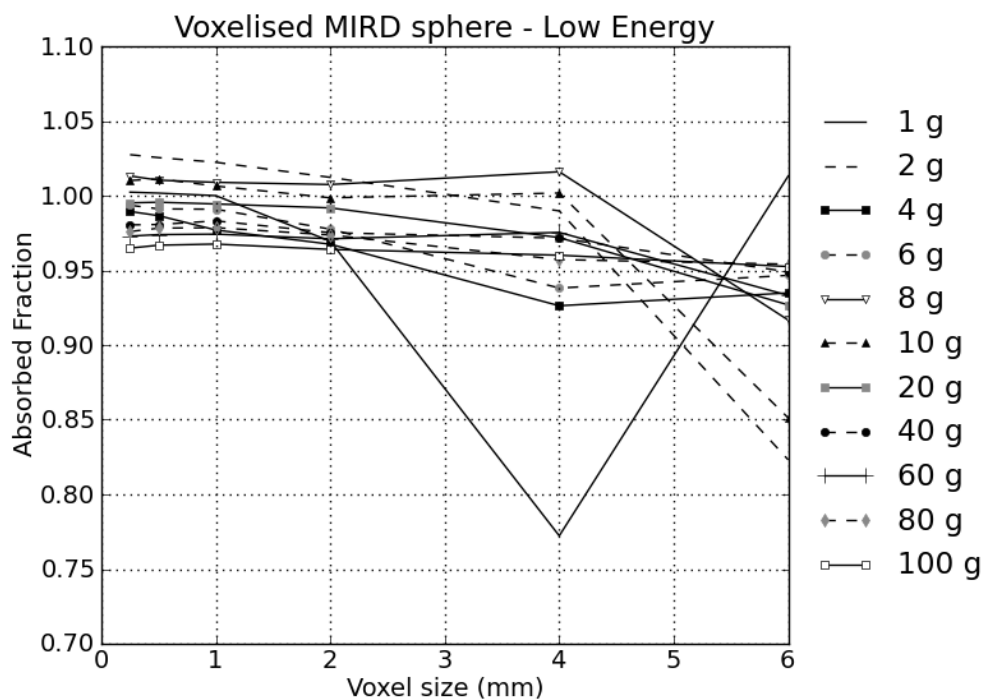


Figure 5.2: Normalised absorbed fractions for 140 keV photons in voxelised sphere phantoms with different masses, using the *low energy* physics package.

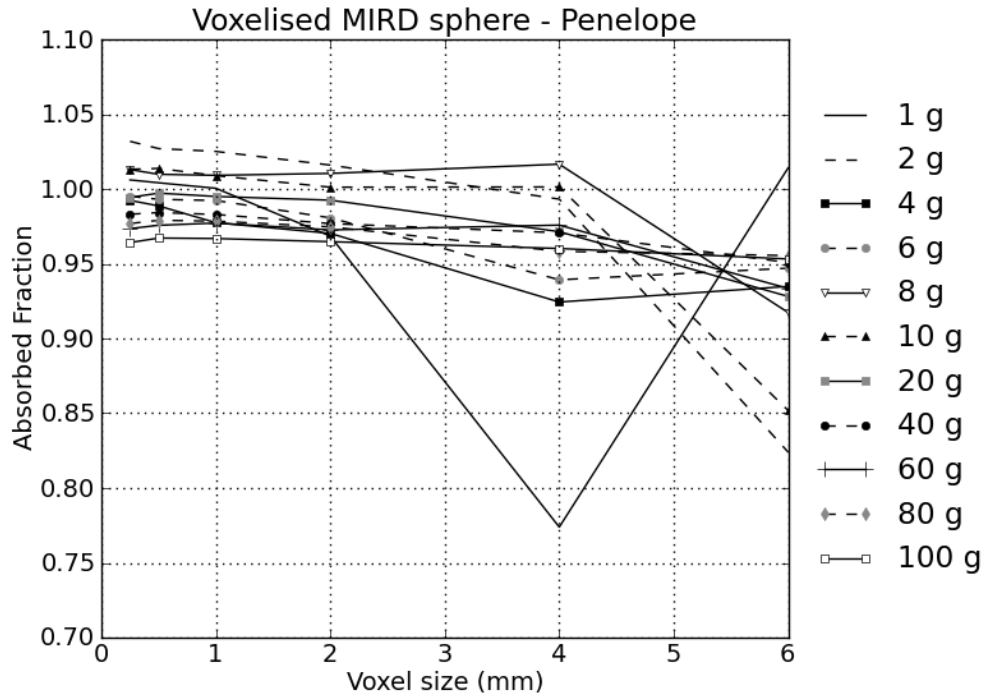


Figure 5.3: Normalised absorbed fractions for 140 keV photons in voxelised sphere phantoms with different masses, using the *PENELOPE* physics package.

5.2.2 Choice of physics packages

Normalising the values in table 5.1 to the reference values for the 140 keV photons, the three physics packages can be compared. Table 5.3 shows the ratio of the GATE values to the reference values. This suggests that by choosing a suitably small voxel size the absorbed fractions are suitably approximated.

Using the values in table 5.3, a small sample hypothesis test¹ is used to compare the absorbed fractions for the different physics packages. The null hypothesis, H_0 is that the expected mean $\mu_0 = 1$ and the alternative hypothesis, H_a is $\mu_0 \neq 1$. For a 95% confidence interval the null hypothesis is rejected for the *standard* library in favor of the alternative hypothesis. For the *low energy* and *PENELOPE* physics libraries the null hypothesis can not be rejected. Therefore as with section 4.4 the

¹Since the sample size is small i.e. $n=11$, deviation from $\mu = 1.00$ is assumed to follow the t distribution.

Table 5.1: The absorbed fractions in the MIRD spheres for 140 keV photons. Values are presented to four decimal places for each of the different physics packages using voxelised phantoms.

Mass (g)	<i>standard</i>	<i>low energy</i>	<i>PENELOPE</i>
1	0.0126	0.0130	0.0131
2	0.0160	0.0164	0.0165
4	0.0202	0.0208	0.0208
6	0.0232	0.0238	0.0239
8	0.0257	0.0263	0.0263
10	0.0277	0.0283	0.0284
20	0.0351	0.0358	0.0358
40	0.0444	0.0451	0.0452
60	0.0508	0.0516	0.0516
80	0.0559	0.0566	0.0567
100	0.0600	0.0608	0.0607

low energy and *PENELOPE* libraries are suitably comparable to the reference values. Therefore a decision on the most suitable package to use will either be the *low energy* or *PENELOPE* package and will depend on the speed of the simulation.

By comparing table 4.1 for the geometric phantom against table 5.2 of the voxelised phantom, it can be seen that the *standard* physics package is the fastest and the *low energy* and *PENELOPE* speed is dependent on the type of phantom being used. It can be seen that by using the geometric phantom the simulation speed is significantly faster than when using a voxelised phantom. A large portion of the simulation time is spent calculating and updating paths of particles in voxelised phantoms [143]. This is a reflection of the differences in between the calculations using the *low energy* and *PENELOPE* libraries.

As voxelised phantoms are the preferred method for creating phantoms of patient anatomy it is considered that the *low energy* physics package is the more useful library for any future applications in this thesis.

Table 5.2: Speed benchmarking of a voxelised phantom for GATE version 6 physics packages with a voxel size of 0.25 mm (Time in seconds)

Run no.	<i>standard</i> (s)	<i>low energy</i> (s)	<i>PENELOPE</i> (s)
1.0	149.2	214.1	225.9
2.0	149.6	217.3	226.0
3.0	151.2	215.7	225.1
4.0	149.8	215.8	226.2
5.0	149.9	215.5	224.8
6.0	150.4	214.4	226.2
7.0	151.2	216.0	225.1
8.0	149.0	215.8	225.7
9.0	150.2	214.9	226.9
10.0	149.6	214.6	224.4
mean	150.0	215.4	225.6
standard deviation	0.8	0.9	0.8

Table 5.3: The t-statistic is used for hypothesis testing of the GATE physics libraries using voxelised sources.

Mass (g)	GATE v6 <i>standard</i>	GATE v6 <i>low energy</i>	GATE v6 <i>PENE- LOPE</i>
1	0.968	1.002	1.006
2	0.998	1.027	1.032
4	0.962	0.989	0.992
6	0.969	0.994	0.995
8	0.988	1.013	1.013
10	0.990	1.010	1.013
20	0.976	0.995	0.994
40	0.966	0.980	0.983
60	0.959	0.973	0.973
80	0.964	0.976	0.977
100	0.952	0.965	0.964
μ_0	1.000	1.000	1.000
α	0.05	0.05	0.05
\bar{X}	0.972	0.993	0.995
$S_{\bar{X}}$	0.014	0.019	0.020
n	11	11	11
T-score	-6.44	-1.18	-0.86
Rejection region ^a	2.63	2.63	2.63

^a Two tail rejection region i.e. if $|t| > \text{rejection region}$, then reject the null hypothesis

5.3 Source to Target

In all of the dosimetric studies discussed so far the source and target region have been the same region. This is adequate for determining the self absorption of organs or tissue that contain radioactivity, however in the majority of cases the absorbed dose resulting from radioactivity in one organ to a target organ is required. This section investigates that situation for very simple homogeneous and heterogeneous phantoms.

5.3.1 Homogeneous voxelised simulation

The absorbed fractions calculated with different voxel sizes are summarised for a homogeneous medium in table 5.4. The values are also normalised to the geometric simulations for both 140 keV and 511 keV energy photons. The geometric simulation value is equivalent to a voxel size of zero. It can be seen that as the voxel size is smaller than 2 mm the absorbed fraction is within 10% agreement with the geometric phantom.

Table 5.4: Absorbed Fractions for a simple source to target region in a homogeneous medium for 140 and 511 keV photons.

Voxel size (mm)	Absorbed	Absorbed	Voxel /	Voxel /
	Fraction 140 keV	Fraction 511 keV	Geometric 140 keV	Geometric 511 keV
8	7.69E-05	7.89E-05	0.120	0.120
4	2.58E-04	2.67E-04	0.404	0.407
2	5.88E-04	6.11E-04	0.921	0.928
1	6.27E-04	6.51E-04	0.982	0.989
0.5	6.33E-04	6.57E-04	0.992	0.999
0.25	6.32E-04	6.58E-04	0.990	1.000
Geometric	6.39E-04	6.58E-04	1.000	1.000

To calculate the mean absorbed dose per unit of cumulated activity (DF) both the region mass and the mean energy emitted per decay (Δ) is required. For a source

emitting only 140 keV photons $\Delta = 2.24 \times 10^{14}$ J, where for a source emitting only 511 keV photons $\Delta = 8.19 \times 10^{14}$ J. For each of the voxelised phantoms the sphere mass is calculated on a 'voxel-wise' basis i.e. each individual voxel that makes up the region has a known volume and a known density. The calculated DFs are shown in table 5.5, also shown is the calculated sphere mass and the voxel DFs divided by the geometric DF.

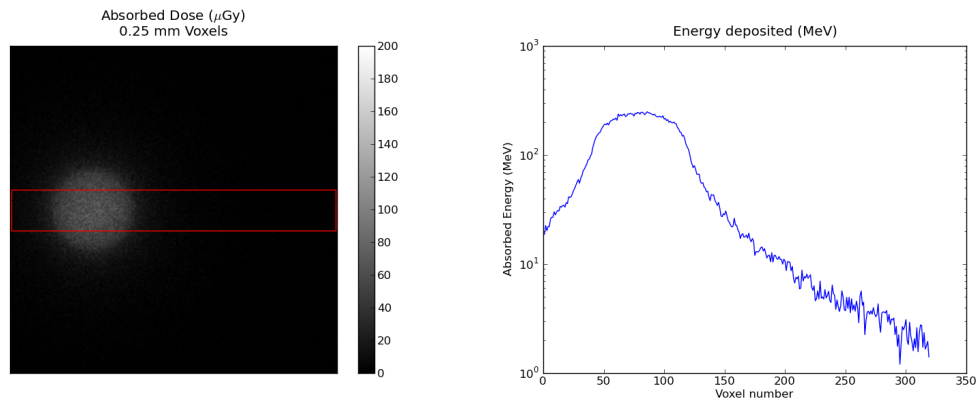
Table 5.5: DFs for a simple source to target region in a homogeneous medium for 140 and 511 keV photons.

Voxel size (mm)	Mass (g)	DF ($\frac{Gy}{Bq \cdot sec}$) 140 Kev	DF ($\frac{Gy}{Bq \cdot sec}$) 511 Kev	Voxel / Geometric 140 keV	Voxel / Geometric 511 keV
8	0.51	3.37E-15	1.26E-14	0.984	0.981
4	1.73	3.35E-15	1.27E-14	0.980	0.986
2	3.88	3.40E-15	1.29E-14	0.994	1.002
1	4.14	3.40E-15	1.29E-14	0.994	1.001
0.5	4.17	3.41E-15	1.29E-14	0.996	1.003
0.25	4.18	3.39E-15	1.29E-14	0.991	1.002
Geometric	4.19	3.42E-15	1.29E-14	1.000	1.000

Figure 5.4 shows the advantages of using a voxelised phantom simulation, clearly showing localised areas of increased absorbed dose. An absorbed dose plot of the homogeneous phantom with a voxel size of 0.25 mm from 511 keV photons is shown in figure 5.4a. It can be seen that from a histogram (figure 5.4b) of the energy deposited in each voxel that for a spherical source a hot spot is seen in the centre of the source as a result of self absorption. A typical exponential decay trend is observed in the deposited energy as the voxels are placed further away from the source. This also demonstrates scatter out of the source region.

5.3.2 Heterogeneous voxelised simulation

A heterogeneous voxelised phantom was simulated with two 10 mm thick slabs of lung and fat separating a spherical source (kidney) and target (liver) region each

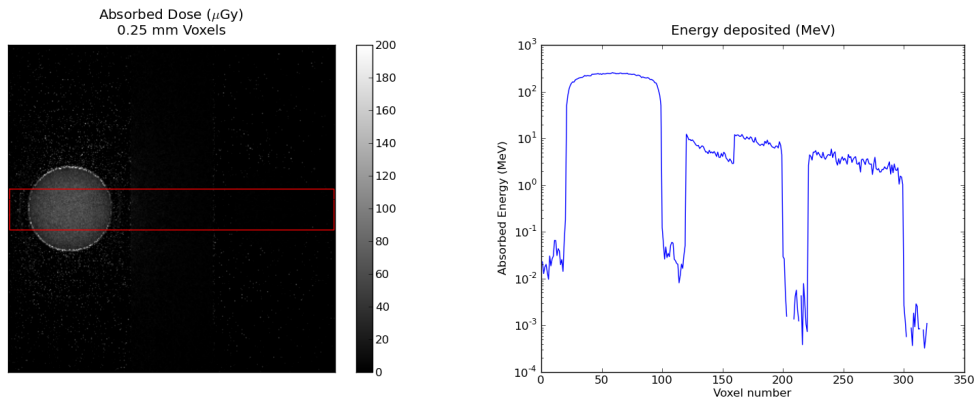


(a) Absorbed dose plot of a homogeneous phantom with a voxel size of 0.25 mm. (b) Deposited energy histogram of values along the centre slice of the phantom.

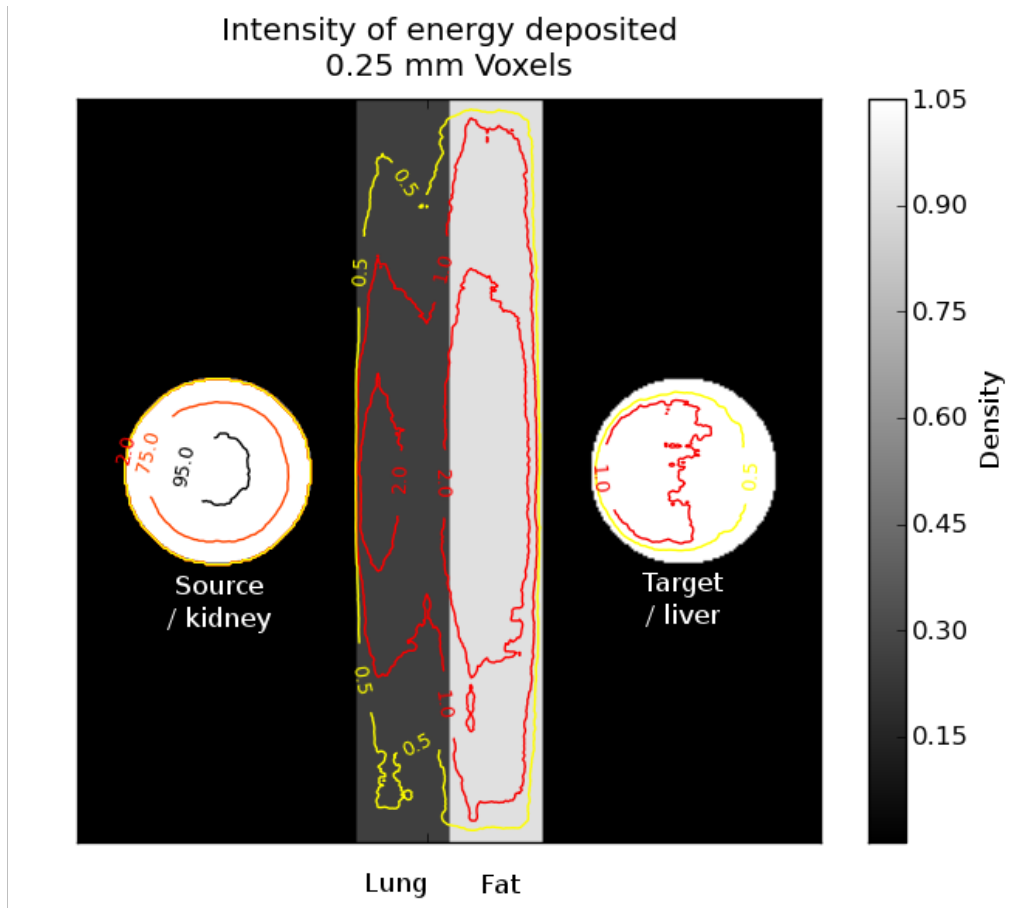
Figure 5.4: Dosimetry plots for a homogeneous phantom with a voxel size of 0.25 mm.

with a radius of 10 mm. This phantom was placed in a world volume with the composition of air. An absorbed dose distribution of the heterogeneous phantom is shown in figure 5.5a. It shows a voxel size of 0.25 mm from 511 keV photons. A histogram of the energy deposited in each voxel is also shown in figure 5.5b. Figure 5.5c shows the density of the phantom overlaid by a contour plot of the intensity of the energy deposited in each voxel. The contour plot is smoothed by a median filter. It can be clearly seen from figures 5.5b and 5.5c that the highest intensity is in the centre of the spherical source. The deposited energy decreases to less than 0.5% of the maximum intensity in the air region. The intensity of energy deposited in the lung and fat regions are below 3% of the maximum. The target region decreases to below 2% of the maximum intensity.

The calculated absorbed fractions for the heterogeneous voxelised phantom are shown in table 5.6. Values are compared to the absorbed fraction calculated with the geometric phantom definition. It is found that for both photon energies the absorbed fraction falls within 10% of the values determined from the geometric phantom for voxel sizes less than 2 mm. Where table 5.7 shows the calculated DFs using the voxel and geometric phantoms. For a voxel size of less than 2 mm the agreement



(a) Absorbed dose plot of a heterogeneous phantom with a voxel size of 0.25 mm. (b) Deposited energy histogram of values along the centre slice of the phantom.



(c) Parentage of maximum energy deposited as a contour plot.

Figure 5.5: Dosimetry plots for a heterogeneous phantom with a voxel size of 0.25 mm.

Table 5.6: Absorbed Fractions for a simple source to target region in a heterogeneous medium for 140 and 511 keV photons.

Voxel size (mm)	Absorbed Fraction 140 keV	Absorbed Fraction 511 keV	Voxel / Geometric 140 keV	Voxel / Geometric 511 keV
8	3.31E-05	4.09E-05	0.094	0.096
4	1.33E-04	1.62E-04	0.378	0.381
2	3.22E-04	3.92E-04	0.917	0.922
1	3.44E-04	4.17E-04	0.978	0.982
0.5	3.48E-04	4.23E-04	0.990	0.995
0.25	3.50E-04	4.23E-04	0.996	0.996
Geometric	3.51E-04	4.25E-04	1.000	1.000

Table 5.7: DFs for a simple source to target region in a heterogeneous medium for 140 and 511 keV photons.

Voxel size (mm)	Mass (g)	DF ($\frac{Gy}{Bq\cdot sec}$) 140 Kev	DF ($\frac{Gy}{Bq\cdot sec}$) 511 Kev	Voxel / Geometric 140 keV	Voxel / Geometric 511 keV
8	0.54	1.37E-15	6.17E-15	0.772	0.788
4	1.83	1.62E-15	7.23E-15	0.915	0.923
2	4.11	1.76E-15	7.80E-15	0.990	0.996
1	4.39	1.76E-15	7.78E-15	0.990	0.994
0.5	4.42	1.76E-15	7.82E-15	0.995	0.999
0.25	4.43	1.77E-15	7.81E-15	0.997	0.998
Geometric	4.44	1.77E-15	7.83E-15	1.000	1.000

between the geometric and voxel phantoms is to within 1%.

5.4 Using Voxelised Phantoms

Overall there is agreement in the absorbed fractions calculated with voxelised phantoms compared to geometric phantoms. In both the homogeneous and heterogeneous cases the voxelised phantom method gave an agreement to within 10% of the geometric value for a voxel size of 2 mm or less. This result suggests that the use of voxelised phantoms in GATE can be highly accurate, provided that the voxelised

phantom is a reasonable representation of the true geometry being simulated. For voxelised phantoms with a voxel size of 2 mm or less, there is very good agreement with the reference values in the MIRD spheres for the three physics libraries used. This agreement is to within 5%.

5.4.1 Absorbed fraction compared to the DF

When the DF's are calculated, the difference between the Voxel and Geometric results give improved agreement for all voxel sizes compared to calculating the absorbed fractions. The reason for this is explained by recapping how $DF(k \leftarrow h)$ is calculated.

$$DF(k \leftarrow h) = \sum_i \Delta_i \frac{\phi_i(k \leftarrow h)}{m_k} \quad (5.1)$$

In equation 5.1 the absorbed fraction is scaled to the mass of the target region and therefore compensates for inaccuracies in the absorbed fraction. When only the voxel size is varied Δ_i is effectively a constant and therefore only the absorbed fraction and target region mass will have any effect on the DF. It should also be noted that the probability that energy is deposited in the target region is dependent on the region's geometry, therefore if the choice in voxel size affects both the target mass and geometry then the absorbed fraction will also be affected. In other words for larger voxels the geometric approximation of the target region is inadequate and results in significantly smaller target mass than reality. This leads to an underestimation of the absorbed fraction. The dose fraction is less affected because it is the energy deposited per unit mass of the modeled target region and the model mass matches its volume.

This is best demonstrated in comparing tables 5.6 and 5.7. For example table 5.6 shows that for a voxel size of 4 mm and 511 keV photons the simulated absorbed fraction was 62% less than the geometric case. Where table 5.7 shows that the under sampled voxelised sphere had a mass of 1.83 g compared to the geometric sphere

mass of 4.44 g (an underestimation of 59%), however when the DF is calculated only a 8% difference is seen between the geometric sphere and the sphere defined by 4 mm voxels.

From tables 5.5 and 5.7 a voxel size of 2 mm or less provides an error of less than 1% compared to the geometric case. From the results the evidence suggests that accurate calculation of the absorbed fractions requires a voxel size of 2 mm or less to achieve convergence. It is therefore considered that as a rule of thumb a voxel size of 2 mm or less provides convergence for calculating DFs. Further investigation on the effect of voxel size is presented in chapter 6.

5.5 Chapter Summary

The use of voxelised phantoms in GATE has been investigated in this chapter. By simulating the MIRD spheres as a voxelised phantom it has been decided that the *low energy* physics package is the most useful of the three packages for further dosimetry simulations in this thesis. This decision takes into account the overall accuracy and simulation speed of very simple voxelised sources and phantoms.

It was also found that calculating the DFs provides a higher level of accuracy than calculating the absorbed fraction in voxelised phantoms. Initial evidence has also been presented to suggest that a voxel size of 2 mm or less provides acceptable volume sampling. This chapter has therefore validated the accuracy of voxelised phantoms in GATE.

Chapter 6

Kidney to Liver Dose Factor

6.1 Introduction

It was recognised in the literature review that the absorbed fraction and organ mass contribute a high uncertainty in an internal dose calculation of patients and that now absorbed fractions are almost exclusively calculated using Monte Carlo approaches. Particular attention has been paid to the accuracy of GATE for calculating absorbed fractions, in chapters 4 and 5. This chapter will make use of GATE in a potentially more clinically relevant situation, using both a standardised model of human anatomy and true patient data. The chapter will calculate organ DFs in the XCAT phantom and a retrospective calculation from patient PET/CT data. Both uniformly and non-uniformly distributed activity in the kidneys will be used to calculate the kidney to kidney DF and kidney to liver DF. As the XCAT phantom is easily scalable, three phantoms with different body mass indexes will also be investigated.

6.2 XCAT Phantom

The resulting dose histogram from the simulation of a number of different XCAT phantom sizes is analysed using the method described in section 3.10. For uniformly

distributed activity in the kidneys the DF for self absorption are summarised in table 6.1. It can be seen that as the phantom mass is increased so does the absorbed fraction, where the kidney to kidney DF decreases as the phantom mass increases. A steady increase in the DF is also seen as the voxel size decreases.

Table 6.2 summarises the absorbed dose in the liver from F-18 uniformly distributed throughout the kidneys for the XCAT phantom. Again as the phantom mass increases the DF decreases and the absorbed fraction increases. The voxel size affects the DF differently for the kidney to liver situation compared to the kidney to kidney situation. A steady decrease in the DF is seen as the voxel size decreases.

6.2.1 Distribution of energy

Iso contours of the deposited energy in the Large XCAT phantom are shown in figure 6.1. The intensity of the deposited energy is shown as a percentage of the maximum energy deposited.

The distribution of the deposited energy from uniform activity inside the kidneys of the XCAT phantom propagates radially from its maximum intensity. The intensity drops sharply at the kidney wall, where the activity is contained. An inverse square propagation can also be seen throughout the liver as the overall intensity drops from 5% to 0.5% of the maximum. The 0.5% contour line maps almost directly around the border of the heart and lung regions. Due to the low density of the Lung regions very little energy is deposited.

6.3 Patient

Using the phantom preparation method described in section 3.9 the kidney to kidney DF is $1.55 \times 10^{-13} \text{ Gy}\cdot\text{Bq}^{-1}\cdot\text{s}^{-1}$, where the kidney to liver DF is $2.43 \times 10^{-15} \text{ Gy}\cdot\text{Bq}^{-1}\cdot\text{s}^{-1}$.

Table 6.1: Kidney DFs of the XCAT phantom of different masses for F-18 distributed uniformly in the kidneys.^a

Voxel Size (mm)	kidney Mass (kg)	ϕ	Φ (kg ⁻¹)	DF (Gy·Bq ⁻¹ ·s ⁻¹)
DF(<i>kidney</i> ← <i>kidney</i>), Small Phantom (51 kg)				
16	0.116	0.07	0.62	1.23E-13
8	0.158	0.14	0.88	1.73E-13
4	0.175	0.19	1.07	2.11E-13
2	0.182	0.22	1.20	2.36E-13
1	0.185	0.24	1.27	2.51E-13
0.6	0.186	0.24	1.30	2.56E-13
0.4	0.187	0.25	1.32	2.61E-13
DF(<i>kidney</i> ← <i>kidney</i>), Average Phantom (69 kg)				
16	0.168	0.09	0.54	1.06E-13
8	0.220	0.15	0.70	1.37E-13
4	0.238	0.20	0.84	1.65E-13
2	0.247	0.23	0.92	1.82E-13
1	0.251	0.24	0.97	1.91E-13
0.6	0.252	0.25	0.99	1.95E-13
0.4	0.253	0.25	1.01	1.98E-13
DF(<i>kidney</i> ← <i>kidney</i>), Large Phantom (95 kg)				
16	0.189	0.09	0.46	9.13E-14
8	0.248	0.16	0.64	1.26E-13
4	0.269	0.20	0.76	1.49E-13
2	0.278	0.23	0.83	1.64E-13
1	0.282	0.25	0.87	1.72E-13
0.6	0.284	0.25	0.89	1.75E-13
0.4	0.285	0.26	0.90	1.78E-13

^aValues are rounded

Table 6.2: Kidney to liver DFs of the XCAT phantom of different masses for F-18 distributed uniformly in the kidneys.^a

Voxel Size (mm)	liver Mass (kg)	ϕ	Φ (kg ⁻¹)	DF (Gy·Bq ⁻¹ ·s ⁻¹)
DF(<i>liver</i> ← <i>kidney</i>), Small Phantom (51 kg)				
16	0.738	0.013	0.018	3.54E-15
8	0.954	0.016	0.017	3.33E-15
4	1.030	0.017	0.016	3.25E-15
2	1.055	0.017	0.016	3.21E-15
1	1.067	0.017	0.016	3.21E-15
DF(<i>liver</i> ← <i>kidney</i>), Average Phantom (69 kg)				
16	1.120	0.017	0.016	3.07E-15
8	1.335	0.019	0.014	2.77E-15
4	1.415	0.020	0.014	2.74E-15
2	1.448	0.020	0.014	2.73E-15
1	1.463	0.020	0.014	2.72E-15
DF(<i>liver</i> ← <i>kidney</i>), Large Phantom (95 kg)				
16	1.281	0.018	0.014	2.78E-15
8	1.515	0.020	0.013	2.56E-15
4	1.599	0.020	0.013	2.53E-15
2	1.636	0.021	0.013	2.51E-15
1	1.653	0.021	0.013	2.51E-15

^aValues are rounded

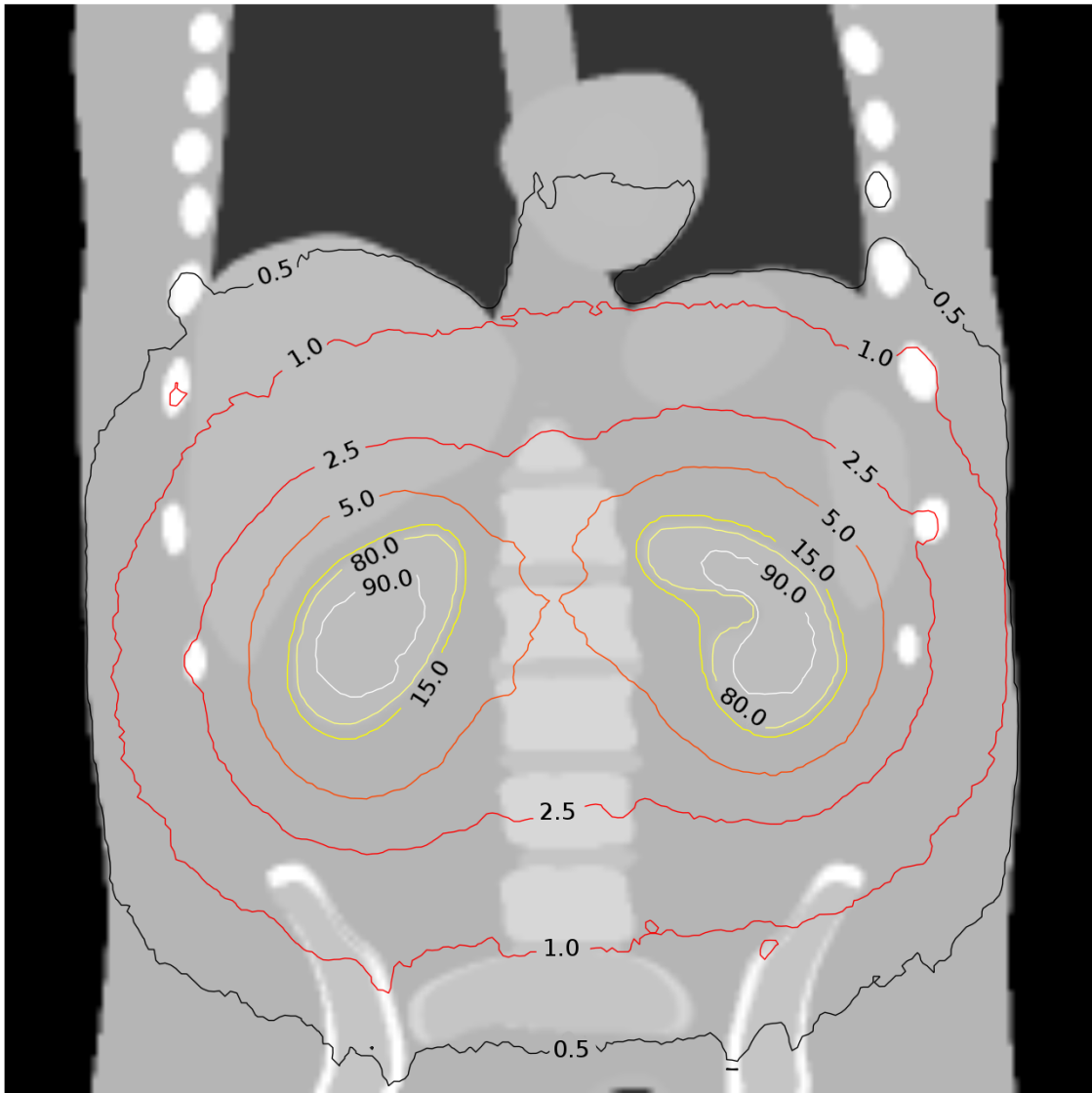


Figure 6.1: Energy distribution of uniform activity in both kidneys of the XCAT phantom (Slice 110, Large).

The absorbed fractions, kidney and liver masses and specific absorbed fractions are also presented in table 6.3.

The absorbed dose on a voxel-wise level is shown for the kidney and liver in figures 6.2 and 6.3 respectively. The dose histogram is fused over the CT image to simplify organ location. The dose histogram is the result of 100 MBq·s cumulated activity with a bio-distribution resulting from ^{18}F -FDG at 70 minutes post injection.

Table 6.3: Kidney and liver DFs from both kidneys of a Average patient administered ^{18}F -FDG.

Organ	Organ Mass (kg)	ϕ	Φ (kg^{-1})	DF ($\text{Gy}\cdot\text{Bq}^{-1}\cdot\text{s}^{-1}$)
kidney	0.264	0.208	0.787	1.55E-13
liver	1.599	0.020	0.012	2.43E-15

6.4 Result Analysis

A number of different variables will affect the accuracy of calculating DFs in voxelised phantoms. Corrections should be applied to ensure that for patient-specific dosimetry the absorbed dose is not underestimated. Voxel volume for the scaled XCAT phantom is used in the following section for estimating the corrections required.

The organ mass is also a key contributor to this correction and the effect of scaling the organ mass of model based phantoms is also discussed. The possible contribution of non-uniform radioactivity will also be highlighted.

6.4.1 Fitting data to different voxel sizes.

It can be seen from table 6.1 that a significantly small voxel size is required to achieve convergence for the organ self dose. Simulating small voxel sizes corrects this spatial sampling issue however this is limited to the computational and memory limitations

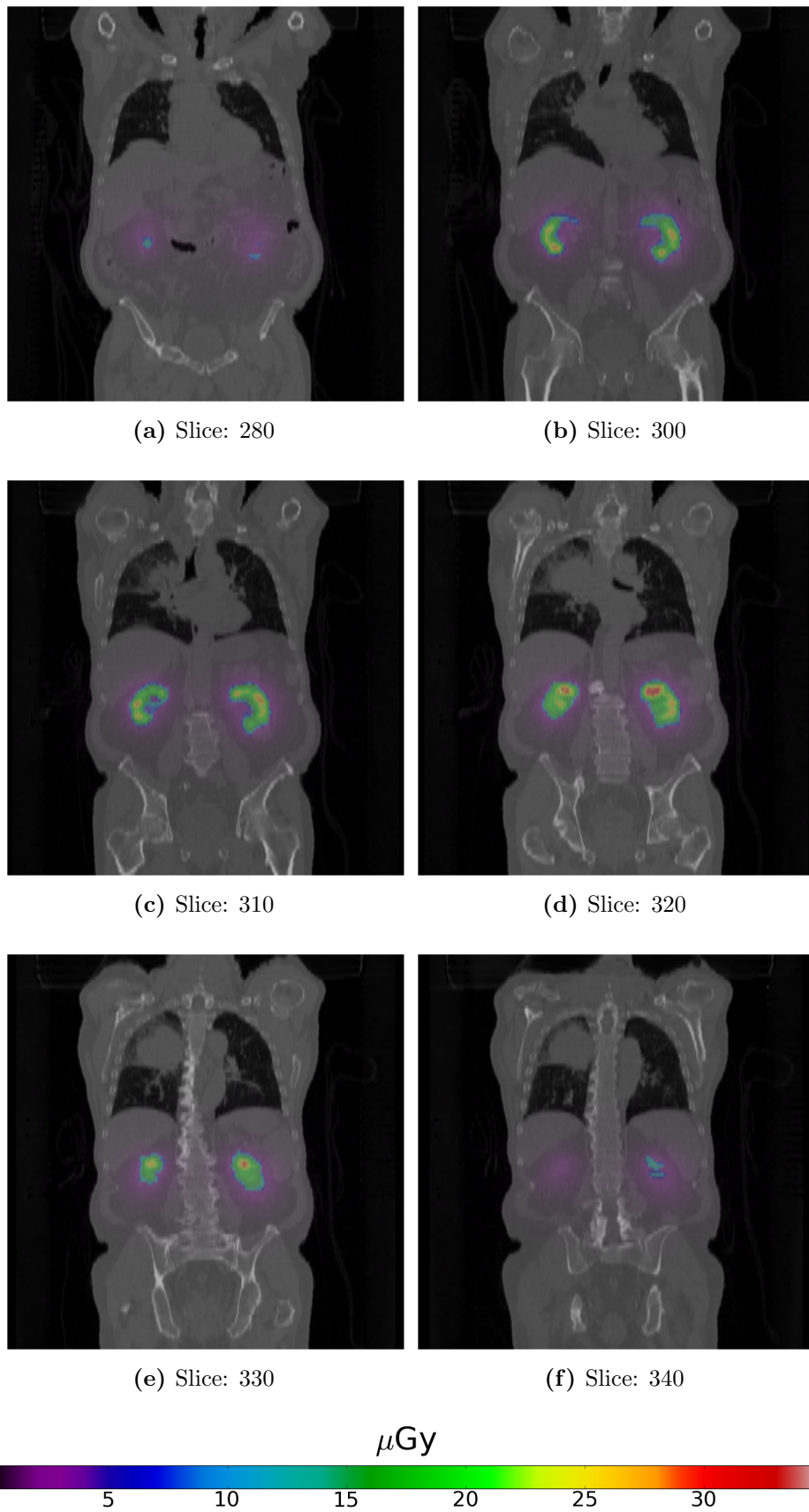


Figure 6.2: Dose distribution of non-uniform activity in both kidneys, overlaid with the patient's low dose CT.

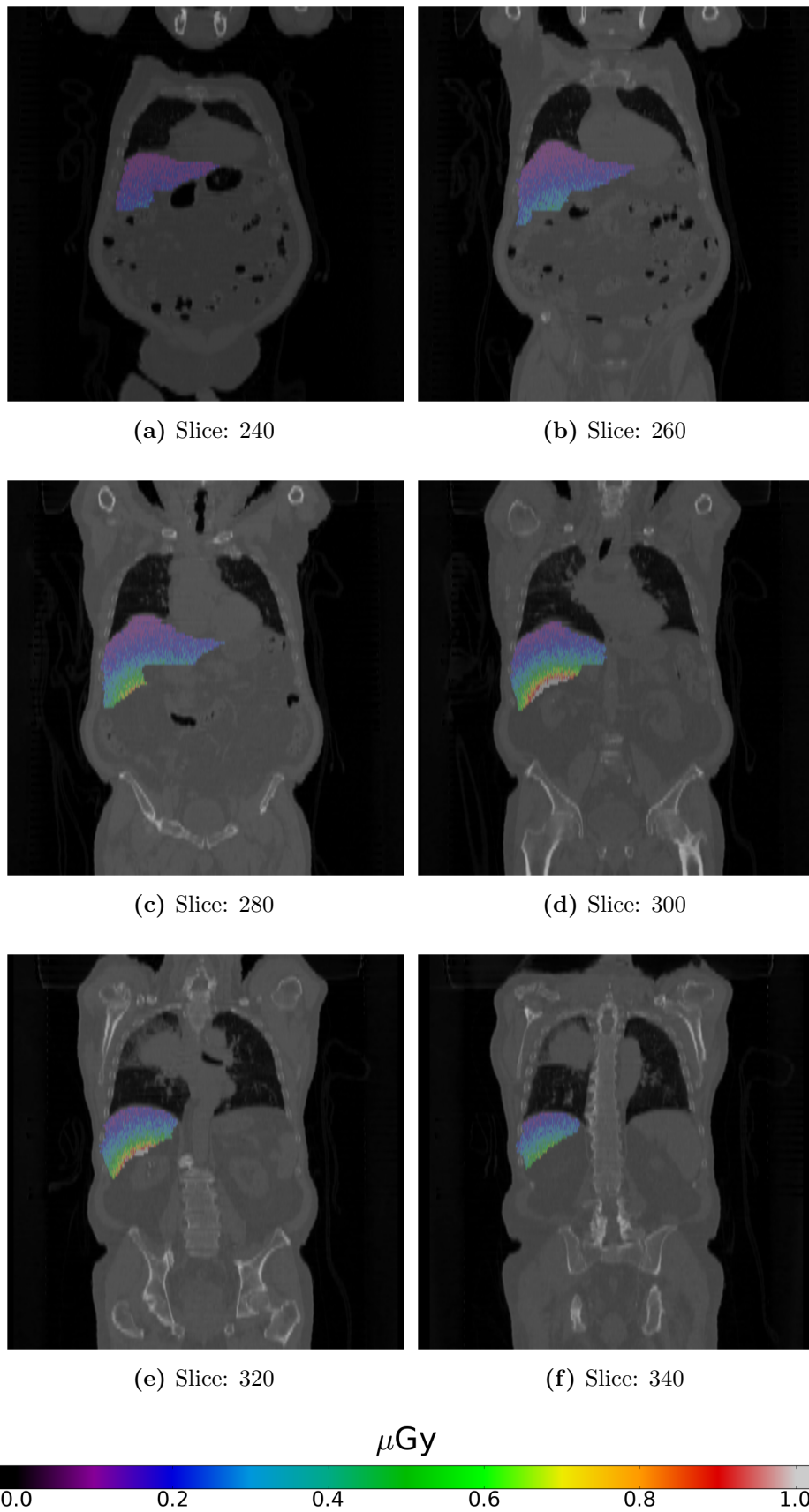


Figure 6.3: Dose distribution in the liver resulting from non-uniform activity in both kidneys, overlaid with the patient's low dose CT.

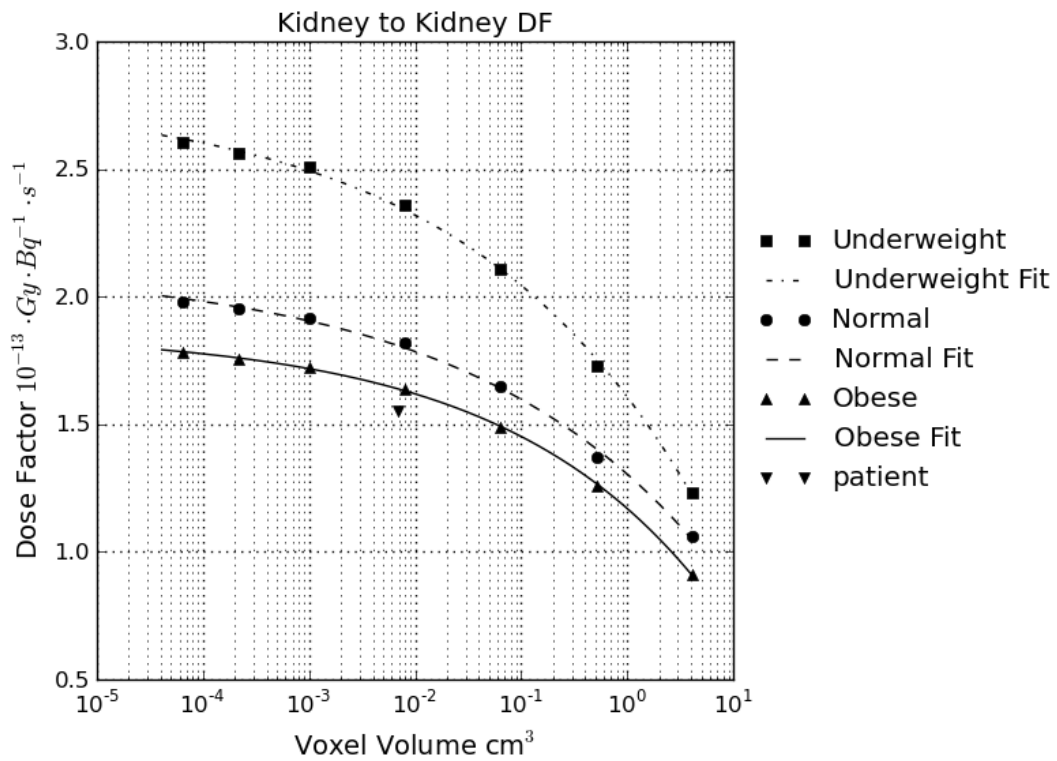
of the computer hardware/software combination. These limitations are not only limited to the Monte Carlo process but also reduce the ability to accurately subsample patient data. In the kidney self-irradiation case the DFs only begin to converge as the voxel size decreases below the current limits of medical imaging equipment. A logical step to resolve this issue of inadequate voxel sampling is to consider fitting the DFs for the XCAT phantom. This is contrary to the results found in section 5.2 where convergence was achieved at 2 mm voxels (figure 5.1 through 5.3).

The DF for uniform activity distributed throughout the kidneys for different voxel volumes are fitted to an equation of the form $y = a - b \cdot x^n$ for the three XCAT phantoms. Where y is the DF in units of $10^{-13} \cdot \text{Gy} \cdot \text{Bq}^{-1} \cdot \text{s}^{-1}$ and x is the voxel volume in cm^3 . Table 6.4 summarises the fitting parameters for the three phantom sizes as well as the coefficient of determination r^2 . Figure 6.4a shows the fitted function for each phantom. Also shown for comparison is the kidney to kidney DF of the Average patient. As the voxel volume approaches zero (i.e. the geometric case) the DF becomes $a \times 10^{-13} \cdot \text{Gy} \cdot \text{Bq}^{-1} \cdot \text{s}^{-1}$, from the fitted parameters. The required correction is most significant for organ self dose

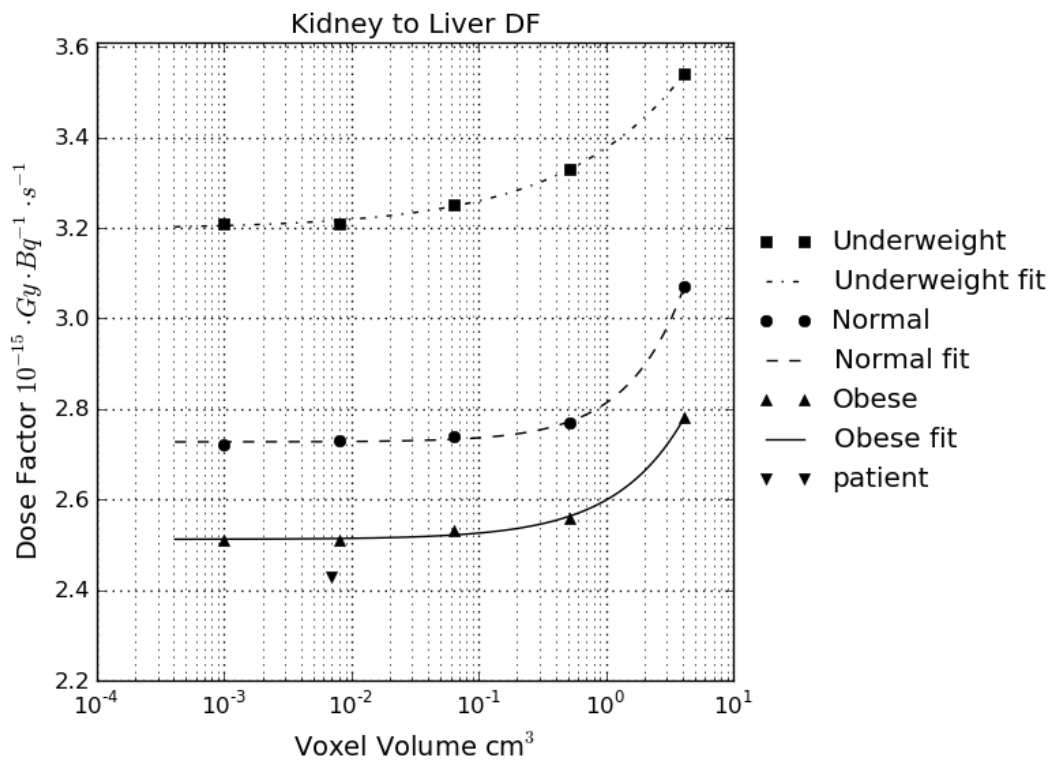
Table 6.4: Fitting parameters for different voxel volumes in the XCAT phantom for the kidneys to kidneys DF. Values are fitted to the equation $y = a - b \cdot x^n$. Where y is the DF in units of $10^{-13} \cdot \text{Gy} \cdot \text{Bq}^{-1} \cdot \text{s}^{-1}$ and x is the voxel volume in cm^3

Phantom	a	b	n	r^2
Small	2.788	1.181	0.201	0.9990
Average	2.117	0.813	0.194	0.9971
Large	1.861	0.691	0.228	0.9996

Even though table 6.1 shows that the kidney to liver DF converges for a voxel size 2 mm or less, values are also fitted to the equation of the form $y = a - b \cdot x^n$. The fitting parameters for figure 6.4b are shown in table 6.5, where $a \times 10^{-15} \cdot \text{Gy} \cdot \text{Bq}^{-1} \cdot \text{s}^{-1}$



(a) Kidney to kidney DF for the XCAT phantom of different phantom sizes.



(b) Kidney to liver DF for the XCAT phantom of different phantom sizes.

Figure 6.4: Fitting DF to voxelised phantoms of different voxel size.

Table 6.5: Fitting parameters for different voxel volumes in the XCAT phantom for the kidneys to liver DF. Values are fitted to the equation $y = a - b \cdot x^n$. Where y is the DF in units of $10^{-15} \cdot \text{Gy} \cdot \text{Bq}^{-1} \cdot \text{s}^{-1}$ and x is the voxel volume in cm^3

Phantom	a	b	n	r^2
Small	3.198	-0.179	0.460	0.9990
Average	2.727	-0.086	0.980	0.9988
Large	2.512	-0.087	0.799	0.9981

is the kidney to liver DF. This trend was also seen in the previous chapter for the simple heterogeneous source to target situation (table 5.7).

From the results of chapter 5 and fitting the XCAT data it is suggested that as a rule of thumb a voxel size of 2 mm or less provides convergence for calculating organ cross doses, where for organ self dose a significantly smaller voxel size is required or must be corrected for.

6.4.2 Scaling patient DF for voxel volume

Using figure 6.4a the patient specific kidney to kidney DF can be scaled to account for voxel volume. The most obvious approach to achieve this scaling is to take the ratio of the DF reference phantom at a voxel volume of zero by the reference phantom DF at a voxel volume of x . Where x is the voxel volume of the patient dose histogram. Using the fitting parameters from the above section this can be written mathematically as equation 6.1.

$$DF_{pat}(0) \approx DF_{pat}(x) \cdot \left(\frac{a}{a - b \cdot x^n} \right) \quad (6.1)$$

Referring to table 6.1 and 6.2, it is decided to normalise the patient DF to the Large XCAT phantom as compared to the Average phantom. This is because the patient and Large XCAT kidney masses are more closely matched. Even though the

total body mass for the Average phantom matches the patient mass the mass of the kidneys is approximately 17 g less than the patient kidney (see following section). Therefore the patient specific kidney to kidney DF becomes $1.76 \times 10^{-13} \cdot Gy \cdot Bq^{-1} \cdot s^{-1}$ scaled up from $1.55 \times 10^{-13} \cdot Gy \cdot Bq^{-1} \cdot s^{-1}$. If normalisation was based on total body weight then the average phantom would have been used to obtain a DF of $1.82 \times 10^{-13} \cdot Gy \cdot Bq^{-1} \cdot s^{-1}$.

From the results obtained the kidney to liver DF converges for larger voxel volumes compared to the kidney to kidney case. Therefore it is not necessary to scale the patient specific kidney to liver DF. It should however be noted that equation 6.1 still holds for this case as $\frac{a}{a-b \cdot x^n}$ is equal to 1.

6.4.3 Organ masses

The organ masses for the XCAT and patient data sets are found by multiplying the total volume of the voxels used to define the organ by the organ density (detailed in section 3.10). Using a similar approach adopted above, the organ mass represented by a voxel volume that approaches zero is obtained by fitting the organ masses in table 6.1 to an equation of the form $y = \alpha - \beta x^\kappa$. The constants α , β and κ are used so that no confusion arises between the constants a , b and n in the previous section.

The constant α represents the organ mass of the XCAT phantom when voxel volume equals zero, where the patient organ mass is found by adopting equation 6.1. Where the correction factor CF_{mass} is defined by equation 6.2.

$$CF_{mass} \equiv \frac{\alpha}{\alpha - \beta \cdot x^\kappa} \quad (6.2)$$

Table 6.6 shows the fitting constants, the mass correction factor and the corrected patient organ mass. The patient kidney and liver mass is therefore 0.269 and 1.619 kg respectively. The coefficient of determination for all of the fitted organ masses is

$r^2 = 0.999$ or better.

An additional point of note from table 6.6 is that the organ masses of the XCAT phantom are relatively small compared to the ICRP reference mass organs. For example the male reference kidney mass is reported as 0.310 kg [144]. From the log file of the underweight, normal and obese XCAT phantoms the kidneys mass is reported as 0.192 kg, 0.258 kg and 0.290 kg respectively. These values match well to the calculated kidney mass for the XCAT phantoms namely 0.187 kg, 0.252 kg and 0.283 kg. The slight differences are introduced in the phantom preparation process i.e. converting surface representations of an organ into a voxel representation.

Table 6.6: Organ mass corrections for voxel volume. For the kidney and liver of the XCAT and kidney data sets.

Organ, Phantom weight	α	β	κ	CF_{mass}^\dagger	Corrected Patient Organ Mass (kg)
kidney, Small	0.187	0.0386	0.4305	1.025	0.270
kidney, Average	0.252	0.0448	0.4468	1.020	0.269
kidney, Large	0.283	0.0491	0.4631	1.028	0.268
liver, Small	1.071	0.1640	0.5021	1.013	1.619
liver, Average	1.470	0.1841	0.4540	1.013	1.620
liver, Large	1.659	0.1990	0.4548	1.013	1.619

[†] Where patient voxel volume is $x = 0.5 \times 0.117 \times 0.117 \text{cm}^3$.

6.5 Agreement to MIRD and OLINDA\EXM

The most widely accepted values for DFs (or S-Values) for nuclear medicine applicable radionuclide are the original MIRD pamphlet 11 [60] and the internal dosimetry software MIRDOSE [81] which has been superseded by OLINDA\EXM [61]. These accepted values have been discussed previously in section 2.9. For self dose in the kidneys pamphlet 11 and RADAR quote a DF of $1.65 \times 10^{-13} \frac{\text{Gy}}{\text{Bq}\cdot\text{s}}$ and $1.68 \times 10^{-13} \frac{\text{Gy}}{\text{Bq}\cdot\text{s}}$ respectively. Table 6.7 provides a summary of the calculated DFs for the kidney self dose.

Table 6.7: Summary of calculated DFs, with organ mass scaling to Reference Man (kidney ← kidney).

Phantom	Organ mass (kg)	DF ($10^{-13} \frac{Gy}{Bq \cdot s}$)	Mass scaled DF ($10^{-13} \frac{Gy}{Bq \cdot s}$)
Small XCAT	0.187	2.79	1.68
Average XCAT	0.252	2.12	1.72
Large XCAT	0.283	1.86	1.70
MIRD 11	0.284	1.65	1.51
OLINDA\EXM	0.299	1.68	1.62
patient	0.269	1.78	1.54

When comparing the values in table 6.7 the DFs for each of the three voxelised XCAT phantoms are notably higher compared to the geometrically defined MIRD 11 and OLINDA\EXM values. It has been shown in the previous chapter that voxelised phantoms using suitably small voxel sizes will match geometric phantom results. Therefore any difference between the geometric and voxelised phantom results are due to the differences in individual organ shape and size. The three XCAT phantoms have a significantly smaller kidney mass when compared to not only the geometric phantoms but also reference man, thus resulting in a higher DF. These differences again highlight the reliance on the phantom used to obtain the organ DFs.

As an additional attempt to compare the DFs for the model based phantoms it will be assumed that equation 2.13 is a reasonable correction for the kidney to kidney case. Assumptions related to this correction are discussed in section 2.6. Table 6.7 shows results of scaling the kidney self dose DFs to an organ mass of 310 g i.e. reference man. Differences in the scaled DF can be explained by three key points. These are as follows:

- differences in organ shapes
- methodology for calculating absorbed energy
- equation 2.13 is only an approximation

Differences in organ shape may be significant enough to effect the scaled DF, for

example the kidneys in the mathematical phantom defined by two ellipsoids cut by a plane which are not as realistic as using the XCAT surface method. This effect on the DF is seen in the differences between the XCAT and OLINDA\EXM results.

The second explanation for differences in the DFs is from the differences in the Monte Carlo approaches used. In particular the contribution of non-penetrating radiation. The methodologies for handling non-penetrating radiation for MIRD pamphlet 11 and OLINDA\EXM are explained in section 2.9 and are by their nature are an approximation. Whereas GATE used a more physically rigorous model in the direct Monte Carlo simulation.

Finally when the scaled DFs for the three XCAT phantoms are compared to each other the differences are not due to differences in methodology, or organ shape. Some small differences may have been introduced by the scaling performed to create the data sets, however this is considered minimal since NURBS surfaces have been used. This comparison leads to the conclusion that organ mass scaling is only a crude approximation. From the results obtained it is suggested that adapting phantom results to individual patients through mass scaling is not necessarily appropriate. The scaled patient specific kidney to kidney DF (shown in table 6.7) adds additional evidence for this.

The patient specific kidney to kidney DF is calculated by direct Monte Carlo simulation which takes into account not only the patient's organ size and shape but also its non-uniform activity distribution. As a direct comparison, the patient kidneys have a mass (0.269 kg) between the Average (0.252 kg) and Large (0.283 kg) XCAT phantoms. However the calculated patient specific DF of $1.78 \times 10^{-13} \frac{Gy}{Bq \cdot s}$ is lower than the Average ($2.12 \times 10^{-13} \frac{Gy}{Bq \cdot s}$) and Large ($1.86 \times 10^{-13} \frac{Gy}{Bq \cdot s}$) XCAT phantoms. If only the organ mass is considered then the patient specific DF should have fallen between the Average and Large XCAT values, however this is not the case and is caused by the non-uniform activity distribution.

In the kidney to liver DF case, pamphlet 11 and RADAR quote DFs of $2.18 \times 10^{-15} \frac{Gy}{Bq \cdot s}$ and $2.06 \times 10^{-15} \frac{Gy}{Bq \cdot s}$ respectively. For each phantom model the kidney to liver DF is also scaled against the source organ mass by equation 2.14. Table 6.8 is a summary of the DFs.

Table 6.8: Summary of calculated DFs (liver \leftarrow kidney).

Phantom	Target Organ mass (kg)	DF ($10^{-15} \frac{Gy}{Bq \cdot s}$)	Mass scaled DF ($10^{-15} \frac{Gy}{Bq \cdot s}$)
Small XCAT	1.07	3.20	2.28
Average XCAT	1.47	2.73	2.38
Large XCAT	1.66	2.51	2.36
MIRD 11	1.81	2.18	2.06
OLINDA\EXM	1.91	2.06	2.01
patient	1.62	2.43	2.21

Again when comparing the source to target DFs for all phantoms and reference values the DF are significantly different compared to each other. For the phantoms that have a mass scaled to the reference kidney mass of 310 g the DF(liver \leftarrow kidney) has a range of $2.01 \times 10^{-15} \frac{Gy}{Bq \cdot s}$ to $2.38 \times 10^{-15} \frac{Gy}{Bq \cdot s}$. Again this evidence suggests that considerable care is required when adapting phantom results to individual patients.

6.6 Variations in Human Anatomy

The dose factors calculated in this thesis have solely concentrated on the kidneys and liver of the XCAT phantom and an individual patient. Both the XCAT phantom and the patient have organs defined that are individual to either the standardised phantom or individual patient. It is however important to recognise that the significant variability between individual patient organ shapes and sizes have not been taken into account. This variability between patients is particularly true for the liver that may vary significantly in not only mass but also shape and will undoubtedly lead to a change in the dose factors calculated.

6.7 Chapter Summary

This chapter has made use of GATE as a tool for calculating organ doses from uniform and non-uniformly distributed F-18 in both a standardised model of human anatomy and actual patient data. It has been shown that the creation of dose histograms and iso dose contours of the energy deposited from the distributed activity is easily calculated in GATE.

The XCAT phantom has been used to investigate the effect of voxel size on the DF. It was found that significantly small voxel sizes are required to achieve convergence for the organ self dose. This spatial sampling issue in the patient specific DF was corrected for by using fitted XCAT data. From the results of chapter 5 and fitting the XCAT data it is suggested that as a rule of thumb a voxel size of 2 mm or less provides convergence for calculating organ cross doses.

A comparison to the highly accepted OLINDA\EXM dosimetry code has also been completed. It can be concluded that differences in patient organ masses contribute to significant variability in the calculated DFs. These results suggests that considerable care is required when adapting phantom results to individual patients. It can therefore also be recommended that where available individual patient specific dosimetry should be calculated using direct Monte Carlo simulation in favor of organ mass scaling.

Chapter 7

Conclusions and Future work

It has been the objective of this thesis to assess the use of patient specific dosimetry calculations using the GATE Monte Carlo package. After validating GATE, the Monte Carlo package was used to demonstrate the significant variability of model based phantoms of different sizes compared to an individual patient. It was shown that organ mass scaling of model based phantoms to individual phantoms is not necessarily suitable and where available individual patient specific dosimetry should be calculated using direct Monte Carlo simulation.

This chapter provides a brief summary of work completed to achieve that objective. It also proposes future work to continue accurate patient specific dosimetry calculations.

7.1 Validating GATE

A validation of GATE against a simple benchmark such as geometric and voxelised spheres of uniformly distributed radioactivity, promotes confidence in the absorbed dose calculations from GATE. The use of the MIRD spheres as a benchmark for Monte Carlo transport codes have been discussed and possible errors within the original values calculated in MIRD pamphlet 8 have been shown.

A comparison of the *standard*, *low energy* and *PENELOPE* physics packages have been made and all show excellent agreement to the gold standard for self absorption in unit density spheres. This agreement is not only limited to geometrically defined phantoms but also voxelised phantoms. From the evidence gathered from the comparison it was decided to use the *low energy* physics package since it provided the most suitable balance between simulation accuracy and voxelised simulation time for internal dosimetry applications.

It was shown in section 5.4 that for voxelised phantoms, the specific absorbed fraction is a more accurate dosimetric quantity for voxelized phantoms compared to the absorbed fraction alone. This finding also leads to the useful rule of thumb that for a source to target regions the specific absorbed fraction requires a voxel size of 2 mm to achieve an appropriate level of accuracy.

The validation of GATE provided in chapters 4 and 5 of this thesis increases the likelihood of the software becoming more accepted in a clinical setting.

7.2 Patient and Model Based Absorbed Dose Calculations

Realistic models of human anatomy such as the XCAT phantom will soon replace traditional stylised phantoms for internal dosimetry calculations. The practical application of using both model and patient specific voxelised phantoms in the GATE Monte Carlo package have been shown in this thesis. The reliance of voxel size on accurate calculations of DFs was investigated using the XCAT phantom.

For organ self-irradiation voxel sizes smaller than currently available from diagnostic imaging modalities are required therefore using voxelised phantoms acquired from true patient images may require a correction for insufficient voxel sampling.

A correction for the patient kidney self dose has been calculated using the XCAT

phantom and applied to a patient specific situation. In this work the scalable XCAT phantom has also been used to show that a voxel size of 2 mm or less is suitable for accurate calculations of organ cross dose.

Model based phantoms are designed to represent reference individuals. By comparing the scaled XCAT phantoms with patient and traditional phantoms it has been shown that differences in organ shape, mass, and activity distribution all affect the calculated DF. To achieve a relative comparison the calculated DFs for each of these phantoms were scaled to an organ mass comparable to reference man. It was concluded from the mass scaled DFs that considerable care is required when adapting model based phantom results to individual patients. As differences in patient organ masses contribute significant variability to the dosimetry calculation it was therefore recommended that where available individual patient specific dosimetry should be calculated using direct Monte Carlo simulation in favor of organ mass scaling.

7.3 Future work

7.3.1 Automation

At present patient specific dosimetry for internal radionuclide's is a labour intensive and time consuming process. To further increase the ease of dosimetry calculations from PET/CT data, much of the process should be fully automated.

One challenging aspect of this is automated organ segmentation. Automated organ segmentation would remove the human judgement from defining the boundaries of patient organs. It may be easiest to automatically segment the CT image then overlay the co-registered PET image to assist with the PET segmentation. Better segmentation of radiosensitive organs including red bone marrow would also increase the likelihood of the effective dose being correctly calculated.

Investigations into the simulation speed and additional variance reduction tech-

niques will also move the methods described in this thesis out of the research domain and into clinical nuclear medicine.

7.3.2 Calculation of additional organs

With the increased development and use of voxelised phantoms equation 6.1 has been proposed to calculate the organ dose factor at a voxel volume of zero from the DF at a voxel volume of x . The fitting parameters a , b and n have been derived from the XCAT phantom using the kidneys as the source organ. The dependence of these parameters on the source and target organ requires additional investigation for other organs in the body. This should include larger source organs including the brain, lungs, and liver as well as smaller organs such as the Gallbladder, Thymus and Thyroid.

7.3.3 Dynamic patient activity distribution

The prime objective of this thesis has been the calculation of static absorbed doses and so has not concentrated on the evaluation of the kinetic properties of radiopharmaceuticals. Continuing investigation into the simulation of dynamic activity distribution will increase the accuracy of patient specific dosimetry evaluations. In section 6.3 dose histograms were shown for a patient injected with ^{18}F -FDG. The calculated DFs are accurate for the time interval of 70 min after the injection of ^{18}F -FDG, i.e. the standard duration of a whole body PET scan.

Frame or list mode dynamic acquisitions are one such method for obtaining time activity curves of individual organs. Time activity curves may then be applied to the Monte Carlo calculation. An example of such an application would be the uptake of a new radiopharmaceutical or abnormal activity uptake in patients receiving therapeutic nuclear medicine procedures. A dynamic acquisition is useful for calculating time activity curves of radiopharmaceuticals with relatively short effective

half-lives. This is true of diagnostic radiopharmaceuticals however individual patient dose estimates are rarely needed for these short effective half-lives. As discussed previously individual patient dose estimates are becoming essential for therapeutic applications, where the effective half-life is relatively long and may be several days. Obtaining time activity curves for long effective half-lives may also be associated with errors as it may only be possible to obtain three to five time points. An error in calculating the time activity curve will undoubtedly effect the calculation of the cumulative activities

7.4 Final concluding remarks

The desire for patient specific dosimetry estimates of internally distributed radioactivity is realised by using Monte Carlo simulations of voxelised phantoms. Individual organ mass scaling of traditional stylised phantoms will therefore soon be replaced by voxelised phantoms such as XCAT. This thesis has shown that the GATE toolkit provides suitable accuracy to perform Monte Carlo simulations of voxelised phantoms. By using the validated GATE toolkit it has been shown that the application of these phantoms must make some considerations for voxel size. Changes in patient organ mass greatly affect dosimetry calculations and therefore where available direct Monte Carlo simulations of individual patients should be considered.k

Appendix A

Gate Macros

This appendix contains a number of GATE, python and bash scripts used for the simulation completed in the sections above.

A.1 PBS Script Example

```
#!/bin/bash
# File Name: pbs-script.sh
# Usage: qsub pbs-script.sh

# Sets the job name
#PBS -N gate_job

# Requests a single CPU to be used for this job
#PBS -l nodes=1

# Sets the maximum time the job will take (2h 30min)
#PBS -l walltime=02:30:00

# Changes directory to your execution directory
cd $PBS_O_WORKDIR

# Set all required GATE variables
source /home/some_path/env_gate.sh

# Run GATE
```

Gate my_macro.mac

A.2 MIRD Spheres

The following are scripts used to simulate the MIRD spheres in GATE.

A.2.1 GATEv3.1.2 MIRD

```
# A parameterized macro for the
# absorbed fraction in a sphere.
#
# usage: Gate -a radius 0.620350 -a energy 0.14 -a time 15.0 spheres.mac
#
# note radius in cm, energy in Mev, time in sec.

# V I S U A L I S A T I O N
#/control/execute visu.mac

# W O R L D
/gate/world/geometry/setXLength 0.1 m
/gate/world/geometry/setYLength 0.1 m
/gate/world/geometry/setZLength 0.1 m
/gate/world/setMaterial MirdSoftTissue

# D E T E C T O R
/gate/world/daughters/name scanner
/gate/world/daughters/insert sphere
/gate/world/setMaterial MirdSoftTissue
/gate/scanner/geometry/setRmax {radius} cm
/gate/scanner/vis/setColor cyan

/gate/scanner/daughters/name l1
/gate/scanner/daughters/insert sphere
/gate/world/setMaterial MirdSoftTissue
/gate/l1/geometry/setRmax {radius} cm
/gate/l1/vis/setColor red

/gate/systems/scanner/level1/attach l1
/gate/l1/attachCrystalSD

# P H Y S I C S
/gate/physics/gamma/selectRayleigh inactive
/gate/physics/gamma/selectPhotoelectric standard
```

```

/gate/physics/gamma/selectCompton standard

# I N A C T I V E   S E C O N D A R Y   E L E C T R O N S
/gate/physics/setElectronCut 30.01 cm
# I N A C T I V E   X - R A Y S
/gate/physics/setXRayCut 1. GeV
/gate/physics/setDeltaRayCut 1. GeV
/gate/physics/verbose 1

# I N I T I A L I Z E
/gate/geometry/enableAutoUpdate
/run/initialize

# S O U R C E
/gate/source/addSource lineS
/gate/source/lineS/setActivity 1200000 Bq
/gate/source/lineS/gps/type Volume
/gate/source/lineS/gps/shape Sphere
/gate/source/lineS/gps/radius {radius} cm
/gate/source/lineS/gps/particle gamma
/gate/source/lineS/gps/energytype Mono
/gate/source/lineS/gps/monoenergy {energy} MeV

# O U T P U T
/gate/output/verbose 1
/gate/output/ascii/setFileName {energy}_{radius}_abfrac
/gate/output/ascii/setOutFileHitsFlag 1
/gate/output/ascii/setOutFileSinglesFlag 0
/gate/output/root/disable

# S T A R T
/gate/application/setTimeSlice {time} s
/gate/application/setTimeStart 0. s
/gate/application/setTimeStop {time} s
/gate/application/startDAQ

```

A.2.2 Calculate absorbed fractions

```

#!/usr/bin/python
# filename: sum_energy.py
# sum energy deposited by hit from gateHits.dat
# Usage: python sum_energy.py hits.dat run.dat

import sys

def main(energy, iname = 'gateHits.dat', runname = 'gateRun.dat') :

```

```

f = open(iname, 'r')
var11 = []
total = 0
while True :
    line = f.readline()
    if not line : break
    if len(line) == 0 : continue
    args = line.split()
    var11.append(float(args[11]))
    total = total + float(args[11])
f.close()

f = open(runname, 'r')
line = f.readline()
emit = float(line.split()[0]) * energy
f.close()

print "%s %s %s" % (str(total), str(emit), str(total / emit))

if __name__ == '__main__' :
    arg = sys.argv
    if len(arg) != 3: sys.exit("Usage: python hits.dat run.dat")
    main(float(arg[1][:5]), iname = arg[1], runname = arg[2])

```

A.2.3 GATEv6.0 physics

```

#
# Physics Example Standard proceses
#
/gate/physics/addProcess PhotoElectric
/gate/physics/addProcess Compton
/gate/physics/addProcess GammaConversion

/gate/physics/addProcess ElectronIonisation
/gate/physics/processes/ElectronIonisation/setStepFunction e+ 0.01 0.1 mm
/gate/physics/processes/ElectronIonisation/setStepFunction e- 0.01 0.1 mm

/gate/physics/addProcess Bremsstrahlung
/gate/physics/addProcess PositronAnnihilation

/gate/physics/addProcess MultipleScattering e+
/gate/physics/addProcess MultipleScattering e-
/gate/physics/processes/MultipleScattering/
    setGeometricalStepLimiterType e- distanceToBoundary
/gate/physics/processes/MultipleScattering/
    setGeometricalStepLimiterType e+ distanceToBoundary

```



```
/gate/physics/setEMin 0.1 keV
/gate/physics/setEMax 10 GeV
/gate/physics/setDEDXBinning 77
/gate/physics/setLambdaBinning 77

#
# Physics Example LowEnergy library
#
/gate/physics/addProcess LowEnergyPhotoElectric
/gate/physics/addProcess LowEnergyCompton
/gate/physics/addProcess LowEnergyGammaConversion
/gate/physics/addProcess LowEnergyRayleighScattering

/gate/physics/addProcess LowEnergyBremsstrahlung e-
/gate/physics/addProcess LowEnergyElectronIonisation e-

/gate/physics/addProcess ElectronIonisation e+
/gate/physics/addProcess Bremsstrahlung e+
/gate/physics/addProcess PositronAnnihilation e+

/gate/physics/addProcess MultipleScattering e+
/gate/physics/addProcess MultipleScattering e-
/gate/physics/processes/MultipleScattering/
    setGeometricalStepLimiterType e- distanceToBoundary
/gate/physics/processes/MultipleScattering/
    setGeometricalStepLimiterType e+ distanceToBoundary

/gate/physics/setEMin 0.1 keV
/gate/physics/setEMax 10 GeV
/gate/physics/setDEDXBinning 77
/gate/physics/setLambdaBinning 77

#
# Physics Example Penelope Library
#
/gate/physics/addProcess PenelopePhotoElectric
/gate/physics/addProcess PenelopeCompton
/gate/physics/addProcess PenelopeGammaConversion
/gate/physics/addProcess PenelopeRayleighScattering

/gate/physics/addProcess PenelopeBremsstrahlung e-
/gate/physics/addProcess PenelopeElectronIonisation e-

/gate/physics/addProcess PenelopeElectronIonisation e+
/gate/physics/addProcess PenelopeBremsstrahlung e+
/gate/physics/addProcess PenelopePositronAnnihilation e+

/gate/physics/addProcess MultipleScattering e+
```

```

/gate/physics/addProcess MultipleScattering e-
/gate/physics/processes/MultipleScattering/
    setGeometricalStepLimiterType e- distanceToBoundary
/gate/physics/processes/MultipleScattering/
    setGeometricalStepLimiterType e+ distanceToBoundary

/gate/physics/setEMin 0.1 keV
/gate/physics/setEMax 10 GeV
/gate/physics/setDEDXBinning 77
/gate/physics/setLambdaBinning 77

```

A.2.4 Gate version 6 MIRD simulation

```

import sys
import os
import optparse

__email__ = "kevin.hickson@petnm.unimelb.edu.au"

def macro(radius, energy, N, phys):
    f = open('sphere_py.mac', 'w')

    if phys == 'std': ex = ' egammaStandardPhys.mac'
    elif phys == 'low': ex = ' egammaLowEPhys.mac'
    elif phys == 'pen': ex = ' egammaPenPhys.mac'
    else: sys.exit('Fail to set physics')

    oname = "%s_%s_%s" % (energy, radius, phys)

    string = ""
    string = ""#Macro from mkmacro.py Gate6 compatable ... KJH Aug 2010
/gate/geometry/setMaterialDatabase ./GateMaterials.db
/gate/world/geometry/setXLength 6 cm
/gate/world/geometry/setYLength 6 cm
/gate/world/geometry/setZLength 6 cm
/gate/world/setMaterial MirdSoftTissue
/gate/world/daughters/name scanner
/gate/world/daughters/insert sphere
#/gate/scanner/setMaterial MirdSoftTissue
/gate/scanner/setMaterial Vacuum
/gate/scanner/geometry/setRmin 0.0 cm
/gate/scanner/geometry/setRmax "" + str(radius) + "" cm
/gate/scanner/daughters/name l1
/gate/scanner/daughters/insert sphere
/gate/l1/setMaterial MirdSoftTissue
/gate/l1/geometry/setRmin 0.0 cm

```

```

/gate/l1/geometry/setRmax "" + str(radius) + "" cm
/gate/systems/scanner/level1/attach l1
/gate/l1/attachCrystalSD
/control/execute"" + ex + ""
/gate/run/initialize
/gate/source/addSource lineS
/gate/source/lineS/setActivity 1000000 Bq
/gate/source/lineS/gps/type Volume
/gate/source/lineS/gps/shape Sphere
/gate/source/lineS/gps/radius "" + str(radius) + "" cm
/gate/source/lineS/gps/particle gamma
/gate/source/lineS/gps/energytype Mono
/gate/source/lineS/gps/monoenergy "" + str(energy) + "" MeV
/gate/output/verbose 1
/gate/output/ascii/enable
/gate/output/ascii/setFileName "" + oname + ""
/gate/output/ascii/setOutFileHitsFlag 1
/gate/output/ascii/setOutFileSinglesFlag 0
/gate/application/setTotalNumberOfPrimaries "" + str(N) + ""
/gate/application/start
    ""

    f.write(string)

if __name__ == '__main__':
    parser = optparse.OptionParser(usage = \
                                   '%prog [options]',
                                   epilog = \
                                   ('Problems to: %s\n' % __email__))

    parser.add_option('-r', # '--radius',
                     dest= 'radius',
                     default = '0.62',
                     action = 'store',
                     help = '''set radius of sphere in cm''')

    parser.add_option('-e', # '--energy',
                     dest= 'energy',
                     default = '0.140',
                     action = 'store',
                     help = \
                     '''set initial photon energy in MeV''')

    parser.add_option('-N', # '--number',
                     dest= 'number',
                     default = '10',
                     action = 'store',
                     help = \
                     '''set number of events to simulate''')

```

```
parser.add_option('-p', #'--phys',
                  dest= 'phys',
                  default = 'std',
                  action = 'store',
                  help = '''set physics processes to use''')

(options, args) = parser.parse_args()
p = options.phys
if p != 'std' and p != 'low' and p != 'pen':
    print "%s not available use;" % options.phys
    print "'std' for standard processes"
    print "'low' for lowenergy livermore processes"
    print "'pen' for Penelope processes"
    sys.exit(1)

macro(options.radius, options.energy, options.number, options.phys)

#!/bin/bash
# File Name: pbs-script.sh
# Usage: qsub pbs-script.sh
#PBS -N gate_job
#PBS -l nodes=1
#PBS -l walltime=02:30:00

cd $PBS_O_WORKDIR

# Set all required GATE variables
source /home/some_path/env_gate.sh
ln -s /home/some_path/GateMaterials.db

energy="0.140"
number="100000"

phys="std
low
pen"

radii="0.620350490899
0.781592641797
0.984745021843
1.12725165179
1.2407009818
1.33650461757
1.68389030096
2.12156883589
2.42859006301
2.67300923514
```

```
2.87941191148
```

```
"
```

```
for i in $phys; do
  for j in $energy; do
    for k in $radii; do
      python mkmacro.py -N "$number" -r "$k" -e "$j" -p "$i"
      echo python mkmacro.py -N "$number" -r "$k" -e "$j" -p "$i"
      Gate sphere_py.mac
      abf="$j_" "$k_" "$i"
      run_ver="$abf"Hits.dat "$abf"Run.dat
      result_ver=results_"$i_" "$j".txt
      echo python sum_energy_diposited.py "$run_ver" to "$result_ver"
      python sum_energy_diposited.py "$run_ver" >>"$result_ver"
      rm -f "$abf"*.dat
      echo Have removed "$abf" dat files.
    done
  done
done
```

A.3 Voxel Phantoms

A.3.1 Interfile creation

```
class createInterfile:
    """Create an voxel map in interfile format"""
    def __init__(self, oname, radius, pixsize, imgsize, verbose=False,
                 xmedcon = False, mix = False):
        self.verbose = verbose
        self.oname = oname
        self.radius = float(radius) * 10. #convert to mm.
        self.xmedcon = xmedcon

        self.pixsize = float(pixsize)
        self.imgsize = int(imgsize)

        string = "\nVerbose has been set to TRUE \n\n"
            "    Header file will be saved as: %s.h33\n"
            "    Image file will be saved as: %s.i33\n"
            "    Radius of sphere set to: %s mm\n"
            % (self.oname, self.oname, self.radius)
        self.v_print(string)

        if mix == False: self.create()
```

```

else: pass

def create(self):
    self.get_scaling_factor()
    self.create_image()

    self.create_header()
    self.vox_sphere()

    if self.xmedcon: self.openxmedcon()

def get_scaling_factor(self):
    self.voxelsize = self.imgsize / self.pixsize

def create_image(self):
    """Use 16 bit unsigned integer if this is to run in Gate"""
    datatype = numpy.uint16
    self.image = numpy.zeros(self.voxelsize**3, datatype).reshape(\
        self.voxelsize, self.voxelsize, self.voxelsize)
    self.v_print('Created image with dtype %s' % datatype)

def openxmedcon(self):
    os.system('xmedcon %s.h33' % self.iname)

def set(self, i, j, k):
    if ((i - (self.voxelsize/2.)) * self.pixsize)**2 + \
        ((j - (self.voxelsize/2.)) * self.pixsize)**2 + \
        ((k - (self.voxelsize/2.)) * self.pixsize)**2 < self.radius**2:
        self.image[i][j][k] = 1

def vox_sphere(self):
    self.v_print("Start image ...")
    p = 0.1
    for i in range(self.voxelsize):
        if i / (p*self.voxelsize) >= p:
            self.v_print('    %s percent done.' % (p * 100))
            p = p + 0.1
        for j in range(self.voxelsize):
            for k in range(self.voxelsize):
                self.set(i,j,k)

    self.v_print('    Saving %s.i33' % self.iname)
    od = open('%s.i33' % self.iname, 'wb')
    od.write(self.image)
    od.close()
    self.v_print('    All done.\n')

def get_gate_trans(self):

```

```

return (self.pixsize * self.voxelsize) / 2.0

def get_trans(self):
    return self.imagesize / 2.0

def create_header(self):
    """Create a header that will work with GATE"""

    self.v_print('Saving header file %s.h33' % self.iname)
    oh = open('%s.h33' % self.iname, 'wb')
    oh.write('!INTERFILE :=\n')
    oh.write('!imaging modality := nucmed\n')
    oh.write('!originating system := greetings\n')
    oh.write('!version of keys := 3.3\n')
    oh.write('date of keys := 1996:09:24\n')
    oh.write('conversion program := python\n')
    oh.write('program author := KJH\n')
    oh.write('program version := 0.01\n')
    oh.write('program date := 2009:09:17\n')
    oh.write(';\n')
    oh.write('!GENERAL DATA :=\n')
    oh.write('!data offset in bytes := 0\n')
    oh.write('!name of data file := %s.i33\n' % self.iname)
    oh.write('patient name := gate\n')
    oh.write('!patient ID := gate\n')
    oh.write('!patient dob := 1985:11:01\n')
    oh.write('!patient sex := Unknown\n')
    oh.write('!study ID := brain\n')
    oh.write('exam type := 2D study\n')
    oh.write('data compression := none\n')
    oh.write('data encode := none\n')
    oh.write(';\n')
    oh.write('!GENERAL IMAGE DATA :=\n')
    oh.write('!type of data := Tomographic\n')
    oh.write('!total number of images := %d\n' % self.voxelsize)
    oh.write('study date := 2009:09:17\n')
    oh.write('study time := 00:00:00\n')
    oh.write('imagedata byte order := LITTLEENDIAN\n')
    oh.write(';\n')
    oh.write('number of energy windows := 1\n')
    oh.write(';\n')
    oh.write('energy window [1] :=\n')
    oh.write('energy window lower level [1] :=\n')
    oh.write('energy window upper level [1] :=\n')
    oh.write('flood corrected := N\n')
    oh.write('decay corrected := N\n')
    oh.write(';\n')
    oh.write('!number of images/energy window := %d \n' \
            % self.voxelsize)

```

```

oh.write('!process status := Reconstructed\n')
oh.write('!matrix size [1] := %d \n' % self.voxelsize)
oh.write('!matrix size [2] := %d \n' % self.voxelsize)
oh.write('!number format := unsigned integer\n')
oh.write('!number of bytes per pixel := 2\n')
oh.write('scaling factor (mm/pixel) [1] := %s\n' % self.pixsize)
oh.write('scaling factor (mm/pixel) [2] := %s\n' % self.pixsize)
oh.write('!number of projections := %d\n' % self.voxelsize)
oh.write('!extent of rotation :=\n')
oh.write('!time per projection (sec) := 0\n')
oh.write('study duration (sec) := 0\n')
oh.write('!maximum pixel count := +1.632600e+04\n')
oh.write('patient orientation := head_in\n')
oh.write('patient rotation := supine\n')
oh.write(';\n')
oh.write('!SPECT STUDY (reconstructed data) :=\n')
oh.write('method of reconstruction := Unknown\n')
oh.write('!number of slices := %d\n' % self.voxelsize)
oh.write('number of reference frame := 1\n')
oh.write('slice orientation := Transverse\n')
oh.write('slice thickness (pixels) := %s\n' % self.pixsize)
#oh.write('slice thickness (pixels) := 1.000\n')
oh.write('centre-centre slice separation (pixels) := %s\n' \
        % self.pixsize)
#oh.write('centre-centre slice separation (pixels) := 1.000\n')
oh.write('filter name := Unknown\n')
oh.write('filter parameters := Cutoff\n')
oh.write('method of attenuation correction := measured\n')
oh.write('scatter corrected := N\n')
oh.write('oblique reconstruction := N\n')
oh.write('!END OF INTERFILE :=\n')
oh.close()
self.v_print('saved.')
```

```

def v_print(self, string):
    """Print if verbose is true"""
    if self.verbose: print str(string)
```

A.3.2 Processing voxel dose

```

class Dose:
    def __init__(self, interfileHeader, DoseFile, GateRun, energy, density,
                 quiet = False, xmedI = False, batch = False):

        self.interfileHeader = interfileHeader
        self.DoseFile = DoseFile
```

```

self.GateRun =GateRun
self.quiet = quiet
self.energy = float(energy)
self.rho = float(density)
self.batch = batch

if xmedI:
    subprocess.call('xmedcon %s' % interfileHeader, shell=True)
    sys.exit(0)

self.read_run()
self.readInterfile()

# change shape
new = numpy.zeros_like(self.ds.image)
int = numpy.where((self.ds.image == 2))
new[int] = 1
self.ds.image = new
#

self.readBinfile()

self.give_results()

def read_run(self):
    f = open(self.GateRun)
    self.number = float(f.readline())
    f.close()

def readInterfile(self):
    self.ds = Interfile.Read(self.interfileHeader)
    self.getCorrectFile()
    self.ds.get_image()

def getCorrectFile(self):
    """Get the correct file path from the interfile"""
    i33_a = self.ds.header['!nameofdatafile'][0]

    if os.path.isfile(i33_a):
        pass
    else:
        i33 = os.path.join(os.path.dirname(self.interfileHeader), i33_a)
        if os.path.isfile(i33):
            self.ds.header['!nameofdatafile'] = [i33]
            if self.quiet == False: warnings.warn(\
                'Found file under: \n%s\nUseing it as the image file!\n\
                % i33)
        else:
            raise IOError('No File %s, The header file is incorrect!'\

```

```

                                                                    % i33_a)
    sys.exit(1)

def readBinfile(self):
    datatype = numpy.float32
    shape = self.ds.image.shape
    size = 1
    for i in range(len(shape)): size = size * shape[i]

    try:
        fd = open(self.DoseFile)
        self.DoseImg = \
            numpy.fromfile(fd, datatype, size).reshape(shape)
        fd.close()
    except ValueError:
        msg = 'The Interfile and Dose.bin file are not the same!\n'\
            'Are you sure the Dose file was generated by this'\
            'interfile?'
        raise ValueError(msg)

def give_results(self):
    self.sum_dose()
    self.delta()
    self.Energy()
    self.absorbfraction()
    self.S_value()

    if self.batch:
        result = '%s %s %s %s %s %s' % \
            (self.interfileHeader, self.ds.image.shape, self.total_dose,
             self.eng, (self.number * self.energy), self.abfrac)

    else:
        result = '=====\n'\
            ' Shape: %s \n'\
            ' iname: %s \n\n'\
            ' Absorb Fraction: %s \n'\
            ' Delta: %s (kg.Gy / Bq.s)\n'\
            ' S-Value: %s (Gy)\n\n'\
            ' Total Dose: %s (Gy)\n'\
            ' Total eng: %s (MeV)\n'\
            '=====\n'\
            % (self.ds.image.shape, self.interfileHeader, self.abfrac, \
              self.delta, self.s, self.total_dose, self.eng)

    print result

def VOX_mass(self):
    self.pix_size = \
        float(self.ds.header['scalingfactor(mm/pixel)[1]'][0]) * 0.1 #cm

```

```
#print 'self.pix_size', self.pix_size
self.vox_mass = self.pix_size**3 * self.rho * 0.001 #kg
#print 'self.vox_mass', self.vox_mass

def Energy(self):
    self.j2MeV = 6.24150636e12
    self.VOX_mass()
        #           cGy           Kg           MeV / j
    self.eng = (self.DoseImg * 0.01) * self.vox_mass * self.j2MeV #MeV
    self.eng = numpy.sum(self.eng * self.ds.image) #MeV

def absorbfraction(self):
    self.abfrac = self.eng / (self.number * self.energy)

def delta(self):
    self.delta = 1 * self.energy * 1.60217646e-13 #kg.Gy / Bq.s

def vox_mass_sphere(self):
    self.sphere_mass = numpy.sum((self.vox_mass * self.ds.image)) #kg

def specific_ab_frac(self):
    self.vox_mass_sphere()
    self.specAbFrac = self.abfrac / self.sphere_mass #1/kg

def S_value(self):
    self.specific_ab_frac()
    self.s = self.delta * self.specAbFrac #Gy

def sum_dose(self):
    self.total_dose = \
        numpy.sum(self.DoseImg * self.ds.image) * 0.01 #Gy
```

Appendix B

Absorbed Fractions

B.1 Simulated Values

Table B.1: Values for the absorbed fractions simulated in GATE.

Sphere mass (g)	Sphere radius (cm)	Gate v3.1.2	Gate v6 standard	Gate v6 Low energy	Gate v6 Penelope	Stabin
Energy: 0.03 MeV						
2	0.782	0.083	0.082	0.089	0.089	0.083
4	0.985	0.105	0.104	0.112	0.115	0.105
6	1.127	0.120	0.122	0.127	0.130	0.120
8	1.241	0.132	0.134	0.139	0.142	0.132
10	1.337	0.142	0.143	0.151	0.153	0.143
20	1.684	0.177	0.176	0.190	0.191	0.179
40	2.122	0.219	0.219	0.232	0.235	0.224
60	2.429	0.245	0.245	0.261	0.264	0.253
80	2.673	0.265	0.265	0.284	0.285	0.276
100	2.879	0.281	0.281	0.299	0.301	0.294
Energy: 0.04 MeV						
1	0.620	0.031	0.031	0.032	0.032	0.031
2	0.782	0.040	0.040	0.042	0.041	0.040
4	0.985	0.051	0.051	0.053	0.053	0.051

continued on next page

continued from previous page, Table B.1

Sphere mass (g)	Sphere radius (cm)	Gate v3.1.2	Gate v6 standard	Gate v6 Low energy	Gate v6 Penelope	Stabin
6	1.127	0.058	0.058	0.062	0.062	0.059
8	1.241	0.065	0.065	0.068	0.068	0.065
10	1.337	0.070	0.070	0.074	0.074	0.071
20	1.684	0.089	0.089	0.094	0.094	0.091
40	2.122	0.113	0.113	0.119	0.118	0.117
60	2.429	0.129	0.129	0.136	0.135	0.136
80	2.673	0.141	0.141	0.148	0.148	0.150
100	2.879	0.151	0.150	0.159	0.158	0.162
Energy: 0.06 MeV						
1	0.620	0.015	0.015	0.015	0.015	0.015
2	0.782	0.019	0.019	0.020	0.020	0.019
4	0.985	0.025	0.024	0.025	0.025	0.025
6	1.127	0.029	0.028	0.029	0.029	0.029
8	1.241	0.032	0.031	0.032	0.032	0.032
10	1.337	0.034	0.034	0.035	0.035	0.035
20	1.684	0.044	0.044	0.045	0.045	0.045
40	2.122	0.056	0.056	0.057	0.057	0.059
60	2.429	0.064	0.064	0.066	0.066	0.069
80	2.673	0.071	0.070	0.073	0.073	0.077
100	2.879	0.076	0.075	0.078	0.078	0.084
Energy: 0.08 MeV						
1	0.620	0.012	0.012	0.012	0.012	0.012
2	0.782	0.016	0.015	0.016	0.016	0.016
4	0.985	0.020	0.020	0.020	0.020	0.020
6	1.127	0.023	0.023	0.023	0.023	0.023
8	1.241	0.026	0.025	0.026	0.026	0.026
10	1.337	0.028	0.027	0.028	0.028	0.028
20	1.684	0.035	0.035	0.036	0.036	0.037
40	2.122	0.045	0.045	0.046	0.046	0.047
60	2.429	0.051	0.051	0.052	0.052	0.055
80	2.673	0.057	0.056	0.058	0.058	0.061
100	2.879	0.061	0.061	0.062	0.062	0.067
Energy: 0.10 MeV						
1	0.620	0.012	0.012	0.012	0.012	0.012
2	0.782	0.015	0.015	0.015	0.015	0.015
4	0.985	0.019	0.019	0.019	0.020	0.020

continued on next page

continued from previous page, Table B.1

Sphere mass (g)	Sphere radius (cm)	Gate v3.1.2	Gate v6 standard	Gate v6 Low energy	Gate v6 Penelope	Stabin
6	1.127	0.022	0.022	0.022	0.023	0.023
8	1.241	0.025	0.025	0.025	0.025	0.025
10	1.337	0.027	0.026	0.027	0.027	0.027
20	1.684	0.034	0.034	0.034	0.034	0.035
40	2.122	0.043	0.043	0.043	0.044	0.045
60	2.429	0.049	0.049	0.050	0.050	0.052
80	2.673	0.054	0.054	0.055	0.055	0.058
100	2.879	0.058	0.058	0.059	0.059	0.063
Energy: 0.14 MeV						
1	0.620	0.013	0.013	0.013	0.013	0.013
2	0.782	0.016	0.016	0.016	0.016	0.016
4	0.985	0.020	0.020	0.021	0.020	0.021
6	1.127	0.023	0.023	0.024	0.023	0.024
8	1.241	0.026	0.026	0.026	0.026	0.026
10	1.337	0.028	0.028	0.028	0.028	0.028
20	1.684	0.035	0.035	0.035	0.035	0.036
40	2.122	0.044	0.044	0.045	0.045	0.046
60	2.429	0.051	0.050	0.051	0.051	0.053
80	2.673	0.056	0.055	0.056	0.056	0.058
100	2.879	0.060	0.059	0.060	0.060	0.063
Energy: 0.364 MeV						
1	0.620	0.015	0.015	0.015	0.015	0.015
2	0.782	0.018	0.019	0.019	0.018	0.019
4	0.985	0.024	0.023	0.023	0.023	0.023
6	1.127	0.027	0.027	0.027	0.027	0.027
8	1.241	0.030	0.030	0.030	0.030	0.029
10	1.337	0.032	0.032	0.032	0.032	0.032
20	1.684	0.040	0.040	0.040	0.040	0.040
40	2.122	0.051	0.051	0.051	0.051	0.051
60	2.429	0.058	0.058	0.058	0.058	0.058
80	2.673	0.064	0.063	0.063	0.064	0.064
100	2.879	0.068	0.068	0.068	0.068	0.069
Energy: 0.662 MeV						
1	0.620	0.014	0.014	0.014	0.014	0.014
2	0.782	0.018	0.018	0.018	0.018	0.018
4	0.985	0.023	0.023	0.023	0.022	0.022

continued on next page

continued from previous page, Table B.1

Sphere mass (g)	Sphere radius (cm)	Gate v3.1.2	Gate v6 standard	Gate v6 Low energy	Gate v6 Penelope	Stabin
6	1.127	0.026	0.026	0.026	0.026	0.026
8	1.241	0.029	0.029	0.029	0.029	0.028
10	1.337	0.031	0.031	0.031	0.031	0.031
20	1.684	0.039	0.039	0.039	0.039	0.039
40	2.122	0.050	0.049	0.049	0.049	0.049
60	2.429	0.057	0.057	0.056	0.056	0.056
80	2.673	0.062	0.062	0.062	0.062	0.062
100	2.879	0.067	0.067	0.067	0.067	0.067
Energy: 1.460 MeV						
1	0.620	0.009	0.009	0.009	0.009	0.009
2	0.782	0.013	0.012	0.012	0.012	0.012
4	0.985	0.017	0.017	0.017	0.016	0.017
6	1.127	0.020	0.020	0.019	0.019	0.020
8	1.241	0.022	0.022	0.022	0.022	0.022
10	1.337	0.024	0.024	0.024	0.024	0.024
20	1.684	0.031	0.031	0.031	0.031	0.031
40	2.122	0.040	0.040	0.040	0.040	0.040
60	2.429	0.046	0.046	0.046	0.046	0.046
80	2.673	0.052	0.052	0.051	0.051	0.051
100	2.879	0.056	0.055	0.055	0.055	0.055
Energy: 2.750 MeV						
1	0.620	0.004	0.004	0.004	0.004	0.004
2	0.782	0.007	0.007	0.007	0.007	0.007
4	0.985	0.010	0.010	0.010	0.010	0.010
6	1.127	0.012	0.012	0.012	0.012	0.012
8	1.241	0.014	0.014	0.014	0.014	0.014
10	1.337	0.015	0.015	0.015	0.015	0.016
20	1.684	0.021	0.021	0.021	0.021	0.021
40	2.122	0.028	0.028	0.028	0.028	0.028
60	2.429	0.033	0.033	0.033	0.033	0.034
80	2.673	0.037	0.037	0.037	0.037	0.037
100	2.879	0.041	0.041	0.041	0.041	0.041

B.2 Normalised Values

Table B.2: Normalised values for the absorbed fractions simulated in GATE. Columns 3 to 6 are normalised to recommended values from Stabin. Column 7 are results from Stabin

Sphere mass (g)	Sphere radius (cm)	Gate3/ Stabin	Gate6 std/ Stabin	Gate6 low/ Stabin	Gate6 pen/ Stabin	EGS4/ MCNP
Energy: 0.03 MeV						
1	0.62	1.00	0.98	1.09	1.08	1.12
2	0.78	1.00	0.99	1.07	1.07	1.11
4	0.99	1.00	0.99	1.06	1.10	1.10
6	1.13	1.00	1.01	1.06	1.09	1.10
8	1.24	1.00	1.01	1.06	1.08	1.10
10	1.34	0.99	1.00	1.05	1.07	1.09
20	1.68	0.99	0.99	1.06	1.07	1.09
40	2.12	0.98	0.98	1.03	1.05	1.08
60	2.43	0.97	0.97	1.03	1.04	1.09
80	2.67	0.96	0.96	1.03	1.03	1.09
100	2.88	0.96	0.96	1.02	1.02	1.09
Energy: 0.04 MeV						
1	0.62	1.00	1.00	1.05	1.04	1.11
2	0.78	1.00	0.99	1.04	1.04	1.08
4	0.99	0.99	0.99	1.05	1.05	1.10
6	1.13	0.99	0.99	1.05	1.05	1.09
8	1.24	0.99	1.00	1.05	1.05	1.10
10	1.34	0.99	0.99	1.04	1.04	1.10
20	1.68	0.98	0.98	1.03	1.03	1.10
40	2.12	0.97	0.97	1.02	1.01	1.10
60	2.43	0.95	0.95	1.00	0.99	1.10
80	2.67	0.94	0.94	0.99	0.99	1.10
100	2.88	0.93	0.93	0.98	0.98	1.11
Energy: 0.06 MeV						
1	0.62	1.00	0.99	1.02	1.02	1.08
2	0.78	1.01	1.00	1.04	1.03	1.04
4	0.99	0.98	0.98	1.01	1.00	1.07
6	1.13	0.98	0.97	1.01	1.00	1.08

continued on next page

continued from previous page, Table B.2

Sphere mass (g)	Sphere radius (cm)	Gate3/ Stabin	Gate6 std/ Stabin	Gate6 low/ Stabin	Gate6 pen/ Stabin	EGS4/ MCNP
8	1.24	0.99	0.98	1.01	1.01	1.09
10	1.34	0.98	0.97	1.00	1.00	1.08
20	1.68	0.97	0.97	0.99	1.01	1.09
40	2.12	0.95	0.95	0.97	0.97	1.09
60	2.43	0.93	0.93	0.96	0.96	1.11
80	2.67	0.92	0.92	0.94	0.94	1.12
100	2.88	0.90	0.90	0.93	0.93	1.13
Energy: 0.08 MeV						
1	0.62	1.03	1.01	1.04	1.03	1.05
2	0.78	0.98	0.97	0.99	0.99	1.02
4	0.99	1.00	0.99	1.01	1.01	1.04
6	1.13	1.00	1.00	1.02	1.01	1.04
8	1.24	0.98	0.97	1.00	1.00	1.04
10	1.34	0.99	0.98	1.00	1.00	1.05
20	1.68	0.95	0.95	0.97	0.97	1.06
40	2.12	0.96	0.95	0.97	0.97	1.07
60	2.43	0.94	0.93	0.95	0.95	1.08
80	2.67	0.93	0.93	0.94	0.95	1.09
100	2.88	0.91	0.90	0.92	0.92	1.10
Energy: 0.10 MeV						
1	0.62	0.99	0.99	1.00	1.01	1.04
2	0.78	1.01	1.00	1.02	1.03	1.03
4	0.99	0.97	0.96	0.97	0.98	1.04
6	1.13	0.97	0.97	0.98	0.98	1.03
8	1.24	0.99	0.98	0.99	1.00	1.05
10	1.34	0.99	0.98	0.99	1.00	1.03
20	1.68	0.97	0.97	0.98	0.98	1.05
40	2.12	0.95	0.95	0.96	0.97	1.06
60	2.43	0.94	0.94	0.96	0.96	1.07
80	2.67	0.93	0.92	0.94	0.94	1.08
100	2.88	0.92	0.91	0.93	0.93	1.08
Energy: 0.14 MeV						
1	0.62	0.96	0.97	0.98	0.98	1.01
2	0.78	0.99	1.00	1.02	1.01	1.02
4	0.99	0.96	0.96	0.98	0.97	1.03
6	1.13	0.97	0.97	0.98	0.98	1.03

continued on next page

continued from previous page, Table B.2

Sphere mass (g)	Sphere radius (cm)	Gate3/ Stabin	Gate6 std/ Stabin	Gate6 low/ Stabin	Gate6 pen/ Stabin	EGS4/ MCNP
8	1.24	0.99	0.99	1.00	0.99	1.03
10	1.34	0.99	0.99	1.00	1.00	1.03
20	1.68	0.97	0.97	0.98	0.98	1.04
40	2.12	0.96	0.96	0.97	0.98	1.04
60	2.43	0.95	0.95	0.97	0.96	1.04
80	2.67	0.96	0.95	0.97	0.97	1.05
100	2.88	0.95	0.94	0.96	0.96	1.05

Energy: 0.364 MeV

1	0.62	0.97	0.99	0.98	0.97	1.02
2	0.78	0.97	0.98	0.98	0.97	1.01
4	0.99	1.03	1.02	1.01	1.02	1.02
6	1.13	1.00	1.00	0.99	1.00	1.03
8	1.24	1.03	1.02	1.02	1.02	1.02
10	1.34	1.00	1.00	1.00	0.99	1.02
20	1.68	1.01	1.01	1.01	1.01	1.02
40	2.12	1.00	0.99	1.00	0.99	1.03
60	2.43	1.00	0.99	1.00	0.99	1.02
80	2.67	0.99	0.99	0.99	0.99	1.02
100	2.88	0.99	0.98	0.99	0.99	1.03

Energy: 0.662 MeV

1	0.62	0.98	0.99	0.98	0.98	1.01
2	0.78	0.98	0.98	0.98	0.98	1.02
4	0.99	1.02	1.03	1.02	1.01	1.02
6	1.13	1.00	1.00	0.99	1.00	1.02
8	1.24	1.03	1.02	1.02	1.02	1.02
10	1.34	1.00	1.00	0.99	0.99	1.03
20	1.68	1.01	1.00	1.00	1.00	1.02
40	2.12	1.01	1.01	1.00	1.01	1.02
60	2.43	1.01	1.01	1.01	1.01	1.01
80	2.67	1.00	1.00	1.01	1.00	1.03
100	2.88	1.00	1.00	0.99	1.00	1.02

Energy: 1.460 MeV

1	0.62	1.02	1.02	1.01	1.02	1.04
2	0.78	1.05	1.04	1.03	1.03	1.05
4	0.99	0.98	0.98	0.97	0.97	1.04
6	1.13	0.98	0.98	0.97	0.97	1.03

continued on next page

continued from previous page, Table B.2

Sphere mass (g)	Sphere radius (cm)	Gate3/ Stabin	Gate6 std/ Stabin	Gate6 low/ Stabin	Gate6 pen/ Stabin	EGS4/ MCNP
8	1.24	1.00	0.99	0.98	0.99	1.03
10	1.34	1.00	0.99	0.98	0.99	1.03
20	1.68	1.00	1.01	0.99	1.00	1.05
40	2.12	1.00	1.00	1.00	0.99	1.03
60	2.43	1.01	1.01	1.00	0.99	1.01
80	2.67	1.01	1.01	1.00	1.00	1.02
100	2.88	1.01	1.01	1.00	1.00	1.01
Energy: 2.750 MeV						
1	0.62	1.11	1.12	1.09	1.10	1.09
2	0.78	0.96	0.95	0.94	0.95	1.04
4	0.99	0.98	0.97	0.97	0.97	1.05
6	1.13	1.01	1.00	1.00	1.01	0.98
8	1.24	0.99	0.98	0.98	0.99	1.05
10	1.34	0.96	0.95	0.94	0.96	1.03
20	1.68	1.00	0.99	1.00	1.00	1.01
40	2.12	1.02	1.01	1.00	1.01	1.02
60	2.43	0.98	0.97	0.98	0.98	1.02
80	2.67	1.01	1.01	1.01	1.01	1.01
100	2.88	1.00	0.99	0.99	1.00	1.01

Appendix C

Monte Carlo

C.1 Introduction

The following section describes the implementation of a very simple Monte Carlo approach that was developed to calculate absorbed dose fractions in the Medical Internal Radiation Dosimetry, spheres [22]. The accuracy of the code can not be compared to general Monte Carlo codes available as it makes a number of large assumptions. The aim of the development was not to reinvent the wheel but to investigate what possible problems the original values for the MIRDS spheres have.

The Monte Carlo program was written in python. Python is a general purpose high level programming code that is useful in rapid development projects. It has a large number of libraries and modules that are available. One problem with python compared to other high level object orientated programming languages such as C++ is it's lack of speed. The availability of high performance numerical libraries such as numpy and scipy do however reduce this limitation.

C.2 Application Assumptions

This code is applicable to a homogeneous medium for the transport of photon energies between 10 keV to 1.020 MeV. These energies have been chosen so that only Compton and photoelectric interactions are taken into account. The use of a homogeneous medium (in this case tissue) has also been chosen to simplify simulation so that a boundary cross algorithm is not required.

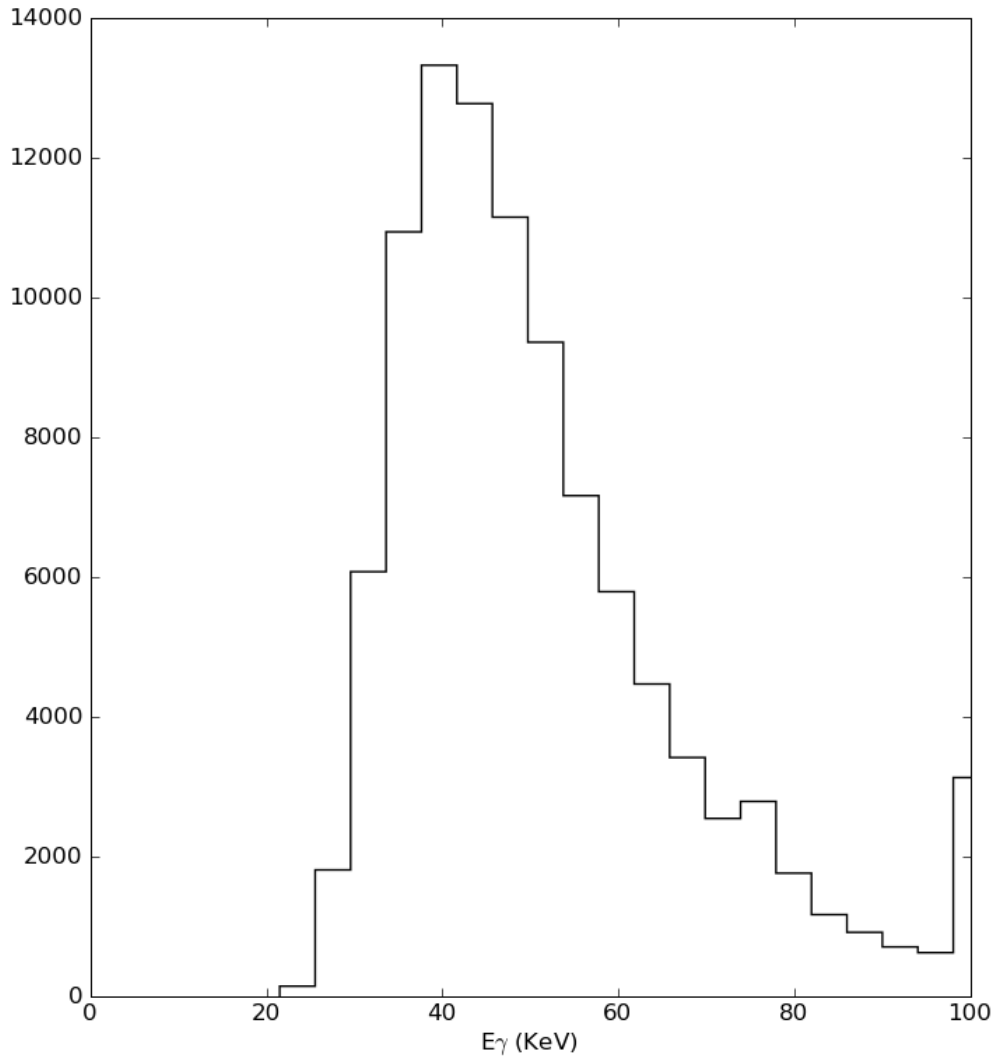
A 10 keV finite energy cut for Compton interaction has been chosen due to the amount of energy lost from Compton scattering at such a low energy. The results of this assumption do not significantly effect the results of the simulation due to the large increase in probability of photoelectric absorption at low energies. This increase in probability is shown in Table C.2 where the ratio of photoelectric to incoherent scattering cross sections increases at low energies. To prove that no increased bias is introduced into the calculations, a simulation of a point source in a semi infinite ¹ tissue medium was performed with a cut value of 1 keV. An initial photon energy of 100 keV was used with 10^5 photons being generated. A histogram of the energy of the initial photon prior to interaction with the medium is shown in Figure C.1. It can be seen that the number of photons that undergo Compton scattering below 10 keV is negligible.

An additional assumption used is that coherent scatter is not modelled. From Table C.3 it can be seen that the effect of coherent scattering is non-negligible at around 30 keV. At higher and lower energies the incoherent and photoelectric cross sections are dominant. Figure C.1 shows that 95% of all photons are absorbed before they fall below 30 keV. Therefore the overall effect of negating coherent scattering may introduce a very small bias towards an increase in the total absorbed fraction.

The final assumption used was that energy is absorbed to a point i.e. when a photon transfers kinetic energy to an electron the energy is assumed to be absorbed

¹The medium size is a total of 12 mean free path lengths. For the MIRD tissue this is approximately 74 cm for 100 keV photons.

Figure C.1: Histogram of scattered radiation in a semi infinite tissue medium using the python Monte Carlo code.



at that point. In reality however energy is absorbed in a region not a point. The size of this energy absorption region is about the mean free path of the electron. For the MIRD tissue this is approximately 0.12 mm for electrons with a kinetic energy of 1 MeV [89]. For a very simple approach this assumption is by far the most important, however this advantage may introduce an additional bias. On one hand calculations are simplified by not simulating electron transport. Where on the other hand the

accuracy is effected by not simulating electrons escaping the region or the production of bremsstrahlung.

C.3 Description

A flow chart diagram of the code is shown in Figure C.2. A gamma photon of some initial energy E_γ is generated at a point with the original cartesian coordinates of $X=Y=Z=0$. The photon is tracked to a point where the type of interaction is found. The process is repeated until the photon is completely absorbed, or has fallen below an energy cut off in which it is absorbed or leaves the world volume.

C.3.1 Random numbers

One very important consideration when using a Monte Carlo method is the generation of random numbers. In reality the numbers used are not exactly random and will after some time repeat. This application uses the pseudo-random number module *random* which is included with the standard python code distribution. The module uses the Mersenne Twister as the core generator. The module is suitable for this Monte Carlo application as it has a large number generation before the sequence is repeated. For the 32 bit variant the Mersenne Twister has a prime period of $2^{19937} - 1$ [145].

The total number of random numbers generated to track a single photon varies, but in general each sequence has a fixed amount. When the process begins three random numbers are generated. Of these, two indicate the initial direction ($0 \leq \alpha \leq \pi$ and $0 \leq \beta \leq 2\pi$) and the third is used to find the path length (Section C.3.3). Each time the path length is sampled a new random number is generated. A fourth is generated to find the interaction type i.e. Compton or photoelectric. If a Compton event is simulated a minimum of four random numbers are generated. The sampling

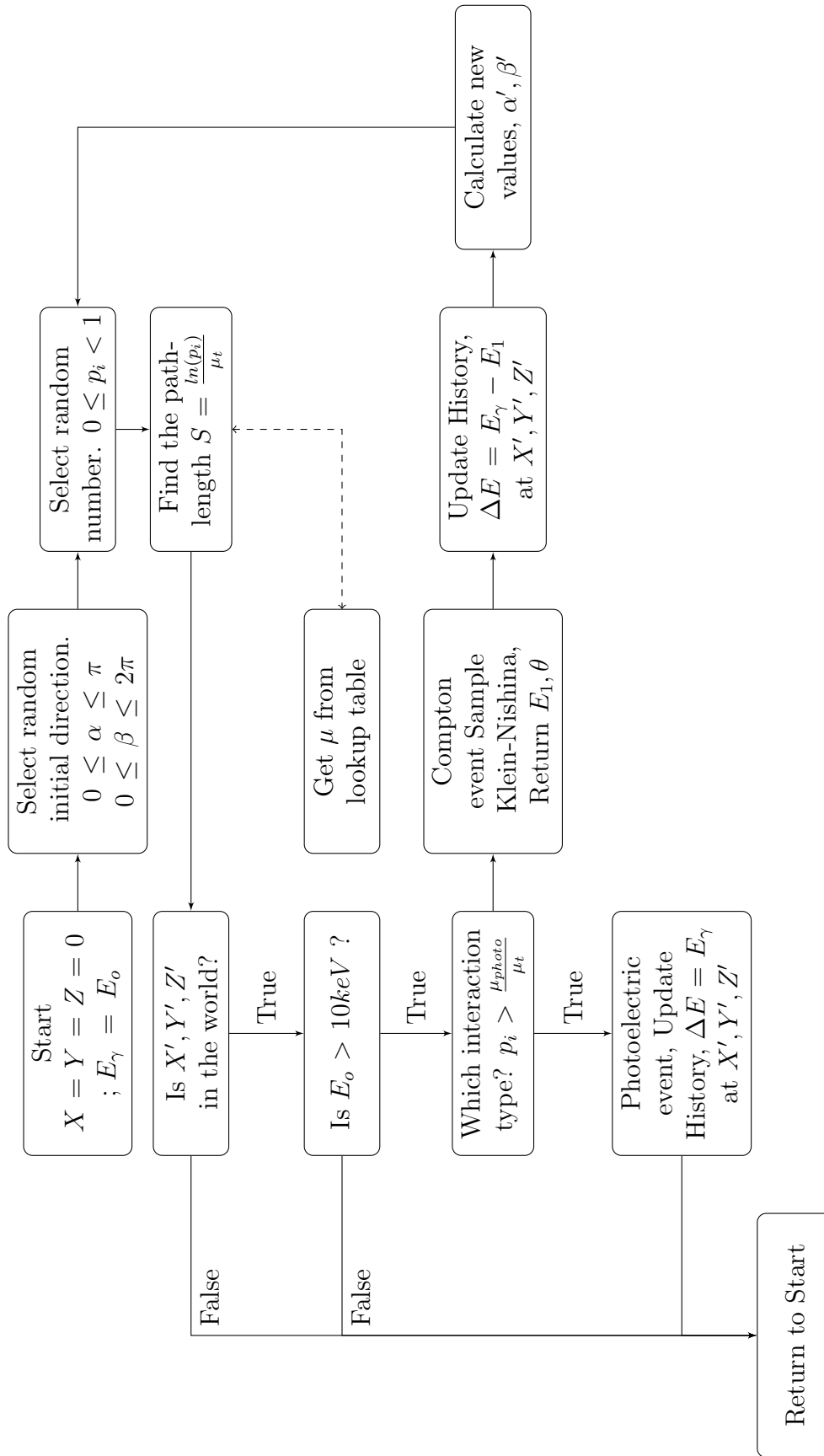


Figure C.2: Diagram for a python based Monte Carlo code for gamma photons. The function used and what it returns is located below the description steps.

Table C.1: Tissue composition used in the MIRD pamphlets[21]

Element	Fraction of mass %
Oxygen	71.39
Carbon	14.89
Hydrogen	10.00
Nitrogen	3.47
Sodium	0.15
Chlorine	0.10

of the Klein-Nishina formula is explained in Section C.3.5.

C.3.2 Tissue cross sections

In the MIRD pamphlets 3 and 8, absorbed fractions are calculated for a composition of tissue shown in Table C.1. This definition for tissue is different from that described by the ICRU report No. 44 [146]. Stabin and Konijnenberg [1] do state however that this composition and those used by others should not provide much of a difference to the absorbed fraction result.

Cross section values were obtained from the NIST:XCOM Database [147]. Values were placed into an array for lookup when necessary. Table C.2 shows selected values for the photoelectric (τ), coherent (σ_{coh}) and incoherent (σ_{icoh}) cross sections as well as the ratio of photoelectric to incoherent scattering cross sections. Table C.3 shows the total cross section with and with out coherent scattering. The ratios are also shown for comparison.

C.3.3 Path length

The path length is found by sampling the probability function for photon interaction (equation C.1).

$$p(x) = \mu_T e^{-\mu_T x} \quad (C.1)$$

Table C.2: Cross-sections obtained from the XCOM database for the tissue composition used in the MIRD pamphlets.

Energy keV	Coherent Scatter (σ_{coh}) cm ² /g	Incoherent Scatter (σ_{icoh}) cm ² /g	Photoelectric (τ) cm ² /g	Ratio $\frac{\tau}{\tau+\sigma_{icoh}}$
10	2.18E-01	1.53E-01	4.49E+00	0.968
30	4.45E-02	1.81E-01	1.32E-01	0.422
60	1.32E-02	1.75E-01	1.35E-02	0.071
100	5.06E-03	1.61E-01	2.50E-03	0.015
200	1.31E-03	1.34E-01	2.62E-04	0.002
500	2.12E-04	9.56E-02	1.71E-05	0.000

Table C.3: Total cross-sections obtained from the XCOM database for the tissue composition used in the MIRD pamphlets.

Energy keV	With Coherent Scatter cm ² /g	Without Coherent Scatter cm ² /g	Ratio
10	4.86E+00	4.64E+00	0.955
30	3.58E-01	3.13E-01	0.874
60	2.02E-01	1.89E-01	0.936
100	1.68E-01	1.63E-01	0.970
200	1.35E-01	1.34E-01	0.993
500	9.58E-02	9.56E-02	0.998

Here the value μ_T is the total attenuation coefficient and is provided from a lookup table created from the XCOM database [147]. Compton and photoelectric cross sections are also obtained from the look up table when the total attenuation coefficient is found. The probability that the photon will travel a distance S or less is then given by equation C.2. If the probability $p(x)$ is substituted to be a random number p_i then the distance traveled is found by the following.

$$S = \frac{1}{\mu_T} \ln(p_i) \quad (\text{C.2})$$

C.3.4 Interaction type

As stated in Section C.2, only Compton and photoelectric photon interactions are taken into account. The type of interaction is found by the ratio of the photoelectric cross-section over the addition of the photoelectric and Compton cross-sections. A random number is generated and if this value is less than the ratio, a photoelectric event is chosen. Values for this ratio in the MIRD tissue are shown in Table C.2. For example in this application a photon with an energy of 30 keV has a 42.2% probability of a photoelectric event occurring.

C.3.5 Sampling the Klein-Nishina distribution

Once a Compton event is found to occur the direction and energy of the scattered photon is required. This is found by using a combined composition and rejection approach [148]. With some work the Compton cross section may be written as a suitable probability density function (PDF) [149] of the ratio of the initial (E_0) and final (E_1) photon energies such that $\epsilon = \frac{E_1}{E_0}$ (This value is sometimes called the wavelength, however the value is dimensionless). For any photon the minimum scattered photon energy will occur from backscatter and is written in equation C.3. For sampling the energy the respective PDF is given by equation C.4. Equation C.4,

is also used in the standard Geant4 electromagnetic physics package [150]. Other methods for sampling from the Klein-Nishina distribution are discussed by Horowitz et. al.[151], Blomquist and Gelbard [152] and Kahn (discussed in [149]).

$$\epsilon_0 = \frac{m_e c^2}{m_e c^2 + 2E_0} \quad (\text{C.3})$$

$$PDF = f(\epsilon) \cdot g(\epsilon) = [\alpha_1 f_1(\epsilon) + \alpha_2 f_2(\epsilon)] \cdot g(\epsilon) \quad (\text{C.4})$$

where, the PDFs f_1 and f_2 are defined on the interval $[\epsilon_0, 1]$:

$$f_1(\epsilon) = \frac{1}{\alpha_1 \epsilon} \quad ; \quad \alpha_1 = \ln\left(\frac{1}{\epsilon_0}\right) \quad (\text{C.5})$$

$$f_2(\epsilon) = \frac{\epsilon}{\alpha_2} \quad ; \quad \alpha_2 = \frac{1 - \epsilon_0^2}{2} \quad (\text{C.6})$$

and where $g(\epsilon)$ is the rejection function;

$$g(\epsilon) = \left[1 - \frac{\epsilon}{1 + \epsilon^2} \sin^2 \theta\right] \quad (\text{C.7})$$

The application of these equations is shown in the flow diagram C.3. Here the back scatter ratio (Equation C.3) is calculated with it's respective positive constants α_1 and α_2 . From the ratio of $\frac{\alpha_1}{\alpha_1 + \alpha_2}$ a test variate for ϵ is sampled from f_1 or f_2 using the cumulative distribution method for continuous variables [153]. The associated test value for the scattering angle θ is then found by the Compton equation. Finally $g(\epsilon)$ is calculated and using the rejection method [153] the test value ϵ is accepted or rejected.

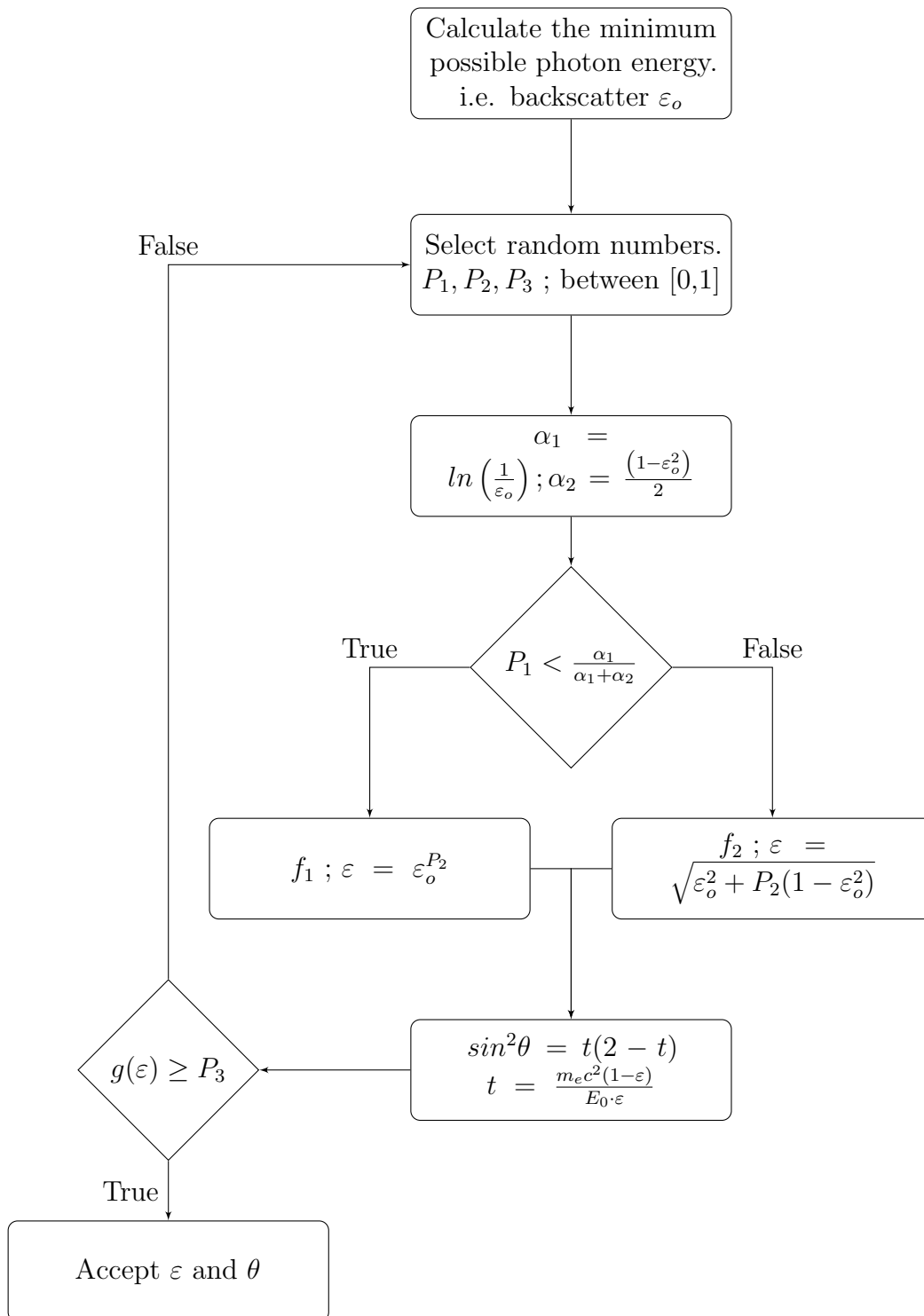


Figure C.3: A Logic diagram for direction and energy change from Compton scattering

C.4 Code

The following are the user classes (track.py) for the Monte Carlo application described above and a command line application for the MIRD spheres.

C.4.1 User classes

```
#!/usr/bin/python
"""
Name: track.py

Description:
    The following is a group of user classes for the implementation
    of a very simple Monte Carlo approach to calculate absorbed
    dose fraction in the Medical Internal Radiation Dosimetry,
    spheres.

Aim:
    The aim of the development was not to reinvent the wheel but to
    investigate what possible problems the original values have.

Limitations:
    a lack of speed,
    homogeneous medium only,
    photon energies between 1.020 MeV to 10 keV,
    Compton and photoelectric interactions only, and
    electron transport is not simulated.

KJH, June - 2010
"""

__author__ = "Kevin J Hickson"
__email__ = "kevin.hickson@petnm.unimelb.edu.au"
__version__ = 0.01

import sys
import math

import random
random.seed()

import numpy
```

```
import pylab

try:
    #The psyco module attempts to pre-compile the code
    #i.e. reducing simulation time, but not by much!
    import psyco
    psyco.full()
except ImportError:
    print ""
    Psyco not installed program may run slow.
    ""

class geometry:
    """This class handles the world geometry, including
    the geometry of the sphere source. A voxel map is implemented
    but not used or tested.
    """
    def __init__(self):
        """__init__ is passed with no effect"""
        pass
    def new_world(self, world_size_x, world_size_y, world_size_z):
        """Create a new voxel world for absorbed dose scoring.
        [Not used]"""
        self.world_size = (world_size_x, world_size_y, world_size_z)
        self.the_world = the_world = self.world((world_size_x,
                                                  world_size_y, world_size_z))
        self.world_centre = (world_size_x/2., world_size_y/2.,
                             world_size_z/2.)
        return the_world

    def world(self, world_size):
        """Called in geometry.new_world [Not used]"""
        size = world_size[0] * world_size[1] * world_size[2]
        array = numpy.zeros(size, dtype = numpy.float32)
        return array.reshape(world_size)

    def cart2sph(self, x, y, z):
        """From Cartesian to Spherical coordinates"""
        #input must be float
        r = math.sqrt(x**2 + y**2 + z**2)
        theta = math.acos(z / r)
        phi = math.atan2(y, x)
        return r, theta, phi

    def sph2cart(self, r, theta, phi):
```

```

    """From Spherical to Cartesian coordinates"""
    # r >= 0
    # 0 <= theta <= pi
    # 0 <= phi < 2pi
    x = r * math.sin(theta) * math.cos(phi)
    y = r * math.sin(theta) * math.sin(phi)
    z = r * math.cos(theta)
    return x, y, z

def sphere_source(self, r):
    """Get a random point (Cartesian coords.)
    in a sphere source. """
    R = random.uniform(0, r)
    theta = random.uniform(0, math.pi)
    phi = random.uniform(0, 2 * math.pi)

    return self.sph2cart(R, theta, phi)

class attenuation_data:
    """Read and use attenuation data from NIST"""
    def __init__(self, numpy_attn_file):
        """
        File columns are as follows.
        Photon Coherent Incoher. Photoel. Tot. w/ Tot. wo/
        Energy Scatter. Scatter. Absorb. Coherent Coherent
        Mev cm^2/g cm^2/g cm^2/g cm^2/g cm^2/g
        """
        #Load numpy binary file.
        self.attn_file = numpy.load(numpy_attn_file)

    def material_names(self):
        """Return the names of each material in
        the numpy attenuation file."""
        return self.attn_file.files

    def get_attn_data(self, name):
        """Return the lookup table for a given material name."""
        return numpy.array(self.attn_file[name],
                           dtype = numpy.float32)

    def get_water(self):
        """Used for testing, returns the water lookup table."""
        self.h2o_attn = h2o_attn = self.get_attn_data('h2o')
        #since density = 1.00 g/cm^3 column [1:] is

```



```

#also in units of cm-1.
#however for anything other than p = 1.00 g/cm3
#p needs to be taken into account.
return h2o_attn

def lookup(self, atn_data, energy):
    """Returns the energy, coherent, incoherent, photo and
    total cross sections from the table atn_data by looking
    up the energy."""

    #use to get closest value
    bool = atn_data[0] == round(energy,3)
    i = numpy.where(bool)

    #Used to check that one and only one energy value has
    #been found, If this is incorrect then there is a problem
    #with the numpy attenuation table.
    if len(i[0]) != 1:
        print 'Debug attn Library, E:%s, i:%s' % (energy,i)

    values = atn_data[0][i][0], atn_data[1][i][0], \
             atn_data[2][i][0], atn_data[3][i][0], \
             atn_data[4][i][0]
    #energy, coherent, incoherent, photo, total
    return values

class histories:
    """Store interaction histories in a way that will make them
    easy to save"""
    def __init__(self, base_name):
        """Opens a history text file. and starts a numpy array
        to keep energy values but not location or type."""
        self.hist = open(base_name, 'w')
        self.abfrac = numpy.array([])

    def write(self, string):
        """Write to the history file."""
        self.hist.write(string + '\n')

    def absorbed_fraction(self, energy):
        """Append energy to the numpy array."""
        self.abfrac = numpy.append(self.abfrac, energy)

class event:
    """Simulate a single event"""
    def __init__(self, event_number, histories, energy0,\

```

```

        x0, y0, z0, world_size, mu_data,\
        material_name, vox = False, savehits=False):
    """Set initial location and energy values and follow event
    until it is terminated
    note: mu in terms of mu = (mu_total, mu_photo, mu_compton)
    """
    self.energy0 = energy0 #MeV
    self.x0 = x0           #cm
    self.y0 = y0           #cm
    self.z0 = z0           #cm
    self.mu_data = mu_data
    self.world = world_size
    self.savehits = savehits #True or False

    self.electron_rest_mass = 0.511 #MeV / c^2

    #Start Main
    self.main(histories, event_number, material_name, vox = vox)

def initial_random_numbers(self):
    """Create the initial random direction in spherical
    coordinates

    0 <= alpha <= pi
    0 <= beta <= 2pi
    """
    #So 1.0 is possible random.uniform is used.
    self.alpha = math.pi * random.uniform(0.0, 1.0)
    self.beta = 2 * math.pi * random.uniform(0.0, 1.0)

def get_flight_distance(self, mu_total):
    """sampling the probability function for photon interaction
    and return a random distance before interaction"""
    p = random.uniform(0., 1.0)
    return -math.log(p) * (1.0 / mu_total) #unit =f mu

def test_event_type(self, mu):
    """Find the event at the interaction location.
    Return Compton or photoelectric only."""
    p = random.uniform(0,1)
    if p < (mu[3]/(mu[3] + mu[2])):return "photoelectric"
    else: return "compton"

    #with coherent scatter the test would look like this.
    """
    if p < (mu[3]/mu[4]):return "photoelectric"

```

```

elif p < ((mu[3] + mu[2]) / mu[4]): return "compton"
elif p < ((mu[3] + mu[2] + mu[1]) / mu[4]):
    return "coherent"
else: return "pair_production 'What the!!!!'"
"""

def new_position(self, S, alpha, beta):
    """Return the new photon location after finding the
    flight distance. Note: Spherical coordinates in,
    Cartesian coordinate out.
    """
    x1, y1, z1 = geometry().sph2cart(S, alpha, beta)
    X = self.x0 + x1
    Y = self.y0 + y1
    Z = self.z0 + z1

    return X, Y, Z

def g4_sample(self):
    """This is g4's combined composition and rejection method
    to sample the energy of a scattered photon.

    It takes a lot of work to recast the Compton cross section
    as a function of E0 and E1 into a suitable
    PDF(e) = f(e).g(e) = [alpha1*f1(e) + alpha2*f2(e)].g(e)
    where e = E1/E0.

    Based on Nelson et al. 1985 (EGS4)
    """

    epsilon_0 = self.electron_rest_mass /
                (self.electron_rest_mass\
                 + (2 * self.energy0))
    #Where epsilon_0 is the minimum possible photon energy
    #i.e. back scatter

    john_west = True #It's the fish that john west rejects
                    #that makes john west the best.

    while john_west:
        p = random.uniform(0.0, 1.0)
        p1 = random.uniform(0.0, 1.0)
        p2 = random.uniform(0.0, 1.0)

        alpha_1 = math.log(1/epsilon_0)
        alpha_2 = 0.5 * (1- (epsilon_0**2))

```

```

    if p < (alpha_1 / (alpha_1 + alpha_2)):
        #sample f1(e)
        epsilon = epsilon_0 ** p1
    else:
        #sample f2(e)
        epsilon = \
            math.sqrt( epsilon_0**2 + p1 * \
                       (1 - epsilon_0**2))
    #From Compton formula
    t = self.electron_rest_mass * (1 - epsilon) / \
        (self.energy0*epsilon)
    sin2 = t*(2-t)

    if 1 - ((epsilon / (1 + epsilon**2))*sin2) >= p2:
        #Accept epsilon
        john_west = False
    else:
        john_west = True

    E1 = self.energy0 * epsilon
    angle = math.acos((1 + \
                      (self.electron_rest_mass/self.energy0) \
                      - (self.electron_rest_mass/E1)))

    return (E1, angle)

def alpha_beta_new(self):
    """Return the new photon direction from the Compton
    scattering angle and a random Azimuth angle.
    """
    self.alpha = alpha = self.scaterAngle
    self.beta = beta = 2 * math.pi * random.uniform(0.0, 1.0)
    return alpha, beta

def main(self, histories, event_number, material_name,
        vox = False):
    """Track a photon until it is absorbed, falls below cut
    off or leaves the world.
    """
    savehits = self.savehits
    material = self.mu_data.get_attn_data(material_name)
    h = histories
    self.initial_random_numbers()
    event = True
    while event:

```

```

mu = self.mu_data.lookup(material, self.energy0)

S = self.get_flight_distance(mu[2]+ mu[3])
self.x1, self.y1, self.z1 = \
    self.new_position(S, self.alpha, self.beta)

#Test if the event is in the world.
#Note the world is a sphere.
if (self.x1 **2 + self.y1 **2 + self.z1 **2) > \
    self.world**2:
    #event out of world
    event = False
else:
    #Test for the cut off value (This case is 10 keV).
    if self.energy0 < 0.010:
        if savehits:
            #Write event to file if asked.
            string = str(\
                '%s %s %s %s %s %s %s %s %s photoelectric'%\
                (event_number, self.energy0, self.energy0,\
                 self.x0, self.y0, self.z0, self.x1, \
                 self.y1, self.z1))
            h.write(string)
        else:
            #else append to the numpy array
            h.absorbed_fraction(self.energy0)
        event = False    #Stop the event.
    else:
        test = self.test_event_type(mu)
        if test == 'photoelectric':
            #Do the scoring for the photoelectric event.
            if savehits:
                string = str(\
                    '%s %s %s %s %s %s %s %s %s photoelectric'\
                    % (event_number, self.energy0,\
                     self.energy0,\
                     self.x0, self.y0, self.z0, self.x1, \
                     self.y1, self.z1))
                h.write(string)
            else:
                h.absorbed_fraction(self.energy0)
            event = False    #Stop event
        elif test == 'compton':
            #Get scatter angle and energy.
            self.energy1, self.scaterAngle = \
                self.g4_sample()

```


C.4.2 Command line parser

```
#!/usr/bin/python
"""
Name: absorbed_fractions.py

Usage: absorbed_fractions.py [options] sphere_radius i_energy(MeV)

Options:
  -h, --help          show this help message and exit
  -d, --debug         set debug option true.
  -a ATTN             A file containing cross section data.
                    Default: attn_data.npz
  -m MATERIAL_NAME   Choose the world material.
                    Default: h2o
  -o ONAME            Set the output histories name.
                    Default: testHits.dat
  -e TOTAL_EVENTS    Set the number of events to track.
                    Default: 10
  -s, --save         Write hits to a file

Description:
  Use the classes defined in track.py to obtain absorbed fraction for
  the MIRD spheres.

  This is ultimately a option parser program for my application.

  The output file is of the form.
  Line 1 (Header):
    sphere_radius(cm), initial_photon_energy(MeV),
    no._events, materal_name.
  Line 2 -> (Data):
    arg[0]           ; Event ID,
    arg[1]           ; Incident photon energy(MeV)
    arg[2]           ; Deposited energy(MeV)
    arg[3] - arg[5] ; Photon origin X, Y, Z
    arg[6] - arg[8] ; Energy Deposited at X, Y, Z
    arg[9]           ; Type of interaction.

KJH - June 2010
"""

__author__ = "Kevin J Hickson"
__email__ = "kevin.hickson@petnm.unimelb.edu.au"
__version__ = 0.01
```

```
import sys
import os
import optparse

import numpy
import track

def main(sphere_radius, initial_energy, number_of_events,
        oname, attn_file, material_name, savehits):
    """Begin the main application"""

    #Call __init__ on the histories class.
    #Sets scoring output.
    histories = track.histories(oname)

    if savehits:
        #Write a header for the output file.
        header = 'sphere_radius: %s initial_energy:' \
                '%s number_of_events:' \
                '%s material_name: %s' \
                % (sphere_radius, initial_energy, number_of_events,
                   material_name)

        histories.write(header)

    #Set the cross section lookup table
    xsection_data_file = track.attenuation_data(attn_file)

    event_number = 1
    world_size = sphere_radius

    while event_number <= number_of_events:
        Ox, Oy, Oz = track.geometry().sphere_source(sphere_radius)
        #Randomly get a point in the sphere to set
        #the org. photon points. Ox, Oy, Oz

        track.event(event_number, histories, initial_energy, \
                   Ox, Oy, Oz,
                   world_size, xsection_data_file, material_name,
                   savehits)
        #Calles an event, and follows it until
        #The event is False.
        event_number = event_number + 1
```



```

if savehits == False:
    #If no output file is selected,
    #absorbed energies have been binned
    #in a Numpy array. Useful for a large number of generated
    #photons.
    print 'Absorbed Fraction:%s, No. int%s, r:%s, e:%s' % \
          ((numpy.sum(histories.abfrac) / \
            (initial_energy*number_of_events)), \
            len(histories.abfrac),\
            sphere_radius, initial_energy)

if __name__ == '__main__':
    #The parser for command line use.
    parser = optparse.OptionParser(usage = \
        '%prog [options] sphere_radius initial_energy(MeV)',
        epilog = ('Problems to: %s\n' % __email__))

    #Add parser options.
    parser.add_option('-d', '--debug',
        dest= 'debug',
        default = False,
        action = 'store_true',
        help = '''set debug option true.''' )

    parser.add_option('-a', # '--attenuation_data',
        dest= 'attn',
        default = 'attn_data.npz',
        action = 'store',
        help=\
        '''A file containing cross section data.\
        Default: attn_data.npz''')

    parser.add_option('-m', # '--material_name',
        dest= 'material_name',
        default = 'h2o',
        action = 'store',
        help = '''Choose the world material.\
        Default: h2o''')

    parser.add_option('-o', # '--output_name',
        dest= 'oname',
        default = 'testHits.dat',
        action = 'store',
        help = \

```

```

        '''Set the output histories name.\
            Default: testHits.dat''')

parser.add_option('-e', # '--number of events',
                  dest= 'total_events',
                  default = '10',
                  action = 'store',
                  help = \
        '''Set the number of events to track.\
            Default: 10''')

parser.add_option('-s', '--save',
                  dest= 'save_events',
                  default = False,
                  action = 'store_true',
                  help = '''Write hits to a file''')

(options, args) = parser.parse_args()

#Check arguments
if len(args) != 2:
    print "Incorrect number of arguments\n"
    parser.print_help()
    sys.exit(1)

#The track.py script is limited to an energy of less
#than 1.022 MeV.

#Check this is true.
if float(args[1]) >= 1.022:
    print "Sorry photon energy can not be equal"
    print "to or above 1.022 MeV."
    sys.exit(1)

#We don't won't to save over the hits file, Check it.
if options.save_events:
    if os.access(options.ename, os.F_OK):
        print '%s already exists\nUse option: -o output_name' \
            % options.ename
        sys.exit(1)

main(float(args[0]), float(args[1]), int(options.total_events),
     options.ename, options.attn, options.material_name,
     options.save_events)

```

Bibliography

- [1] M. Stabin and M. Konijnenberg, “Re-evaluation of absorbed fractions for photons and electrons in spheres of various sizes,” *Journal of Nuclear Medicine*, vol. 41, pp. 149–160, 2000.
- [2] W. C. Eckelman, *PET in Drug Discovery and Development*. Springer, 2004, ch. 48, pp. 815–828.
- [3] D. R. Fisher, S. Shen, and R. F. Meredith, “Mird dose estimate report no. 20: Radiation absorbed-dose estimates for 111in- and 90y-ibritumomab tiuxetan,” *Journal of Nuclear Medicine*, vol. 50, pp. 644–652, 2009.
- [4] M. T. Hays, E. E. Watson, S. R. Thomas, and M. Stabin, “Mird dose estimate report 19: Radiation absorbed dose estimates from 18f-fdg.” *Journal of Nuclear Medicine*, vol. 43, pp. 210–214, 2002.
- [5] S. Mattsson, “Radiation dose to patients from radiopharmaceuticals addendum 3 to icrp publication 53 icrp publication 106,” ICRP, Tech. Rep., 2008.
- [6] M. G. Stabin, *Fundamentals of Nuclear Medicine Dosimetry*. Springer, 2008.
- [7] M. Cristy and K. Eckerman, “Specific absorbed fractions of energy at various ages from internal photon sources. vii. adult male,” Oak Ridge National Laboratory, Tech. Rep., 1987.
- [8] G. Zubal, C. Harrell, E. Smith, Z. Ratner, G. Gindi, and P. Hoffer, “Computerized three-dimensional segmented human anatomy,” *Medical Physics*, vol. 21, pp. 299–302, 1994.
- [9] W. P. Segars, “Development and application of the new dynamic nurbs-based cardiac-torso (ncat) phantom.” Ph.D. dissertation, Department of Biomedical Engineering, University of North Carolina, 2001.
- [10] S. Agostinelli, J. Allison, K. Amako, J. Apostolakis, H. Araujo, P. Arce, M. Asai, D. Axen, S. Banerjee, G. Barrand *et al.*, “Geant4-a simulation toolkit,” *Nuclear Instruments and Methods in Physics Research-Section A Only*, vol. 506, no. 3, pp. 250–303, 2003.
- [11] S. Jan, G. Santin, D. Strul, S. Staelens, K. Assié, D. Autret, S. Avner, R. Barbier, M. Bardies, P. M. Bloomfield *et al.*, “Gate: a simulation toolkit for pet and spect,” *Physics in Medicine and Biology*, vol. 49, pp. 4543–4561, 2004.

-
- [12] W. Segars and B. Tsui, "Mcat to xcat: The evolution of 4-d computerized phantoms for imaging research," *Proceedings of the IEEE*, vol. 97, no. 12, pp. 1954–1968, 2009.
- [13] D. Smith, "Fundamental quantities and units for ionizing radiation." International Commission on Radiation Units and Measurements, Tech. Rep., 1998.
- [14] H. O. Wyckoff, A. Allisy, and K. Liden, "Correspondence: The new special names of si units in the field of ionizing radiations," *Physics in Medicine and Biology*, vol. 20, p. 1029, 1975.
- [15] J. C. P. Heggie, N. A. Liddell, and K. P. Maher, *Applied Imaging Technology*, 4th ed. St Vincent's Hospital, Melbourne, 2001.
- [16] J. Valentin, "The 2007 recommendations of the international commission on radiological protection, publication 103," ICRP, Tech. Rep., 2007.
- [17] W. A. Jennings, "When did you last see your rontgen? – the si units and their use," *Physics in Medicine and Biology*, vol. 29, no. 2, pp. 131–137, 1984.
- [18] J. Valentin, "Icrp publication 92: Relative biological effectiveness (rbe), quality factor (q), and radiation weighting factor (wr)," ICRP, Tech. Rep., 2003.
- [19] H. Cember and T. E. Johnson, *Introduction to Health Physics*, 4th ed. McGraw–Hill, 2009.
- [20] H. E. Johns and J. R. Cunningham, *The Physics of Radiology*, 4th ed. Charles C Thomas Publisher, 1983.
- [21] G. Brownell, W. Ellett, and R. Reddy, "Absorbed fractions for photon dosimetry. mird pamphlet no. 3," Society of Nuclear Medicine, Tech. Rep., 1968.
- [22] W. Ellett and R. Humes, "Absorbed fractions for small volumes containing photon emitting radioactivity. mird pamphlet no. 8," Society of Nuclear Medicine, Tech. Rep., 1972.
- [23] R. Howell, "The mird schema: from organ to cellular dimensions," *Journal of Nuclear Medicine*, vol. 35, no. 3, p. 531, 1994.
- [24] S. Goddu and T. Budinger, *MIRD Cellular S. Values: Self-absorbed Dose Per Unit Cumulated Activity for Selected Radionuclides and Monoenergetic Electron and Alpha Particle Emitters Incorporated Into Different Cell Compartments*. Society of Nuclear Medicine Reston, VA, 1997.
- [25] W. Bolch, L. Bouchet, J. Robertson, B. Wessels, J. Siegel, R. Howell, A. Erdi, B. Aydogan, S. Costes, E. Watson *et al.*, "Mird pamphlet no. 17: The dosimetry of nonuniform activity distributions–radionuclide s values at the voxel level," *Journal of Nuclear Medicine*, vol. 40, no. 1, p. 11S, 1999.

-
- [26] M. Stabin, J. Siegel, J. Hunt, R. Sparks, J. Lipsztein, and K. Eckerman, "Radar—the radiation dose assessment resource. an online source of dose information for nuclear medicine and occupational radiation safety," *Journal of Nuclear Medicine*, vol. 42, p. 243, 2001.
- [27] M. Stabin and L. da Luz, "Decay data for internal and external dose assessment," *Health physics*, vol. 83, no. 4, p. 471, 2002.
- [28] T. W. Burrows, "Nuclear decay data in the mird format," February 2011. [Online]. Available: <http://www.nndc.bnl.gov/mird/>
- [29] J. Chang, "Table of nuclides," 2000. [Online]. Available: <http://atom.kaeri.re.kr/>
- [30] W. Snyder, M. Ford, and G. Warner, "Revision of mird pamphlet no. 5 entitled" estimates of absorbed fractions for monoenergetic photon sources uniformly distributed in various organs of a heterogeneous phantom", " Oak Ridge National Lab., Tenn.(USA), Tech. Rep., 1974.
- [31] R. Kramer, M. Zankl, G. Williams, and G. Drexler, "The calculation of dose from external photon exposures using reference human phantoms and monte carlo methods: Part i. the male (adam) and female (eva) adult mathematical phantoms," GSF-National Research Center for Environment and Health, Neuherberg, Germany:, Tech. Rep. GSF-Report S-885, 1982.
- [32] S. Guatelli, B. Mascialino, and M. G. Pia, "Geant4 anthropomorphic phantoms," Genova, Italy, Oct 2006. [Online]. Available: http://geant4.slac.stanford.edu/Space06/presentations/01_Monday/12-Guatelli_phantom_nss2006.pdf
- [33] P. Dimbylow, "Fdtd calculations of the whole-body averaged sar in an anatomically realistic voxel model of the human body from 1 mhz to 1 ghz," *Physics in Medicine and Biology*, vol. 42, p. 479, 1997.
- [34] D. Jones, "A realistic anthropomorphic phantom for calculating organ doses arising from external photon irradiation," *Radiation Protection Dosimetry*, vol. 72, no. 1, p. 21, 1997.
- [35] U. Fill, M. Zankl, N. Petoussi-Henss, M. Siebert, and D. Regulla, "Adult female voxel models of different stature and photon conversion coefficients for radiation protection," *Health physics*, vol. 86, no. 3, p. 253, 2004.
- [36] N. Petoussi-Henss, M. Zankl, U. Fill, and D. Regulla, "The gsf family of voxel phantoms," *Physics in Medicine and Biology*, vol. 47, p. 89, 2002.
- [37] C. Shi and X. Xu, "Development of a 30-week-pregnant female tomographic model from computed tomography (ct) images for monte carlo organ dose calculations," *Medical physics*, vol. 31, p. 2491, 2004.
- [38] C. Lee, J. Williams, C. Lee, and W. Bolch, "The uf series of tomographic computational phantoms of pediatric patients," *Medical physics*, vol. 32, p. 3537, 2005.

- [39] M. Zankl, R. Veit, G. Williams, K. Schneider, H. Fendel, N. Petoussi, and G. Drexler, "The construction of computer tomographic phantoms and their application in radiology and radiation protection," *Radiation and Environmental Biophysics*, vol. 27, no. 2, pp. 153–164, 1988.
- [40] J. Nipper, J. Williams, and W. Bolch, "Creation of two tomographic voxel models of paediatric patients in the first year of life," *Physics in Medicine and Biology*, vol. 47, p. 3143, 2002.
- [41] K. Smans, M. Tapiovaara, M. Cannie, L. Struelens, F. Vanhavere, M. Smet, and H. Bosmans, "Calculation of organ doses in x-ray examinations of premature babies," *Medical physics*, vol. 35, p. 556, 2008.
- [42] C. Lee, C. Lee, S. Park, and J. Lee, "Development of the two korean adult tomographic computational phantoms for organ dosimetry," *Medical physics*, vol. 33, p. 380, 2006.
- [43] B. Zhang, J. Ma, L. Liu, and J. Cheng, "Cnman: a chinese adult male voxel phantom constructed from color photographs of a visible anatomical data set," *Radiation protection dosimetry*, 2007.
- [44] M. Ackerman, "The visible human project: a resource for anatomical visualization." *Studies in health technology and informatics*, vol. 52, p. 1030, 1998.
- [45] X. Xu, T. Chao, and A. Bozkurt, "Vip-man: an image-based whole-body adult male model constructed from color photographs of the visible human project for multi-particle monte carlo calculations," *Health Physics*, vol. 78, no. 5, p. 476, 2000.
- [46] M. Zankl, N. Petoussi-Hens, U. Fill, and D. Regulla, "The application of voxel phantoms to the internal dosimetry of radionuclides," *Radiation protection dosimetry*, vol. 105, no. 1-4, p. 539, 2003.
- [47] P. Campadelli, E. Casiraghi, S. Pratisoli, and G. Lombardi, "Automatic abdominal organ segmentation from ct images," *Electronic Letters on Computer Vision and Image Analysis*, vol. 8, no. 1, pp. 1–14, 2009.
- [48] M. George Linguraru, L. Zhixi, F. Shah, S. Chin, and R. Summers, "Automated liver segmentation using a normalized probabilistic atlas," *Progress in biomedical optics and imaging*, vol. 10, no. 38, 2009.
- [49] M. Linguraru, J. Sandberg, Z. Li, F. Shah, and R. Summers, "Automated segmentation and quantification of liver and spleen from ct images using normalized probabilistic atlases and enhancement estimation," *Medical physics*, vol. 37, p. 771, 2010.
- [50] N. Ray, S. Acton, T. Altes, E. De Lange, and J. Brookeman, "Merging parametric active contours within homogeneous image regions for mri-based lung segmentation," *Medical Imaging, IEEE Transactions on*, vol. 22, no. 2, pp. 189–199, 2003.

-
- [51] X. Liu, M. Linguraru, J. Yao, and R. Summers, "Organ pose distribution model and an map framework for automated abdominal multi-organ localization," *Medical Imaging and Augmented Reality*, pp. 393–402, 2010.
- [52] M. Linguraru, J. Yao, R. Gautam, J. Peterson, Z. Li, W. Marston Linehan, and R. Summers, "Renal tumor quantification and classification in contrast-enhanced abdominal ct," *Pattern recognition*, vol. 42, no. 6, pp. 1149–1161, 2009.
- [53] R. P. Sorlie, "Automatic segmentation of liver tumors from mri images," Master's thesis, Department of Physics University of Oslo, 2005.
- [54] H. Wang, R. Jaszczak, and R. Coleman, "Solid geometry-based object model for monte carlo simulated emission and transmission tomographic imaging systems," *IEEE Transactions on Medical Imaging*, vol. 11, no. 3, pp. 361–372, Sep 1992.
- [55] B. M. Tsui, J. A. Terry, and G. T. Gullberg, "Evaluation of cardiac cone-beam single photon emission computed tomography using observer performance experiments and receiver operating characteristic analysis." *Investigative radiology*, vol. 28, no. 12, pp. 1101–1112, 1993.
- [56] L. Piegl, "On nurbs: a survey," *Computer Graphics and Applications*, vol. 11, no. 1, pp. 55–71, 1991.
- [57] M. Ackerman, "The visible human project," *Proceedings of the IEEE*, vol. 86, no. 3, pp. 504–511, 2002.
- [58] P. M. Marine, M. G. Stabin, M. J. Fernald, and A. B. Brill, "Changes in radiation dose with variations in human anatomy: Larger and smaller normal-stature adults," *J Nucl Med*, vol. 51, pp. 806–811, 2010.
- [59] L. D. Clark, M. G. Stabin, M. J. Fernald, and A. B. Brill, "Changes in radiation dose with variations in human anatomy: Moderately and severely obese adults," *J Nucl Med*, vol. 51, pp. 929–932, 2010.
- [60] W. Snyder, M. Ford, G. Warner, and S. Watson, "S": Absorbed dose per unit cumulated activity for selected radionuclides and organs. mird pamphlet no. 11," *Society of Nuclear Medicine, New York*, 1975.
- [61] M. Stabin, R. Sparks, and E. Crowe, "Olinda/exm: the second-generation personal computer software for internal dose assessment in nuclear medicine," *Journal of Nuclear Medicine*, vol. 46, no. 6, p. 1023, 2005.
- [62] N. Petoussi-Henss, W. E. Bolch, M. Zankl, G. Sgouros, and B. Wessels, "Patient-specific scaling of reference s-values for cross-organ radionuclide s-values: what is appropriate?" *Radiation Protection Dosimetry*, vol. 127, no. 1-4, pp. 1922–196, 2007.

- [63] M. Stabin, J. Siegel, R. Sparks, K. Eckerman, and H. Breitz, "Contribution to red marrow absorbed dose from total body activity: a correction to the mird method," *Journal of Nuclear Medicine*, vol. 42, no. 3, p. 492, 2001.
- [64] L. Williams, A. Liu, D. Yamauchi, G. Lopatin, A. Raubitschek, and J. Wong, "The two types of correction of absorbed dose estimates for internal emitters," *Cancer*, vol. 94, no. S4, pp. 1231–1234, 2002.
- [65] R. Howell, B. Wessels, R. Loevinger, E. Watson, W. Bolch, A. Brill, N. Charkes, D. Fisher, M. Hays, J. Robertson *et al.*, "The mird perspective 1999. medical internal radiation dose committee." *Journal of Nuclear Medicine: Official Publication, Society of Nuclear Medicine*, vol. 40, no. 1, pp. 3S–10S, 1999.
- [66] A. Divoli, S. Chiavassa, L. Ferrer, J. Barbet, G. Flux, and M. Bardies, "Effect of patient morphology on dosimetric calculations for internal irradiation as assessed by comparisons of monte carlo versus conventional methodologies," *Journal of Nuclear Medicine*, vol. 50, no. 2, p. 316, 2009.
- [67] M. Cremonesi, M. Ferrari, C. Grana, A. Vanazzi, M. Stabin, M. Bartolomei, S. Papi, G. Prisco, G. Martinelli, G. Paganelli *et al.*, "High-dose radioimmunotherapy with 90y-ibritumomab tiuxetan: comparative dosimetric study for tailored treatment," *Journal of Nuclear Medicine*, vol. 48, no. 11, p. 1871, 2007.
- [68] G. Paganelli, C. De Cicco, M. Ferrari, G. Carbone, G. Pagani, M. Leonardi, M. Cremonesi, A. Ferrari, M. Pacifici, A. Di Dia *et al.*, "Intraoperative avidination for radionuclide treatment as a radiotherapy boost in breast cancer: results of a phase ii study with 90 y-labeled biotin," *European Journal of Nuclear Medicine and Molecular Imaging*, vol. 37, no. 2, pp. 203–211, 2010.
- [69] M. Stabin, "Uncertainties in internal dose calculations for radiopharmaceuticals," *Journal of Nuclear Medicine*, vol. 49, no. 5, p. 853, 2008.
- [70] R. B. Firestone, "Minimum acceptable uncertainties for adopted half-lives," Lawrence Berkeley National Laboratory, 2009, uSNDN/CSWEG Meeting, November 2-6, 2009. [Online]. Available: <http://www.nndc.bnl.gov/proceedings/2009csewgusndp/Wednesday/usndp/Half-lifeComparison.pdf>
- [71] M. Woods and S. Collins, "Half-life data—a critical review of tecdoc-619 update," *Applied radiation and isotopes*, vol. 60, no. 2-4, pp. 257–262, 2004.
- [72] R. Smart, "2009 australian radionuclide dose calibrator survey," *ANZ Nuclear Medicine Journal*, vol. 41, no. 3, pp. 2–5, 2009.
- [73] M. Koole, D. Lewis, C. Buckley, N. Nelissen, M. Vandenbulcke, D. Brooks, R. Vandenberghe, and K. Van Laere, "Whole-body biodistribution and radiation dosimetry of 18f-ge067: a radioligand for in vivo brain amyloid imaging," *Journal of Nuclear Medicine*, vol. 50, no. 5, p. 818, 2009.

- [74] R. Helmer and C. Van der Leun, "Recommended standards for [gamma]-ray energy calibration (1999)," *Nuclear Instruments and Methods in Physics Research Section A: Accelerators, Spectrometers, Detectors and Associated Equipment*, vol. 450, no. 1, pp. 35–70, 2000.
- [75] J. Thie, "Understanding the standardized uptake value, its methods, and implications for usage," *Journal of Nuclear Medicine*, vol. 45, no. 9, p. 1431, 2004.
- [76] L. Strauss and P. Conti, "The applications of pet in clinical oncology," *Journal of Nuclear Medicine*, vol. 32, no. 4, p. 623, 1991.
- [77] C. Kim, N. Gupta, B. Chandramouli, and A. Alavi, "Standardized uptake values of fdg: body surface area correction is preferable to body weight correction," *Journal of Nuclear Medicine*, vol. 35, no. 1, p. 164, 1994.
- [78] R. Hicks, "The suv and fit pet: A tasty alphabet soup or a dog's breakfast?" *Leukemia & lymphoma*, vol. 48, no. 4, pp. 649–652, 2007.
- [79] J. Keyes Jr, "Suv: Standard uptake or silly useless value?" *Journal of Nuclear Medicine*, vol. 36, no. 10, p. 1836, 1995.
- [80] G. O'Keefe, T. Saunder, S. Ng, U. Ackerman, H. Tochon-Danguy, J. Chan, S. Gong, T. Dyrks, S. Lindemann, G. Holl *et al.*, "Radiation dosimetry of β -amyloid tracers 11c-pib and 18f-bay94-9172," *Journal of Nuclear Medicine*, vol. 50, no. 2, p. 309, 2009.
- [81] M. Stabin, "Mirdose: personal computer software for internal dose assessment in nuclear medicine," *Journal of Nuclear Medicine*, vol. 37, no. 3, p. 538, 1996.
- [82] —, "New internal radiation dose and modeling software; fda approves commercial mirdose successor," *Journal of Nuclear Medicine*, vol. 45, pp. 26–27, 2004.
- [83] R. E. Toohey, "Mirdose 3 distribution suspended," *Journal of Nuclear Medicine*, vol. 41, no. 6, pp. 13N–19, 2000. [Online]. Available: <http://jnm.snmjournals.org>
- [84] R. Loevinger, T. Budinger, and E. Watson, "Mird primer for absorbed dose calculations. new york: The society of nuclear medicine," 1988.
- [85] M. Stabin and J. Siegel, "Physical models and dose factors for use in internal dose assessment," *Health physics*, vol. 85, no. 3, p. 294, 2003.
- [86] ICRP, "Limits for intakes of radionuclides by workers, icrp publication 30," International Commission on Radiological Protection, Tech. Rep. 30, 1972.
- [87] N. Metropolis, "The beginning of the monte carlo method," pp. 125–131, 1987. [Online]. Available: <http://jackman.stanford.edu/mcmc/metropolis1.pdf>

-
- [88] T. E. Booth, F. B. Brown, J. S. Bull, R. A. Forster, J. T. Goorley, H. G. Huges, R. L. Martz, R. E. Prael, A. Sood, J. E. Sweezy, and A. J. Zukaitis, "Mcnp5 1.50 release notes," Los Alamos National Laboratory, Tech. Rep., 2008, accessed: 2010. [Online]. Available: <http://mcnp-green.lanl.gov/index.html>
- [89] I. Kawrakow, E. Mainegra-Hing, D. Rogers, F. Tessier, and B. Walters, "The egsnrc code system: Monte carlo simulation of electron and photon transport," National Research Council of Canada, NRCC Report PIRS-701, 2010. [Online]. Available: <http://www.irs.inms.nrc.ca/inms/irs/EGSnrc/EGSnrc.html>
- [90] P. Andreo and M. Ljungberg, *General Monte Carlo Codes for use in Medical Radiation Physics*, ser. Medical Science Series. Institute of Physics Publishing, 1998, ch. 4.
- [91] H. Yoriyaz, M. Stabin, and A. Santos, "Monte carlo mcnp-4b-based absorbed dose distribution estimates for patient-specific dosimetry," *Journal of Nuclear Medicine*, vol. 42, no. 4, pp. 662–669, 2004.
- [92] P. Ferrari and G. Gualdrini, "An improved mcnp version of the norman voxel phantom for dosimetry studies," *Physics in Medicine and Biology*, vol. 50, pp. 4299–4316, 2005.
- [93] M. Sohrabpour, M. Hassanzadeh, M. Shahriari, and M. Sharifzadeh, "Gamma irradiator dose mapping simulation using the mcnp code and benchmarking with dosimetry," *Applied Radiation and Isotopes*, vol. 57, no. 4, pp. 537–542, 2002.
- [94] R. Miro, J. Soler, S. Gallardo, J. M. Campay, S. Diez, and G. Verdu, "Mcnp simulation of a theratron 780 radiotherapy unit," *Radiation Protection and Dosimetry*, vol. 116, no. 4, pp. 65–68, 2005.
- [95] A. Bielajew, H. Hirayama, W. Nelson, and D. Rogers, "History, overview and recent improvements of egs4," National Research Council of Canada and National Laboratory for High Energy Physics and Stanford Linear Accelerator Center, Tech. Rep., 1994, accessed Aug 2010. [Online]. Available: <http://rcwww.kek.jp/research/egs/>
- [96] M. Stabin and H. Zaidi, *Monte Carlo Codes for use in therapeutic nuclear medicine*, ser. Series in Medical Physics and Biomedical Engineering. Institute of Physics Publishing, 2003, ch. 6.
- [97] K. Amako, S. Guatelli, V. Ivanchenko, M. Maire, B. Mascialino, K. Murakami, L. Pandola, S. Parlati, M. G. Pia, M. Piergentili, T. Sasaki, and U. L., "Validation of geant4 electromagnetic physics versus protocol data," in *Nuclear Science Symposium Conference Record, IEEE*, 2004.
- [98] F. Salvat, J. Fernandez-Varea, and J. Sempau, "Penelope-2008: A code system for monte carlo simulation of electron and photon transport," in *OECD Nuclear Energy Agency, Issy-les-Moulineaux NEA France*, 2008.

-
- [99] S. Chauvie, S. Guatelli, V. Ivanchenko, F. Longo, A. Mantero, B. Mascialino, P. Nieminen, L. Pandola, S. Parlati, L. Peralta *et al.*, “Geant4 low energy electromagnetic physics,” in *Nuclear Science Symposium Conference Record, 2004 IEEE*, vol. 3. IEEE, 2005, pp. 1881–1885.
- [100] S. Jan, G. Santin, D. Strul, S. Staelens, K. Assié, D. Autret, S. Avner, R. Barbier, M. Bardiès, P. M. Bloomfield *et al.*, *GATE Users Guide*, 2007. [Online]. Available: <http://www.opengatecollaboration.org>
- [101] R. L. Harrison, “Simset,” 1993. [Online]. Available: http://depts.washington.edu/simset/html/simset_main.html
- [102] K. Iwata, R. G. Greaves, and C. M. Surko, “gamma -ray spectra from positron annihilation on atoms and molecules,” *Physical Review A*, vol. 55, no. 5, p. 3586, 1997. [Online]. Available: <http://link.aps.org/abstract/PRA/v55/p3586>
- [103] S. Jan, D. Benoit, E. Becheva, T. Carlier, F. Cassol, P. Descourt, T. Frisson, L. Grevillot, L. Guigues, L. Maigne *et al.*, “Gate v6: a major enhancement of the gate simulation platform enabling modelling of ct and radiotherapy,” *Physics in Medicine and Biology*, vol. 56, p. 881, 2011.
- [104] D. Visvikisa, M. Bardiesb, S. Chiavassab, C. Danfordc, A. Kirovc, F. Lamarea, L. Maigned, S. Staelense, and T. R., “Use of the gate monte carlo package for dosimetry applications,” *Nucl. Inst. and Meth. A*, vol. 569, pp. 335–340, 2006.
- [105] J. De Beenhouwer, S. Staelens, D. Kruecker, L. Ferrer, Y. D’Asseler, I. Lemahieu, and F. Rannou, “Cluster computing software for gate simulations,” *Medical physics*, vol. 34, p. 1926, 2007.
- [106] S. Staelens, J. De Beenhouwer, D. Kruecker, L. Maigne, F. Rannou, L. Ferrer, Y. D’Asseler, I. Buvat, and I. Lemahieu, “Gate: improving the computational efficiency,” *Nuclear instruments and methods in physics research section a: Accelerators, spectrometers, detectors and associated equipment*, vol. 569, no. 2, pp. 341–345, 2006.
- [107] S. Jan, C. Comtat, D. Strul, G. Santin, and R. Trebossen, “Monte carlo simulation for the ecat exact hr+ system using gate,” *IEEE Tran Nucl Sci*, vol. 52, no. 3, pp. 627–633, 2005.
- [108] R. Taschereau and A. Chatziioannou, “Compressed voxels for high-resolution phantom simulations in gate,” *Molecular Imaging and Biology*, vol. 10, no. 1, pp. 40–47, 2008.
- [109] National Electrical Manufactures Association, “Nu2-1994 performance measurements of positron emission tomographs,” National Electrical Manufactures Association, Tech. Rep., 1994. [Online]. Available: <http://www.nema.org/stds/nu2.cfm>.
- [110] H. Hines, M. Casey, N. Wainer, J. Colsher, C. Stearns, M. E. D. Witherspoon, J. Karp, V. Simcic, P. Vernon, G. Muehllehner, Y. Hefetz, and T. Rempel,

- “Nu2-2001 performance measurements of positron emission tomographs,” National Electrical Manufactures Association, Tech. Rep., 2001. [Online]. Available: <http://www.nema.org/stds/nu2.cfm>.
- [111] A. Perkins, C. Stearns, J. Chapman, J. Kolthammer, J. J. Williams, and M. Casey, “Nu2-2007 performance measurements of positron emission tomographs,” National Electrical Manufactures Association, Tech. Rep., 2007. [Online]. Available: <http://www.nema.org/stds/nu2.cfm>.
- [112] Y. Chung, Y. Choi, G. Cho, Y. Choe, K. Lee, and B. Kim, “Optimization of dual layer phoswich detector consisting of lso and luyap for small animal pet,” *Nuclear Science, IEEE Transactions on*, vol. 52, no. 1, pp. 217–221, 2005.
- [113] J. Jung, Y. Choi, Y. Chung, O. Devroede, M. Krieguer, P. Bruyndonckx, and S. Tavernier, “Optimization of lso/luyap phoswich detector for small animal pet,” *Nuclear Instruments and Methods in Physics Research Section A: Accelerators, Spectrometers, Detectors and Associated Equipment*, vol. 571, no. 3, pp. 669–675, 2007.
- [114] N. Karakatsanis, N. Sakellios, N. X. Tsantilas, N. Dikaios, C. Tsoumpas, D. Lazaro, G. Loudos, C. R. Schmidtlein, K. Louizi, J. Valaisc, D. Nikolopoulos, J. Malamitsib, J. Kandarakis, and K. Nikita, “Comparative evaluation of two commercial pet scanners, ecat exact hr + and biograph 2, using gate,” *Nucl. Inst. and Meth. A*, vol. 569, pp. 368–372, 2006.
- [115] F. Lamare, A. Turzo, Y. Bizais, C. C. Le Rest, and D. Visyikis, “Validation of a monte carlo simulation of the philips allegro/gemini pet systems using gate,” *Physics in Medicine and Biology*, vol. 51, pp. 943–962, 2006.
- [116] P. Gonias, N. Bertsekas, N. Karakatsanis, G. Saatsakis, A. Gaitanis, D. Nikolopoulos, G. Loudos, L. Papaspyrou, N. Sakellios, N. X. Tsantilas, A. Daskalakis, P. Liaparinos, K. Nikita, A. Louizi, D. Cavouras, I. Kandarakis, and G. S. Panayiotakis, “Validation of a gate model for the simulation of the siemens biograph 6 pet scanner,” *Nucl. Inst. and Meth. A*, vol. 571, pp. 263–266, 2007.
- [117] C. R. Schmidtlein, A. S. Kirov, S. A. Nehneh, Y. E. Erdi, L. M. Bidaut, A. Ganin, C. W. Stearns, D. L. McDaniel, and K. A. Hamacher, “Validation of gate monte carlo simulations of the ge advance/discovery ls pet scanners,” *Medical Physics*, vol. 33, no. 1, pp. 198–208, 2006.
- [118] D. Autret, A. Bitar, L. Ferrer, A. Lisbona, and M. Bardiès, “Monte carlo modeling of gamma cameras for i-131 imaging in targeted radiotherapy,” *Cancer biotherapy & radiopharmaceuticals*, vol. 20, no. 1, pp. 77–84, 2005.
- [119] S. Staelens, D. Strul, G. Santin, S. Vandenberghe, M. Koole, Y. D’Asseler, I. Lemahieu, and R. Walle, “Monte carlo simulations of a scintillation camera using gate: validation and application modelling,” *Physics in Medicine and Biology*, vol. 48, p. 3021, 2003.

- [120] S. Staelens, G. Santin, S. Vandenberghe, D. Strul, M. Koole, Y. D'Asseler, I. Lemahieu, and R. Van de Walle, "Transmission imaging with a moving point source: influence of crystal thickness and collimator type," *Nuclear Science, IEEE Transactions on*, vol. 52, no. 1, pp. 166–173, 2005.
- [121] Z. El Bitar, D. Lazaro, C. Coello, V. Breton, D. Hill, and I. Buvat, "Fully 3d monte carlo image reconstruction in spect using functional regions," *Nuclear Instruments and Methods in Physics Research Section A: Accelerators, Spectrometers, Detectors and Associated Equipment*, vol. 569, no. 2, pp. 399–403, 2006.
- [122] J. Ortuno, P. Guerra-Gutierrez, J. Rubio, G. Kontaxakis, and A. Santos, "3d-osem iterative image reconstruction for high-resolution pet using precalculated system matrix," *Nuclear Instruments and Methods in Physics Research Section A: Accelerators, Spectrometers, Detectors and Associated Equipment*, vol. 569, no. 2, pp. 440–444, 2006.
- [123] J. He, G. O'Keefe, S. Gong, G. Jones, T. Saunder, A. Scott, and M. Geso, "A novel method for respiratory motion gated with geometric sensitivity of the scanner in 3d pet," *Nuclear Science, IEEE Transactions on*, vol. 55, no. 5, pp. 2557–2565, 2008.
- [124] L. Ferrer, N. Chouin, A. Bitar, A. Lisbona, and B. M., "Implementing dosimetry in gate: Dose-point kernel validation with geant4 4.8.1," *CANCER BIOTHERAPY & RADIOPHARMACEUTICALS*, vol. 22, no. 1, pp. 125–129, 2007.
- [125] C. O. Thiam, V. Breton, D. Donnarieix, B. Habib, and M. L., "Validation of a dose deposited by low-energy photons using gate/geant4," *Physics in Medicine and Biology*, vol. 53, pp. 3039–3055, 2008.
- [126] R. Taschereau and C. A. F., "Monte carlo simulations of absorbed dose in a mouse phantom from 18-fluorine compounds," *Medical Physics*, vol. 34, pp. 1026–1036, 2007.
- [127] D. Rogers and R. Mohan, "Questions for comparison of clinical monte carlo codes," in *13th ICCR Monte Carlo Session*, 2000. [Online]. Available: <http://www.irs.inms.nrc.ca/papers/iccr00/iccr00.html>
- [128] M. J. Rivard, B. M. Corsey, L. A. DeWerd, W. F. Hanson, H. M. Saiful, G. S. Ibbott, M. G. Mitch, R. Nath, and J. F. Williamson, "Update of aapm task group no. 43 report: a revised aapm protocol for brachytherapy dose calculations." *Medical Physics*, vol. 31, pp. 633–74, 2004.
- [129] G. Cirrone, G. Cuttone, F. Di Rosa, L. Pandola, F. Romano, and Q. Zhang, "Validation of the geant4 electromagnetic photon cross-sections for elements and compounds," *Nucl. Inst. and Meth. A*, vol. 618, pp. 315–322, 2010.
- [130] B. A. Faddegon, I. Kawrakow, Y. Kubyshev, J. Perl, J. Sempau, and L. Urban, "The accuracy of egsnrc, geant4 and penelope monte carlo systems for the

- simulation of electron scatter in external beam radiotherapy,” *Physics in Medicine and Biology*, vol. 54, pp. 6151–6163, 2009.
- [131] P. Chin and N. M. Spyrou, “Monte carlo investigation of positron annihilation in medicine positron emission tomography,” *Nucl. Inst. and Meth. A*, vol. 580, pp. 481–484, 2007.
- [132] VPAC, “Victorian partnership for advanced computing,” 2010. [Online]. Available: <http://www.vpac.org/services/supercomputers/tango>
- [133] AMD, “Amd opteron™ processor solutions,” 2010. [Online]. Available: <http://products.amd.com/en-us/OpteronCPUDetail.aspx?id=419>
- [134] J. Browne and A. De Pierro, “A row-action alternative to the em algorithm for maximizing likelihood in emission tomography,” *Medical Imaging, IEEE Transactions on*, vol. 15, no. 5, pp. 687–699, 1996.
- [135] M. Atkins and B. Mackiewich, “Fully automatic segmentation of the brain in mri,” *Medical Imaging, IEEE Transactions on*, vol. 17, no. 1, pp. 98–107, 2002.
- [136] L. Massoptier and S. Casciaro, “A new fully automatic and robust algorithm for fast segmentation of liver tissue and tumors from ct scans,” *European Radiology*, vol. 18, no. 8, pp. 1658–1665, 2008.
- [137] S. Pan and B. Dawant, “Automatic 3d segmentation of the liver from abdominal ct images: a level-set approach,” in *Proceedings of SPIE*, vol. 4322, 2001, p. 128.
- [138] T. Jones and D. Metaxas, “Automated 3d segmentation using deformable models and fuzzy affinity,” in *Information Processing in Medical Imaging*. Springer, 1997, pp. 113–126.
- [139] W. Ellett, G. Brownell, and R. Reddy, “An assessment of monte carlo calculations to determine gamma ray dose from internal emitters,” *Physics in Medicine and Biology*, vol. 13, no. 2, pp. 219 – 230, 1968.
- [140] G. van Rossum, “Python programming language.” [Online]. Available: <http://www.python.org/>
- [141] J. Turner, *Atoms, radiation, and radiation protection*. Vch Pub, 2007.
- [142] M. J. Berger, J. S. Coursey, M. A. Zucker, and J. Chang, “Stopping-power and range tables stopping-power and range tables for electrons, protons, and helium ions,” Oct 2010. [Online]. Available: <http://www.nist.gov/pml/data/star/index.cfm>
- [143] N. Rehfeld, S. Stute, J. Apostolakis, M. Soret, and I. Buvat, “Introducing improved voxel navigation and fictitious interaction tracking in gate for enhanced efficiency,” *Physics in Medicine and Biology*, vol. 54, p. 2163, 2009.

- [144] J. Valentin, *Basic anatomical and physiological data for use in radiological protection: reference values*. Elsevier, 2003, vol. 89.
- [145] M. Matsumoto and T. Nishimura, “Merenne twister: A 623-dimensionally equidistributed uniform pseudo-random number generator,” *ACM Transactions on Modeling and Computer Simulation*, vol. 8, no. 1, pp. 3–30, 1998.
- [146] M. Bethesda, “Tissue substitutes in radiation dosimetry and measurement, report 44,” International Commission on Radiation Units and Measurements, Tech. Rep., 1989.
- [147] M. J. Berger, J. H. Hubbell, S. M. Seltzer, J. Chang, J. S. Coursey, R. Sukumar, and D. S. Zucker, “Xcom: Photon cross sections database,” The National Institute of Standards and Technology (NIST), Accessed 2010. [Online]. Available: <http://www.nist.gov/physlab/data/xcom/index.cfm>
- [148] W. Nelson, H. Hirayama, and D. Rogers, “The egs4 code system, report slac-265,” Stanford Linear Accelerator Center, Tech. Rep., 1985.
- [149] J. K. Shultis and R. E. Faw, *Radiation shielding*. American Nuclear Society, 2000.
- [150] H. Wellisch, M. Maire, and L. Urban, *Geant4 Users’ Documents: Physics Reference Manual*, 8th ed., CERN, 2005. [Online]. Available: <http://geant4.cern.ch/G4UsersDocuments/UsersGuides/PhysicsReferenceManual/html/PhysicsReferenceManual.html>
- [151] Y. S. Horowitz, A. Dubi, and S. Mordechai, “The monte carlo nonuniform sampling technique applied to the klein-nishina probability density function,” *Nucl. Sci. Eng.*, vol. 60, pp. 461–482, 1976.
- [152] R. N. Blomquist and E. M. Gelbard, “An assessment of existing klein-nishina monte carlo sampling methods,” *Nucl. Sci. Eng.*, vol. 83, pp. 380–384, 1983.
- [153] H. Zaidi, *Quantitative Analysis in Nuclear Medicine Imaging*. Springer, 2006, ch. 11 Monte Carlo Modeling in Nuclear Medicine Imaging, pp. 358–390.